UNIVERSITY OF OSLO
Department of Chemistry

High Temperature Oxidation of Sanergy HT

- oxidation kinetics and growth mechanism of a metallic interconnect

Master's thesis in Materials, Energy and Nanotechnology

Aina Øverås Skott

June 2013

Preface

This thesis fulfils the requirements for the Master of Science degree in Materials Chemistry under the program Materials, Energy and Nanotechnology at the University of Oslo. The experimental work in this thesis was conducted at the Centre for Materials Science and Nanotechnology (SMN) from August 2011 to June 2013.

I would first like to thank my supervisor Reidar Haugsrud for great guidance and encouragement. The group of Solid-State Electrochemistry is thanked for challenging discussions and advice, especially Truls Norby for valuable feedback, Anna Magraso Sola for technical and emotional support during HT-ESEM experiments and Anders Werner Bredvei Skilbred for enthusiastically introducing me to the art of high temperature oxidation. Zuoan Li for guidance during two-stage oxidation experiments, and my fellow Master students for all the good times during the last five years. Especially, I would like to thank my best friend Kari Nordholm for always being positive, never giving up and for spending more time with me the last two years than with her family and friends combined. Together we have achieved impossible goals, survived a tropical storm and planned enough adventures to last a lifetime.

I am grateful to my parents, family and friends for support and distractions. Tor-Erik is thanked for tolerating endless stories about the ups and downs of my life as a student, and for kicking me out of airplanes when I complain too much. Finally, I would like to thank my sister Anette for being my ultimate life coach and travel companion, and for starting early to prepare me for life by teaching me how to do fractions in kindergarten.

Oslo, June 2013

Aina Øverås Skott

Abstract

Chromia forming alloys are regarded as promising interconnects materials for fuel cell applications.[1,2] Under operating conditions metallic interconnects will oxidise, forming a protective oxide layer which will affect the electrical and mechanical properties of the interconnect. Sanergy HT from Sandvik Materials Technology is a commercial multicomponent Fe-22Cr alloy developed specifically for fuel cells. In this work, the oxidation behaviour and growth kinetics of Sanergy HT were examined.

Samples of uncoated and 600 nm Co coated Sanergy HT were oxidized at temperatures from 800 °C to 1000 °C in air, O_2+Ar and 5 % H_2+Ar. Thermogravimetry (TG) was used to examine oxide scale growth kinetics, and in-situ High Temperature Environmental Scanning Electron Microscopy (HT-ESEM) was used to study formation and development of morphological features. The chemical composition of the oxide scales was identified by X-ray diffraction (XRD) and Energy Dispersive Spectrometry (EDS) analysis. Microstructure and morphology of surfaces and cross sections were analysed by Scanning Electron Microscopy (SEM). Two-stage oxidation by ^{18}O-^{16}O isotope exchange was conducted to investigate growth mechanisms of Cr_2O_3 and (Co, Mn)$_3O_4$ on coated samples. Secondary Ion Mass Spectrometry (SIMS) was used to obtain depth profiles of ion distributions in the formed oxide scales.

The formed oxide scales consist of duplex layers of Cr_2O_3 near the oxide-alloy interface, with an (A, B)$_3O_4$ spinel (A, B = Mn, Cr, Co, Fe) phase in the outer part of the scale, near the gas-oxide interface. The oxides grow predominately by outward diffusion of cations. The oxide growth kinetics were generally observed to be parabolic, with growth rates for cobalt coated samples varying from $1.9{\cdot}10^{-13}$ to $1.0{\cdot}10^{-11}$ g^2/cm^4s at temperatures between 850 °C and 1000 °C in wet air. The activation energy for cobalt coated samples was 320 kJ/mol. The growth rate constants of uncoated samples exhibited non-linear temperature dependence, and no activation energy could be calculated for the full temperature range. The rate constants of both cobalt coated and uncoated samples were also found to be independent of p_{O_2}. The irregular dependence of temperature and the

independence of p_{O_2} is assumed to result from alloying elements entering as aliovalent dopants in the growing oxide scales.

List of Abbreviations

BSC Bias Supply Controller

EDS Energy Dispersive Spectroscopy

ESEM Environmental Scanning Electron Microscopy

ETD Everhart-Thornley Detector

HSA Heating Shield Assembly

HSM Heating Stage Module

HT-ESEM High Temperature Scanning Electron Microscopy

HT-GSED High Temperature Gaseous Secondary Electron Detector

HTSC High Temperature Stage Controller

HV High Vacuum

LFD Large-Field Detector

REO Reactive Element Oxides

SEM Scanning Electron Microscopy

SOFC Solid Oxide Fuel Cell

SSD Solid-State Detector

TEC Thermal Expansion Coefficient

TG Thermogravimetry

WFB Water Flow Box

XRD X-ray Diffraction

Contents

Chapter 1

Introduction

1.1 Background and motivation

The world is facing a great challenge. The global energy demand is expected to double by 2050, even if improvements are made in increasing energy efficiency.[3] This is a consequence of growth in the human population and also the enhanced standard of living in highly populated countries with rapidly expanding economies. As of today, fossil fuels are by far the most common energy source worldwide. However, as fossil fuels are a limited resource, the available amounts of coal, oil and natural gas are not sufficient to meet the future energy demand. In addition, enormous stresses are caused on the environment by the combustion of fossil fuels. Most climate scientists agree that the major changes in climate and increasing average surface temperature of the Earth are related to man-made emissions in the atmosphere. Thus, there is a great need of environmentally friendly and competitive alternatives to non-renewable energy sources. For new energy technology to be commercialized, it is absolutely vital that it is economically competitive, efficient and has an adequate lifetime. Fuel cells stand out as a technology of great potential due to high efficiencies and versatile application possibilities.

1.2 Fuel cells

A fuel cell is a device converting chemical energy directly to electricity through a chemical reaction. As no combustion is involved, the energy conversion is very efficient and with much less generated pollutants compared to traditional power systems. Fuel cells are galvanic cells, similar to ordinary batteries. But unlike batteries, fuel cells do not need recharging and will not run down as long as fuel is available. A fuel cell consists of two electrodes, anode and cathode, separated by an electrolyte. Fuel is supplied to the anode, where it is oxidized and the electrons are transferred to an external

circuit. At the cathode, an oxidant such as oxygen gas, is reduced and electrons are drawn from the external circuit, while ions are conducted through the electrolyte.

The fuel may either come from fossil resources, such as gases from coal, oil or natural gas, or from renewable energy sources. The most common fuel from renewable resources is hydrogen, but also methanol, ammonia and biofuels have become increasingly relevant.

To achieve usable power, individual fuel cells must be connected in series.. This series of connected cells is referred to as a stack. Depending on the particular application, the configuration of the fuel cell stack may vary. Several configurations, with differences in geometry and power density, have been reported.

1.2.1 The Solid Oxide Fuel Cell

The Solid Oxide Fuel Cell (SOFC) is regarded as the most effective and versatile fuel cell there is,[4] suitable for various applications from vehicles to large-scale, stationary power stations.[5] The SOFC is characterized by solid-state components only. The electrolyte is a solid inorganic ceramic, often yttria-stabilised zircona,[6] in between two porous electrodes as seen in figure 1.1. At the cathode, oxygen gas is reduced to oxygen ions. The oxygen ions are then lead through the electrolyte, before reacting with the fuel at the anode. The operating temperatures are high, typically from 750 °C to 1000 °C.[6] The high operating temperatures are due to slow oxygen transport through the electrolyte at lower temperatures.[4]

As SOFCs operate at elevated temperatures, the requirements for each material component are tough. However, due to their many advantages, such as high efficiency and fuel flexibility, SOFCs are still the leading fuel cell type in regards to commercialization.[5] The highest fuel efficiency for SOFCs has been at 1000 °C,[5] but at such high temperatures the cell life-time decreases significantly. One challenge is thus to reduce the operating temperature, while maintaining high efficiency. This would significantly reduce the total cost of the fuel cell, especially for sealing materials and the interconnect.

1.3 The interconnect

A fuel cell interconnect is a material separating the individual cells in a fuel cell stack, and has the most stringent requirements of all fuel cell components. The interconnect has to separate the fuel on the anode side of one cell from the air on the cathode side of the neighbouring cell. In

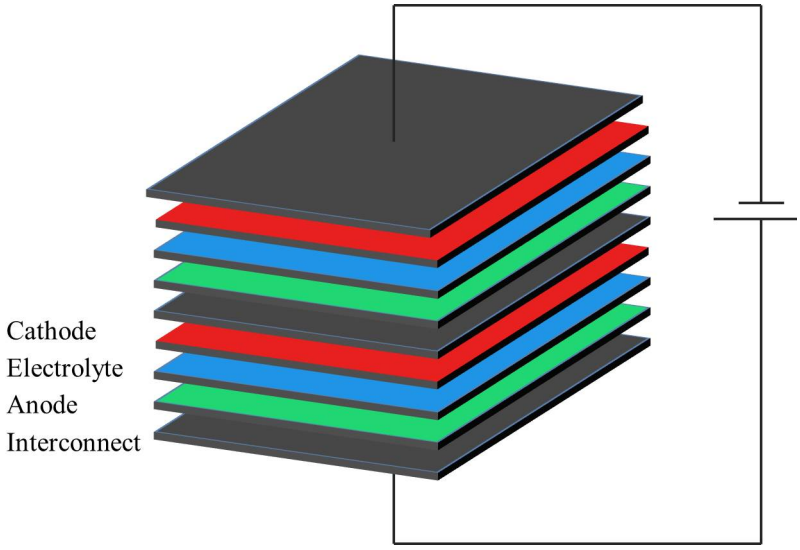

Figure 1.1: Schematic diagram of a flat plate fuel cell stack.

addition, the interconnect must provide electrical connection between the cells, good channels for gas flow and preferably be low-weight.

Naturally, there are few materials available that can fulfil these requirements. The two main groups of suitable materials are ceramics and metal alloys. Ceramics are brittle, have complicated fabrication routes and high cost, and metallic interconnects will thus be the focus of this survey. A disadvantage with metallic interconnects is that under operating conditions, oxidation of the alloy surface is inevitable. The formation of an oxide scale on the surface will alter both the mechanical and electrical properties of the interconnect material, resulting in degradation and reduced performance of the fuel cell. If metallic interconnects are to be used in fuel cell applications, the oxidation behaviour under operating conditions must be examined thoroughly. The following chapter will give a brief introduction to high temperature oxidation of metals, especially for chromia-forming alloys.

1.4 Objective

The main objective of this study is to investigate the oxidation behaviour of Sanergy HT from Sandvik Materials Technology, an iron-chromium alloy to be used as interconnect material in fuel cell stacks. The work will include examination of oxide growth kinetics and scale properties under both oxidizing and reducing conditions, and at high temperatures. Measurements will be conducted on both uncoated and 600 nm Co coated samples of Sanergy HT to elucidate the effect of cobalt coating on oxidation properties.

Oxide growth rates of uncoated and cobalt coated samples at temperatures from 800 °C to 1000 °C in air, O_2+Ar mixtures and 5 % H_2+Ar will be studied by Thermogravimetry (TG). In addition, TG will be used to investigate the effect of temperature, time and oxygen activity on oxide growth rates. The effect of cobalt coating will be evaluated by Scanning Electron Microscopy (SEM) and two-stage oxidation in oxygen isotopes $^{18,18}O_2$ and $^{16,16}O_2$. The chemical composition of the formed oxide scales will be determined by X-ray diffraction (XRD) and Energy Dispersive Spectroscopy (EDS) analysis. Microstructure and morphology of surfaces and cross sections will be analysed by Scanning Electron Microscopy (SEM).

Fe-Cr alloys with a sufficient amount of Mn will form duplex oxide scales of Cr_2O_3 and a $(Cr, Mn)_3O_4$ spinel phase. The growth mechanisms of these two oxides will be investigated by two-stage oxidation in $^{18,18}O_2$ and $^{16,16}O_2$. Secondary Ion Mass Spectrometry (SIMS) will be used to obtain depth profiles of oxygen isotope and cation distributions in the formed oxide scales. Cross-sections of the oxidized samples will be examined by EDS spot analyses and line scans to map possible temperature and time variations in the concentrations of the scales.

The formation and development of oxide surface features in 600 Pa H_2O at temperatures from 600 °C to 900 °C will be studied in-situ by High Temperature Environmental Scanning Electron Microscopy (HT-ESEM) and ex-situ by SEM. HT-ESEM will also be evaluated as an experimental method in the field of high temperature oxidation. The comparability with TG, which is a far more conventional method, will be investigated by comparing samples oxidized during HT-ESEM and by TG under similar conditions.

Chapter 2

Theory

2.1 Oxidation of metals and alloys

The theory in this chapter is retrieved from ″High Temperature Corrosion" by Per Kofstad[7] unless stated otherwise. Oxide scales form on metal surfaces under most conditions, as long as the partial pressure of oxygen at the surface is sufficient. As oxidation can lead to drastically changed material properties, understanding and reducing this problem is of high importance in all parts of the industry where metals and alloys are used. It has therefore been a driving force to develop materials with high oxidation resistance and to investigate methods for improving surfaces of already commercial alloys.

$$xM + (\frac{y}{2})O_2 = M_xO_y \tag{2.1}$$

Although the chemical reaction of forming a metal oxide, equation 2.1, may seem simple and straight-forward, the process itself is often highly complicated. Factors influencing the oxidation process include temperature, pressure, gas composition, the elapsed time of the reaction, pretreatment and surface preparation.

The growth mechanism of an oxide scale is a combination of several reactions. Initially, gas molecules are adsorbed on the surface and dissociated due to the high reactivity of surface atoms. As the reaction continues, oxide nuclei will form and grow by surface diffusion until a continuous oxide film is covering the surface completely. The nucleation site of the first oxide is believed to be lattice imperfections such as grain boundaries or dislocations, but could also be surface impurities.

When a continuous oxide film separates the metal surface from the oxygen gas, the reaction can proceed further only by solid-state diffusion of the reactants through the film. This may occur by inward diffusion of oxygen reacting with metal at the oxide-metal interface, or by metal diffusing

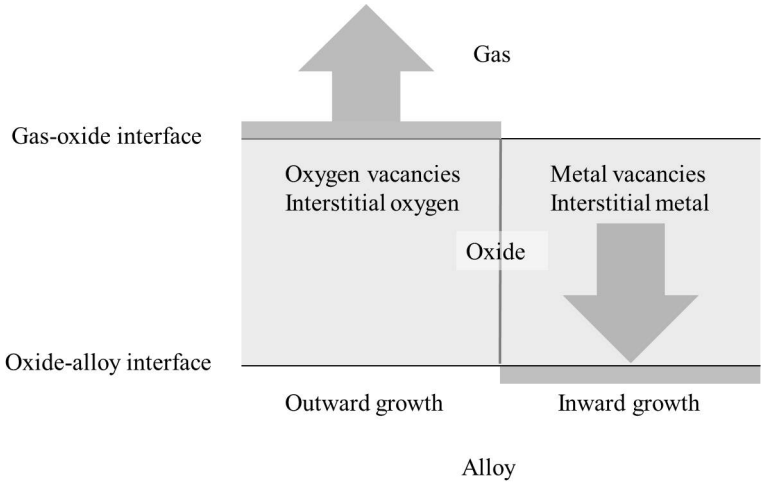

Figure 2.1: Oxide formation and scale growth on metal surface by inward and outward diffusing species.

outwards to react at the gas-oxide interface, as seen in figure 2.1. The driving force for these processes are generally the presence of an electric field or a gradient in chemical potential.

Metals and alloys generally oxidise following the same principles. However, due to the increased number of reactants present, the oxidation of alloys can be complex. Variations in thermodynamic stability, properties of reaction products and differences in diffusivity for alloying elements through the alloy and the formed oxide are all contributing factors to complex oxidation behaviour. As pure metals are seldom used as construction materials, understanding the oxidation mechanisms of important alloys is necessary.

2.2 The thermodynamics of oxidation reactions

When a metal reacts with oxygen gas to form a metal oxide, see equation 2.1, the chemical reaction is driven by a change in Gibbs free energy.

$$\Delta G_r = \Delta H_r - T\Delta S_r \tag{2.2}$$

At constant temperature, a change in Gibbs free energy is directly related to the changes in enthalpy and entropy of the reaction, as seen in equation 2.2. In equation 2.2, G_r is the Gibbs free energy, T is the temperature, H_r is the enthalpy and S_r the entropy of the reaction. For a specific reaction at constant pressure and temperature to happen spontaneously, the change in Gibbs free energy must be negative. Any system will thus tend to react until ΔG_r is at a minimum. When the change in Gibbs free energy of a reaction

is zero, the reaction is at equilibrium and thus not spontaneous in either direction. The change in Gibbs free energy of a reaction at equilibrium, ΔG_r°, can be expressed in terms of the equilibrium constant, K:

$$\Delta G_r^\circ = -\mathrm{R}T \ln K_r \tag{2.3}$$

R is the ideal gas constant and K_r is defined by the activities of the chemical species involved in the reaction. For the oxidation reaction in equation 2.2, the Gibbs free energy can thus be written:

$$\Delta G_r^\circ = -\mathrm{R}T \ln K_r = -\mathrm{R}T \ln \left(\frac{a(M_x O_y)}{a(M)^x a(O_2)^{\frac{y}{2}}} \right) \tag{2.4}$$

The activities, a, of pure solids and liquids can be approximated as unity, and the activity of gases may be approximated by their partial pressures $a_J = p_J/p^\circ$.

$$\Delta G_r^\circ = -\mathrm{R}T \ln \left(\frac{1}{a(O_2)^{y/2}} \right) = -\mathrm{R}T \ln \left(p_{o_2}^{-y/2} \right) \tag{2.5}$$

Equation 2.5 can be rearranged to:

$$p_{O_2} = e^{(2\Delta G_r^\circ / y\mathrm{R}T)} \tag{2.6}$$

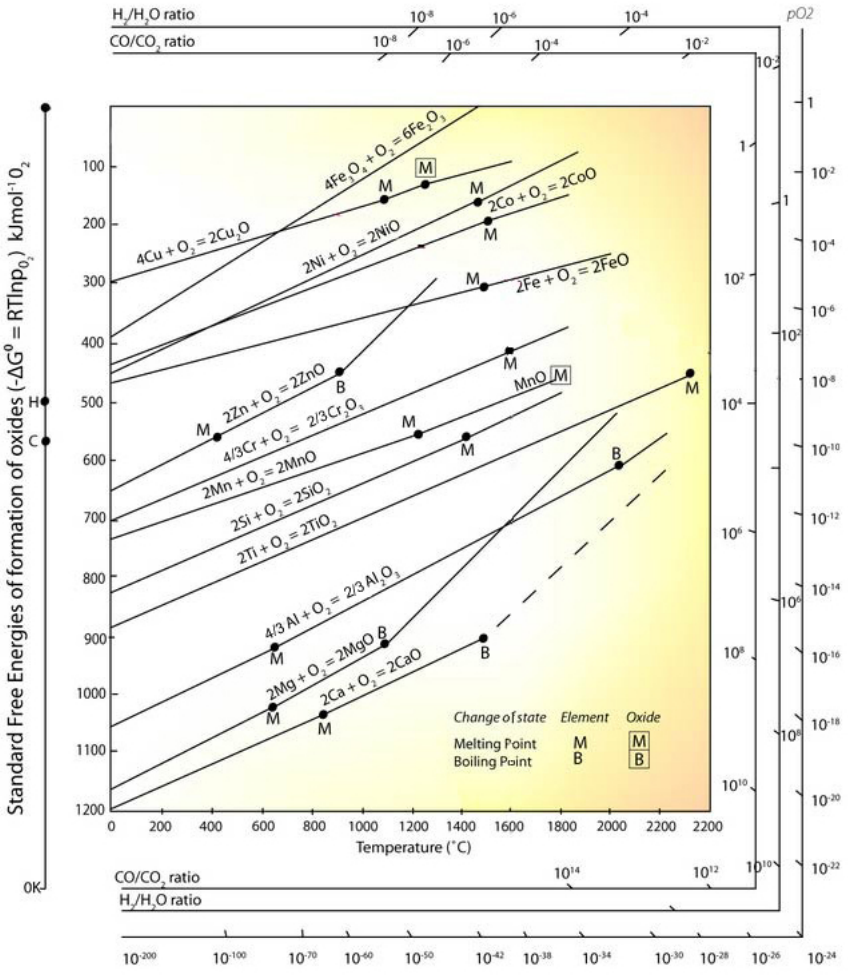

Figure 2.2: Ellingham-Richardson diagram. Standard free energy of formation for selected oxides as a function of temperature.[8]

The oxygen partial pressure where metal and oxide are in equilibrium is called the dissociation pressure. If the p_{O_2} is higher than the dissociation pressure of the oxide, the oxide will be stable. Equation 2.6 can thus be used to calculate the thermodynamical stability of metals or oxides at a set p_{O_2} and temperature. The stability of oxides at different temperatures can be compared in an Ellingham-Richardson diagram. The Ellingham-Richardson diagram is constructed by plotting the free energies for formation of different oxides as a function of temperature, as seen in figure 2.2. The stability of oxides increases in the negative direction of the y-axis in the diagram, and the stability of metals will hence increase in the positive direction of the y-axis.

2.3 Defects in oxides

Oxides and other crystalline materials will contain lattice imperfections, or defects, at high temperatures. These defects will enable ion transport in the material, and thus influence both oxide growth mechanisms and rate kinetics. This section will first explain how the defect situation in a crystalline material may be described by defect chemical reactions, then the probable defect structures in Cr_2O_3 and (Cr, Mn)$_3O_4$ will be deduced. Cr_2O_3 and (Cr, Mn)$_3O_4$ are the expected dominating phases in Fe-Cr alloys with an addition of Mn,[9] similar to the alloy used in the experimental work of this study. The defect chemistry in this section is retrieved from "*Defects and Transport in Crystalline Solids*" by Per Kofstad and Truls Norby.[10]

To achieve a configuration of minimum energy, atoms or ions in crystalline solids are assigned specific sites in the structure. At absolute zero temperature there are as such no defects present, and the structure is defined as ideal. As the temperature rises, defects are introduced in the crystal structure. The ideal structure is used as a reference state, and any deviation from it will be regarded as defective. This could be excess or deficiency by either oxygen or metal, compared to what would be expected for a perfect lattice structure. Defects can be limited to one lattice site, extended over several sites or be electronic. Electronic defects, such as defect electrons or electron holes, are not constrained to specific lattice sites. Defects limited to one lattice site are called point defects. Point defects include vacant lattice sites, or vacancies, interstitial atoms and substitutional atoms. Extended defects can either be one-dimensional, such as grain boundaries and dislocations, two-dimensional planes or three-dimensional precipitations or pores. Grain boundaries or other extended defects are often rapid diffusion paths for ion transport. An illustration of different defects present in a crystallographic lattice can be seen in figure 2.3.

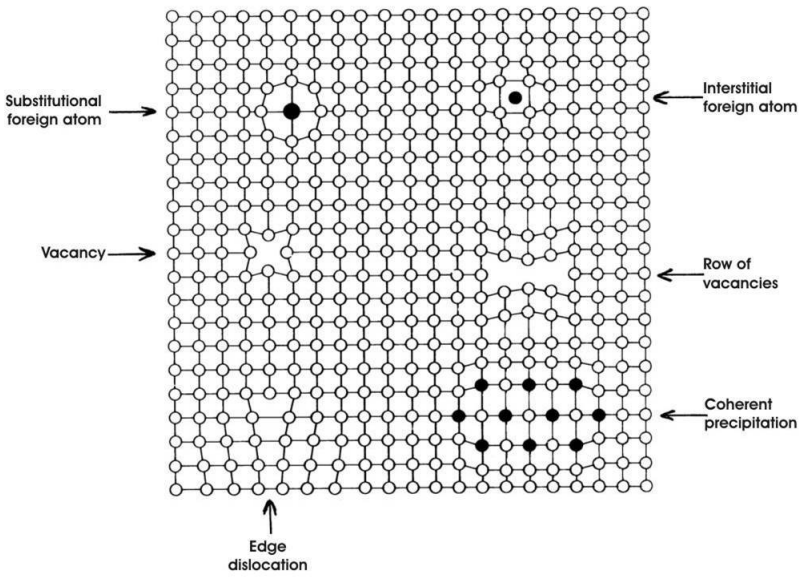

Figure 2.3: Schematic illustration of selected defects in a crystallographic lattice, adapted from Kofstad and Norby.[10]

2.3.1 Kröger-Vink notation

The defect situation in a crystalline material can be described by defect chemical reactions, where reactants form to give products in a similar way as conventional chemical reactions. In the bulk, ionic transport will proceed by point defects. These point defects may be formed either by interaction with gases from the surroundings, for instance oxygen, or without external influences. The resulting defect reactions are referred to as external or internal defect reactions, respectively.

The notation used in defect chemistry to describe defect chemical species is Kröger-Vink notation, proposed by F. A. Kröger and H. J. Vink in 1956.[11] Each defect is denoted as A_s^c, where A is the chemical species, s indicates the lattice site and c is the effective charge of the species. The effective charge is the real charge of the defect, subtracted the charge the site would have in the ideal structure. A positive effective charge is denoted with a bullet symbol $^\bullet$, and negative effective charge with $'$. Neutral effective charge is denoted with the symbol ^{X}.In this way, oxygen vacancies may be written as v_O and metal interstitials as M_i. If the oxygen vacancies have positive effective charges, the notation then will be $v_O^\bullet$ or $v_O^{\bullet\bullet}$ if the vacancy is singly or doubly charged.

2.3.2 Formation of defects

When treating defect chemical equilibria, some assumptions must be made. It is assumed that defect concentrations are small enough for the defects not to interact. In addition, it is assumed that all sites are energetically equal. When these two requirements are fulfilled, we term the conditions as ideal. Under ideal conditions the equilibrium constant for a defect chemical reaction, K, can be given by the activities or site fractions of the defects. An example of a defect chemical reaction is the formation of oxygen vacancies in equation 2.7.

$$O_O^x = v_O^{\bullet\bullet} + 2e' + \frac{1}{2}O_2 \tag{2.7}$$

The equilibrium constant for this reaction can be expressed as following:

$$K_{v_O} = \frac{a_{v_O^{\bullet\bullet}} a_{e'}^2 a_{p_{O_2}}^{\frac{1}{2}}}{a_{O_O^x}} = \frac{(\frac{[v_O^{\bullet\bullet}]}{[O]})(\frac{n}{N_C})^2(\frac{p_{O_2}}{p_{O_2}^0})^{\frac{1}{2}}}{\frac{[O_O^x]}{[O]}} = (\frac{[v_O^{\bullet\bullet}]}{[O]})(\frac{n}{N_C})^2(\frac{p_{O_2}}{p_{O_2}^0})^{\frac{1}{2}} \tag{2.8}$$

Further simplifications can be made by assuming $[O_O^x] = 1$ and $p_{O_2}^0 = 1$ bar. It is also for simplicity common to neglect $\frac{1}{N_C}$. The resulting expression will then be:

$$K'_{v_O} = [v_O^{\bullet\bullet}]n^2 p_{O_2}^{\frac{1}{2}} \tag{2.9}$$

2.3.3 Defect structure of Cr_2O_3

As previously mentioned, the transport in solids are enabled by defects. In crystalline materials, defects can give rise to movement of atoms, ions and electrons through the material, and electrical, magnetic and optic properties may all vary due to the dominating defects present. As a large number of high-temperature alloys, including the alloy investigated in this work, form a protective scale of Cr_2O_3, it is important to elucidate the defect situation in chromia. The defects present in chromia is assumed to be interstitial chromium and oxygen, chromium and oxygen vacancies, electrons and electron holes. The total electroneutrality of chromia is given in equation 2.10.

$$3[Cr_i^{\bullet\bullet\bullet}] + 2[v_O^{\bullet\bullet}] + p = 3[v_{Cr}^{'''}] + 2[O_i^{''}] + n \tag{2.10}$$

Chromium defects The formation of cation vacancies in Cr_2O_3, see equation 2.11, will occur at the normally occupied octahedral sites in the corundum lattice. At high oxygen partial pressure, it is probable that chromium vacancies and electron holes will dominate the defect structure in chromia:

$$\frac{3}{2}O_2(g) = 2v_{Cr}^{'''} + 6h^{\bullet} + 3O_O^x \tag{2.11}$$

Other defect concentrations can be considered minor, and the electroneutrality in equation 2.10 is reduced to $3[v_{Cr}^{'''}] = p$. At lower oxygen partial pressure, chromium interstials and electrons will most likely dominate:

$$2Cr_{Cr}^{x} + 3O_{O}^{x} = 2Cr_{i}^{\bullet\bullet\bullet} + 6e^{'} + \frac{3}{2}O_2(g) \tag{2.12}$$

The electroneutrality can then be reduced to $3[Cr_i^{\bullet\bullet\bullet}] = n$.

Oxygen defects Oxygen interstitials diffuse slowly in Cr_2O_3 and is thus regarded a minority defect. The presence of oxygen interstitials in the lattice is not likely due to the close packing and the size of an oxygen anion. However, in disordered regions such as grain boundaries and other interfaces they may occur. The formation of oxygen interstitials:

$$\frac{1}{2}O_2 = O_i^{''} + 2h^{\bullet} \tag{2.13}$$

The formation of oxygen vacancies:

$$O_O^x = \frac{1}{2}O_2 + v_O^{\bullet\bullet} + 2e^{'} \tag{2.14}$$

By calculating the p_{O_2} dependencies of the present defect concentrations from the limiting equations above, a Brouwer diagram illustrating the defect concentrations as a function of p_{O_2} can be constructed. A Brouwer diagram for Cr_2O_3 can be seen in figure 2.4.

2.3.4 Defect structure of (Cr, Mn)$_3$O$_4$

Many Fe-Cr alloys will in addition to a Cr_2O_3 scale grow a spinel phase, $(A,B)_3O_4$, during oxidation. This spinel phase will be located on top of the chromia scale, near the gas-oxide interface. For alloys with an addition of Mn, the spinel phase will generally be rich in manganese due to the rapid diffusion of Mn ions through the alloy and the Cr_2O_3 scale.[12] Spinels are in general resistive against oxygen defects, and the total electroneutrality of the spinel can thus be written:

$$2[Mn_i^{\bullet\bullet}] + 3[Cr_i^{\bullet\bullet\bullet}] + p = 2[v_{Mn}^{''}] + 3[v_{Cr}^{'''}] + n \tag{2.15}$$

Interstitial cations are assumed to dominate in spinel phases at low p_{O_2}, while cation vacancies dominates at higher pO_2. The gradient in partial pressure of oxygen, from a maximum at the surface to a minimum in the alloy interior, will affect the spinel defect structure. At the chromia-spinel interface, the oxygen activity is lower and interstitial cations will dominate. In regions of the spinel closer to the gas-spinel interface, p_{O_2} increases and cation vacancies will eventually be in majority.

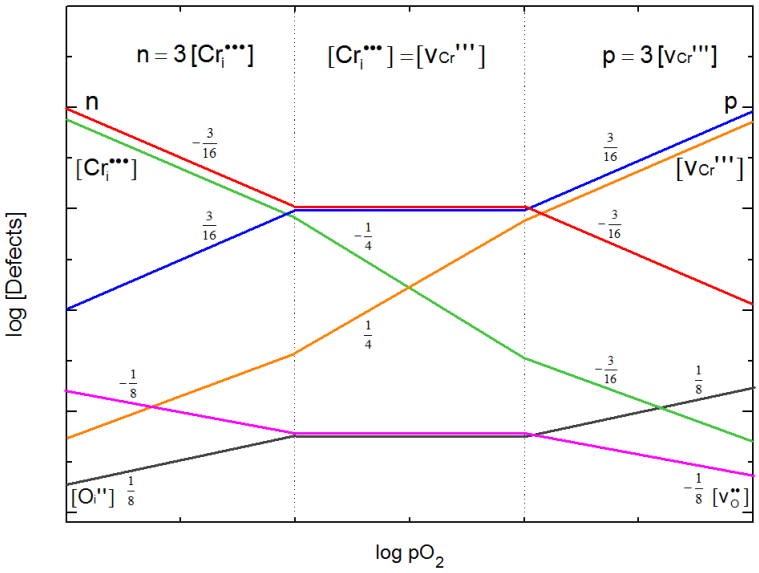

Figure 2.4: Brouwer diagram of pO_2 dependent defect concentrations in Cr_2O_3.

2.4 Diffusion

As mentioned earlier, when a dense oxide scale is completely covering the metal surface, the oxide growth will proceed further by diffusion of reacting species through the scale, see figure 2.5. Diffusion is the process of mass transport of species through a medium. Atoms in a medium will diffuse in a direction which reduce the Gibbs free energy of the system. Diffusion in metals can occur by point defects, substitutionally and interstitially, or by extended defects such as grain boundaries, dislocations or interfaces.

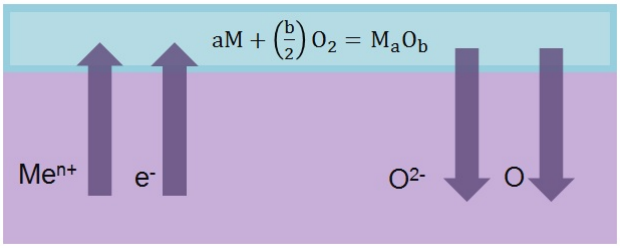

Figure 2.5: Diffusion of reactants through alloy and oxide scale

The transport of atoms by diffusion can be expressed by Fick's first law, which states that the flux, J_i of atoms through an area per time unit is proportional to the concentration gradient. Fick's first law in one dimension can be seen in equation 2.16.

$$J_i = -D_i \frac{\delta C_i}{\delta x} \tag{2.16}$$

In equation 2.16, D_i is the diffusion coefficient of the diffusing species, C_i is the concentration and x is the distance. The direction of the flux is set by the negative sign, as the particles diffuse from an area of higher concentration to lower concentration. The validity of Fick's first law is limited to neutral particles diffusing in a constant concentration gradient. However, in oxides most diffusion particles are charged.

Diffusion of species in the lattice will generally happen by either vacancies or interstitials. The vacancy mechanism can be viewed as ions jumping to vacant lattice sites, while interstitials jump between neighbouring interstitial voids in the crystal structure. Interstitial diffusion is only likely to happen when the interstitial atom is small enough to fit in between atoms at normal lattice sites. Both these mechanisms are illustrated in figure 2.6.

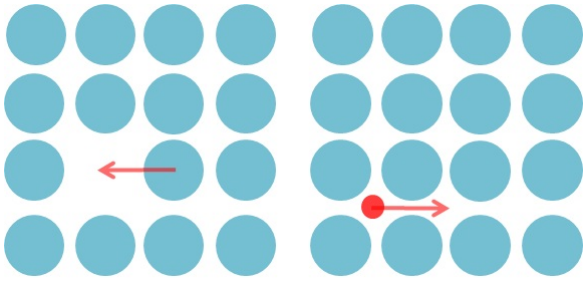

Figure 2.6: Left: Vacancy diffusion, right: Interstitial diffusion

In real materials, ionic transport will be effected by the presence of interfaces. Interfaces are regions structurally different from the bulk material. In disordered regions, such as in grain boundaries, the structure is more open compared to the grain interior, enabling atoms to move more readily. Extended lattice defects such as interfaces and grain boundaries are therefore important rapid short-circuiting diffusion paths for ions in oxides. Due to higher mobilities in these disordered regions, the activation energy for grain-boundary diffusion is in general much smaller than for lattice diffusion. Generally, the same laws can be used to describe lattice diffusion and grain-boundary diffusion. However, diffusion along grain boundaries and other interfaces in multicomponent alloys can be complicated, due to additional segregation effects. This is the tendency of certain metal components to segregate into the grain boundaries[13] or other interfaces, such as in the oxide-alloy interface between the grown oxide scale and the underlying metal surface.

2.5 Oxide scale growth

2.5.1 Wagner's Oxidation Theory

Wagner's oxidation theory relates the parabolic oxidation rate observed for many metals and alloys with the diffusion of reactants through the scale. In an ideal case, this oxide scale is dense, continuous and adherent, completely covering the metal surface. Wagner derived a model for such an ideal case, based on a series of assumptions. However, a detailed description of Wagner's oxidation model will not be given in this work. Wagner's theory is one of the most important contributions in understanding and predicting high temperature oxidation of metals and metal alloys.

Wagner's model for parabolic oxidation is built on the assumption that oxide scales grow by diffusion of reacting atoms through the oxide layer and that this reaction is the rate limiting step in the overall oxidation. The reason for this diffusion to occur, is assumed to be the presence of lattice point defects. As the oxide scale grows, the diffusing distance will increase and the reaction rate therefore decreases with time. One prerequisite for diffusion dominating the oxidation rate, is that reactions occurring at metal-scale and scale-gas interfaces are so fast that they do not contribute significantly to rate control.

One key aspect of Wagner's theory, is that the parabolic rate constant is expressed in terms of independently measurable properties.[10] For instance electronic and ionic conductivity of the oxide, or by self-diffusion coefficients of the reactants. The parabolic oxidation of an oxide M_aO_b by Wagner's

model can be expressed by equation 2.17[1]:

$$\frac{dx}{dt} = \frac{b}{c_O}\frac{dn}{dt} = (\frac{1}{2}\int_{p^1_{O_2}}^{p^0_{O_2}}(\frac{z_{cat}}{2}D_M + D_O)d\ln p_{O_2}))\frac{1}{\Delta x} = k^*_p\frac{1}{\Delta x} \qquad (2.17)$$

where x is scale thickness, c_O is the number of oxide ions per cm^3, z_{cat} is the cation charge and D_M, D_O are the self-diffusion coefficients for the metal and the oxide reactants respectively.

The overall driving energy for the oxidation reaction is the gain in Gibbs free energy when an oxide is formed from a metal and oxygen gas. It will therefore exist a gradient in the partial pressure or activity of oxygen across the oxide scale. This gradient will be at a maximum in the oxidant gas and decrease to a minimum in the metal interior. At the oxide/metal interface this partial pressure will be the decomposition pressure of the oxide in equilibrium with its metal.[10] There will also be a gradient in chemical potential. This gradient is the driving force for transport of chemical species in the system.

2.5.2 Oxidation kinetics and rate laws

Different rate laws can be assigned to oxidation reactions to describe the behaviour as a function of time. Investigation of reaction rates provides valuable information about the dominating reaction mechanism and the rate-controlling process. It is also a good way for comparing actual reactions with theoretical models. Groups of rate laws frequently ocurring in the literature are parabolic, linear and logarithmic oxidation. It is important to state that these are simplifications, and that there in some cases may be difficult to fit experimental rate data to simple rate equations.

For a large number of metals, the oxidation rates follow a parabolic behaviour as a function of time, where rates initially are very fast and then gradually slows down. For this type of oxidation reaction, the scale thickness can be given by

$$\frac{\partial x}{\partial t} = k'_p\frac{1}{x} \qquad (2.18)$$

which after integration as a function of time becomes

$$x^2 = 2k'_p t + C_0 = k_p t + C_0 \qquad (2.19)$$

where x is thickness, k_p the parabolic growth rate constant and C_0 an integration constant. Parabolic dependence as a function of time reflects a

[1]The complete derivation of equation 2.17 will not be provided in this thesis. Interested readers are advised to read chapter 7 in "Defects and Transport in Crystalline Solids" by Per Kofstad and Truls Norby[10]

reaction rate determined by thermal lattice diffusion of one or both reactants through the scale. Parabolic oxide scale growth is often called protective oxidation.

The thickness related parabolic growth rate constant, $k_{p,t}$ and the weight related parabolic growth rate constant, $k_{p,w}$, are related through equation 2.20.

$$k_{p,t} = \left(\frac{M_{M_xO_y}}{b \cdot M_O \cdot d_{M_xO_y}} \right)^2 \cdot k_{p,w} \tag{2.20}$$

Linear oxidation as a function of time is observed when the reaction rate is determined by surface reactions. The reaction rate is then constant with time and independent of previously consumed reactants. A large number of metals oxidized at temperatures below 300 °C to 400 °C show an initially rapid reaction rate, which later is reduced to almost negligible rates.[7] This behaviour has been described by logarithmic rate equations. Linear and logarithmic rate kinetics will not be discussed further in this work.

2.5.3 Temperature dependence of reaction rates

For most chemical reactions, an increase in temperature yields raised reactions rates. In the late 1800s, the Swedish chemist Svante Arrhenius detected that almost all reaction rates have a similar dependence of temperature. The Arrhenius equation may be written as in equation 2.21 or alternatively as in equation 2.22.

$$\ln k_r = \ln A - \frac{E_a}{\mathrm{R}T} \tag{2.21}$$

$$k_r = Ae^{-E_a/\mathrm{R}T} \tag{2.22}$$

In these equations k_r is the rate constant, the parameter A is the called the pre-exponential factor and E_a is the activation energy. R is the gas constant and T the temperature where k_r is measured. By plotting $\ln k_r$ as a function of $\frac{1}{T}$, the y-intercept is $\ln A$ and the slope is equal to $-\frac{E_a}{\mathrm{R}T}$.

2.5.4 The activation energy

The activation energy, E_a, of a reaction may be calculated from the slope of an Arrhenius plot. From equation 2.22 it can be noted that a reaction with high activation energy will give an Arrhenius plot with a very steep slope, and the reaction is thus sensitive to temperature. Reactions with low activation energies will be less sensitive to temperature. A general rule is that the activation energy remains constant when the rate determining mechanism is the same.[7]

2.5.5 The effect of dopants

When oxidizing Fe-Cr alloys at high temperatures, the formed chromia scale is rarely undoped. Alloys consist of various metal constituents, all contributing to give certain desired material properties. These elements may dissolve in the Cr_2O_3 scale as dopants. The introduction of such foreign species will alter the defect structure of the oxide. The effectively charged cations are compensated by oppositely charged defects to ensure electroneutrality. This will thus vary the defect concentrations.

Mn, Ti, Mo, Nb and Ni are examples of common alloying elements. The effect of these constituents on a growing oxide scale will vary, due to factors such as oxygen affinity and mobility. As dopants, these cations may diffuse through interstitial voids or by substitution. Mn can function as a lower valent dopant in chromia, and at high p_{O_2} the following situation may occur:

$$2MnO(s) + \frac{1}{2}O_2(g) = 2Mn_{Cr}^{'} + 3O_O^x + 2h^{\bullet} \tag{2.23}$$

At high partial pressures of oxygen it is therefore assumed that lower valent dopants, such as Mn, will increase the concentration of positive electron holes. Reversly, higher valent dopants such as Ti will increase the concentrations of negative defects. For low levels of pO_2, Mn may dissolve according to:

$$2MlO(s) = 2Ml_{Cr}^{'} + v_O^{\bullet\bullet} + 2O_O^x \tag{2.24}$$

Dopants can also interact with other point defects present in the material and form complex defects. The formation of such complex defects are caused by coulombic attraction between the reacting elements and point defects of opposite charge. To illustrate this phenomenon, one can consider the association between a lower valent dopant, such as Mn ($Mn_{Cr}^{'}$), and oxygen vacancies ($v_O^{\bullet\bullet}$).

$$Mn_{Cr}^{'} + v_O^{\bullet\bullet} = (Mn_{Cr}v_O)^{\bullet} \tag{2.25}$$

The complex defect will have an effective positive charge and a mobility similar to that of the dopant alone. If the dopant is relatively immobile, the oxygen vacancy can be considered trapped in this complex defect.

Hydrogen and water

Hydrogen will dissolve in chromia as protons bound to oxide ions, forming substitutional hydroxide ions $OH_O^{\bullet}$ on oxygen sites, see equation 2.26.

$$\frac{1}{2}H_2(g) + O_O^x + h^{\bullet} = OH_O^{\bullet} \tag{2.26}$$

The same mechanism is probable for water vapour:

$$H_2O(g) + O_O^x + 2h^\bullet = 2OH_O^\bullet + \frac{1}{2}O_2(g) \tag{2.27}$$

The total electroneutrality for the system can be written:

$$[OH_O^\bullet] + 2[v_O^{\bullet\bullet}] + 3[Cr_i^{\bullet\bullet\bullet}] + p = 3[v_{Cr}^{'''}] + n \tag{2.28}$$

It can be seen from equation 2.28 that as hydrogen or water enters the oxide as a positive dopant, the concentration of other positive defects will decrease.

Chapter 3

Literature

3.1 The use of metals in society

As stages of human prehistory is referred to as the bronze age and the iron age, it is evident that metals and alloys have had a significant role in the development of our society. 250 years ago, the industrial revolution drastically changed the daily lives of our ancestors. Machines and other advanced equipment were introduced to both agriculture and the industry, leading to more automated and efficient work. The human dependence upon metals is obvious when taking a glance at our industry, homes or means of transportation. The construction of airplanes, cars, buildings or electric lighting are all enabled by metal alloys.

Today the world's most important construction material is steel, with a global production of above 1,414 million tons annually.[14] Steel is made by combining iron with other elements, of which carbon is the most common. The addition of carbon or elements such as Mn, Si, Ni or Cr prevent the movement of dislocations and will thus harden the steel. By varying the amount of alloying elements, and also the form in which they are present, material properties such as ductility and strength can be controlled.

3.2 Fe-Cr alloys

Iron is the cheapest and one of the most commonly used construction materials in the world. However, iron is not suitable for high temperature applications due to its very low stability in oxidizing surroundings. If iron is to be used at high temperatures, a slow growing and protective oxide scale should be formed to avoid critical degradation of the material. This can be accomplished by the addition of chromium. If the chromium content in the alloy is sufficiently high, the formation of the very stable oxide Cr_2O_3 will be

preferred. The process where oxidation of one alloy constituent to form an external protective scale is preferred, is referred to as *selective oxidation*.[7]

When an Fe-Cr alloy is exposed to oxidizing conditions, both iron and chromium will react to form oxides, but at different rates. Initially, the oxidation process is dominated by surface interactions between the alloy and the gaseous surroundings. For Fe-Cr alloys with a high chromium content (20-27 wt.%), the formation of a protective chromia scale at the surface becomes favourable. The critical level of Cr required to sustain the growth of a protective chromia scale is about 17 wt.%, but commercial high temperature alloys contain an excess to ensure a sufficient level of Cr.[15] If the chromium concentration after a time is lower than the critical limit, there is an insufficient amount of Cr available to continue the formation of a protective Cr_2O_3 scale. When this occurs an acceleration in oxidation rate, called *breakaway oxidation* may be observed.

Ferritic stainless steels usually have chromium contents of 12-30 wt.% and low carbon levels, less than 0.25 wt.%. Ferritic stainless steels are used in applications such as washing-machine drums and exhaust systems. It is also evaluated as a candidate for fuel cell interconnects, which is the aim of this thesis. A common problem with chromium containing steel is the formation of volatile chromium species, such as CrO_3 and $CrO_2(OH)_2$ under high temperature oxidation.[7] These gaseous species lead to metal loss and subsequently degradation of the steel.

Much work has been done on the oxidation of unalloyed Cr, to compare chromia growth mechanics of pure Cr to what is observed for chromium containing alloys. The growth of Cr_2O_3 scales on pure chromium is similar to the chromia growth on Fe-Cr alloys, which could indicate that the same oxidation mechanism is dominating both systems.[7] The oxidation kinetics of chromium above 700 °C seem to follow the parabolic behaviour expected in protective stages of oxidation.[16]

3.3 Fuel cell interconnect materials

A fuel cell stack consists of multiple cells connected in series to gain usable power. Each individual cell is separated in the stack by plate components called interconnects. The interconnect is designated to separate the fuel side in one cell from the air side of the next, and in addition provide electrical contact between the cells.

3.3.1 Interconnect requirements

The interconnect must withstand both oxidizing and reducing conditions at high temperatures during the entire range of its lifetime. In addition, the material must have high electronic conductivity, sufficient mechanical strength and be completely gas tight. If a material is to perform satisfactory as an interconnect in a fuel cell stack, certain requirements must be fulfilled:[1,17]

- High electronic and low ionic conductivity
- Chemical stability under oxidizing and reducing conditions
- Chemical stability towards other cell components
- High mechanical strength
- Suitable thermal expansion coefficient
- High thermal conductivity
- Simple fabrication route and good machinability
- Low cost

The minimum electrical conductivity accepted by fuel cell interconnect materials is 1 S/cm.[1] Ideally, resistance loss through the stack should be no more than through an individual cell. The conductivity of ions must be very low, as reduction in partial pressures of oxygen and hydrogen from such a leakage would decrease the open circuit voltage, and thus seriously affect the cell efficiency. Chemical stability under reducing and oxidizing conditions, and towards other cell components, is crucial as material changes will introduce stresses, strains and also affect the electrical conductivity of the interconnect over time. The partial pressure of oxygen will vary from 10^{-4}-$10^{-0.7}$ atm on the cathode side to 10^{-18}-10^{-8} on the anode side.[1] Any structural change caused by these p_{O_2} gradients could introduce enough mechanical stress to cause cracking and eventually lead to cell malfunction. The thermal expansion coefficients (TEC) of all fuel cell components have to match, as too large a difference could lead to mechanical and electrical breakdown of the system. The thermal conductivity must also be relatively good, and the lowest accepted value is 5 $Wm^{-1}K^{-1}$.[18]

As the interconnects are the main structural elements of the fuel cell stack, the mechanical strength must be sufficient to hold the other fuel cell components at operating temperatures. The last, and possibly the key requirement, is to keep the cost of the interconnect at a minimum. This requires both low raw material cost and a cheap mass-production

manufacturing process. If fuel cell systems are to be successfully commercialized, the total cost of the unit must be economically competitive. The two main groups of materials considered as of today, are ceramics and metals. The following section will summarize the main advantages and challenges regarding the two groups of potential interconnects.

3.3.2 Ceramic interconnects

In the early stages of solid-oxide fuel cells, operating temperatures exceeded 1000 °C. This excluded the use of almost any material as interconnects, except ceramics. The demanding requirements for interconnect materials still eliminated almost all groups of oxides, except lanthanum chromites. $LaCrO_3$ is the most common ceramic interconnect material due to high electronic conductivity in both fuel and oxidant atmospheres, good chemical stability and compatibility with other cell components.[19]

Ceramic interconnect materials have complicated fabrication routes, which increase the cost drastically. They are also very brittle and have limited mechanical strength. As the development of fuel cells moves towards lower operating temperatures, this will enable the use of cheaper materials such as commercial alloys. Ceramic interconnect materials will therefore not be discussed further in this work.

3.3.3 Metallic interconnects

Metallic interconnects have great potential due to high electronic and thermal conductivity, low cost and easy fabrication. One obvious problem with metallic interconnects operating under oxidizing and reducing conditions is the formation of oxide scales. This is inevitable at high temperatures under such conditions, and can drastically reduce the performance of the fuel cell stack. To ensure satisfying performance and efficiency, it is vital to have the lowest possible resistance through the fuel cell stack. The oxide scales must also match the other requirements for interconnect materials to ensure optimal performance.

The two most promising groups of candidates as of today, are nickel based chromium bearing alloys and Fe-Cr alloys.[20,21] Chromia forming alloys are less resistant against oxidation at high temperatures than Al_2O_3 forming alloys, but the electrical conductivity of chromia exceeds alumina by orders of magnitude.[20,22] The main problem with using chromium containing alloys as interconnects, is the evaporation of volatile Cr species under operating conditions. The presence of chromium species at the electrodes, especially the cathode side, will seriously damage the electrochemical performance of the fuel cell. The volatilization of Cr_2O_3 can be inhibited by the addition of

alloying elements, or protective surface coatings, that favour the formation of a stable oxide on top of the chromia scale.

Alloys such as *Inconel 600,Haynes 230* and *Haynes 242* are among the best nickel based alloys for interconnect purposes.[18] Generally, the oxidation rates of Ni-Cr alloys are slow and the electrical conductivities of the resulting oxide scales are quite high.[23] The oxidation rates of Ni-based alloys tend to be lower than those for Fe-Cr alloys.[18] The main problem for nickel based chromia forming alloys is that their thermal expansion coefficients are generally too high to successfully match with other fuel cell components.[23] As a result, this group of alloys is essentially excluded as potential interconnect materials and will not be further discussed in this work.

One of the most commonly used Fe-Cr alloys for SOFCs is *Crofer 22 APU* from ThyssenKrupp VDM, specifically designed to meet the requirements for metallic interconnect materials. Crofer 22 APU has a composition of Fe-22%Cr with additions of Mn, Ti and La.[24] The parabolic growth rate constant for Crofer 22 APU at 800 °C is reported in the range of $4.8{\cdot}10^{-14}$ to $6.5{\cdot}10^{-14} g^2/cm^4 s$.[25,26] The alloy chosen for this work, Sanergy HT, is a Fe-22%Cr alloy also designed specifically for interconnect purposes.

Another group of potential interconnects are alloys based on chromium. Cr based alloys doped with dispersed oxides, such as *Ducrolloy* (Cr-5%Fe-1Y_2O_3), show especially low weight change as function of time.[18] However, the fabrication process of Cr-based alloys are expensive. Iron based chromium bearing alloys are therefore the best metallic interconnect materials so far, until the cost of Cr-based oxide-dispersion strengthened (ODS) alloys is sufficiently decreased.

Effect of alloying additives in Fe-Cr alloys

Small amounts of different elements are often added to alloys to achieve or improve certain desired material properties. The effect these elements have on the oxidation properties of Fe-Cr alloys is of great interest. Alloying components such as Si, Al, Mn or Ti can not only impact the properties of the Fe-Cr alloy, but also the crystal structure and composition of the oxide and the oxide-alloy interface. Adding minor amounts of certain elements have proved to show various effects:[27,28]

- Formation of new oxide phase in the outer layer of the external oxide scale or in the inner layer of the material
- Change in defect concentrations, electrical conductivity or physical properties

Table 3.1: Conductivities of cobalt spinels[31]

	σ
Co_3O_4	6.0 S/cm
Co_2MnO_4	60 S/cm
$CoMn_2O_4$	6.4 S/cm
Mn_3O_4	0.1 S/cm

- Change in adhesive properties of oxide and oxide-alloy interface

Mn is an element often added to alloys. Manganese has a diffusion rate in chromia at 900 °C which is two orders of magnitude faster than Fe or Ni.[12] The tendency is thus for Mn to diffuse through the Cr_2O_3 scale of Fe-Cr alloys to form an outer layer of $MnCr_2O_4$ spinel. Titanium added to chromia forming alloys has a tendency to oxidize to the very stable TiO_2 at the scale surface, the oxide-alloy interface or in grain boundaries.

Alloying elements may segregate to grain boundaries, and other interfaces, altering oxide growth rates.[29] As many alloying elements will occupy chromium sites in oxides formed on Fe-Cr alloys, this may affect the outward chromium transport and subsequently the oxide growth rate. The segregation of alloying elements to interfaces can lead to physical blocking by elements, or their oxides, in the grain boundaries, and the formation of complex defects.

3.3.4 Protective coatings

Surface coatings can be applied in the attempt to alter and improve the oxidation behaviour of interconnect materials and metals in general. The use of commercial alloys would be economically desirable, but this will require finding solutions for several critical issues leading to degradation of the fuel cell stack. The problems arise especially on the cathode side, with increasing contact resistance and the evaporation of volatile chromium species poisoning the cathode.[30]If stainless steel interconnects are to be used in fuel cell systems, this process must be prevented.

The desired effects of coatings include reduced oxide growth rates, increased conductivity of the scale, enhanced metal-oxide adhesion and to avoid evaporation of volatile Cr species.[30] There are numerous types of coatings tested in recent literature, including reactive element oxides (REO), rare earth perovskite and conducting spinels.[30] Reactive element oxides have been found to significantly reduce oxidation rates and improve metal-oxide adhesion.[30]

A surface coating of cobalt can reduce oxidation rates and also form (Co, $Mn)_3O_4$ and Co_3O_4 which prevent chromium evaporation. In addition to preventing chromium evaporation, the formed cobalt spinel layer increase the surface conductivity. The conductivities of different cobalt spinels are given in table 3.1. Although coatings can be used to modify and improve desired oxidation properties, they may also affect the transport processes in the metal. The coatings can lead to doping of the scale, which may change the the conduction mechanism compared to an uncoated alloy.[18] The total cost of an interconnect will not be significantly increased by applying a surface coating, as protective coatings may enable the use of less expensive alloys. Coatings can thus provide a relatively cheap and efficient method to improve the oxidation properties of ferritic interconnect materials at high temperatures.

3.3.5 Volatile Cr species

Cr_2O_3 is the only solid chromium oxide thermodynamically stable at high temperatures.[7] High temperature oxidation of chromium containing alloys can thus lead to evaporation of volatile Cr species, such as CrO_3 and $CrO_2(OH)_2$. The formation of CrO_3 (g) in dry conditions:

$$Cr_{Cr}^{x} + \frac{3}{2}O_2(g) = v_{Cr}^{'''} + 3h^{\bullet} + CrO_3(g) \tag{3.1}$$

The evaporation rate of CrO_3 is proportional to $p_{O_2}^{\frac{3}{4}}$,[7] and the CrO_3 evaporation is thus most important at high partial pressures of oxygen. In wet atmospheres, $CrO_2(OH)_2$ (g) is formed by:

$$Cr_{Cr}^{x} + \frac{3}{2}O_2(g) + H_2O(g) = v_{Cr}^{'''} + 3h^{\bullet} + CrO_2(OH)_2(g) \tag{3.2}$$

The chromium loss caused by evaporation increases the degradation rate of the material, and evaporated chromium species may also lead to cathode poisoning if the alloy is used as an interconnect in a fuel cell system.

3.4 Cr_2O_3

Many high-temperature applications use iron-based alloys with chromium as a major constituent. This is largely due to the formation of the slowly growing, protective Cr_2O_3 scale on the metal surface. The crystal structure of chromia can be seen as hexagonally close-packed oxygen anions with chromium cations occupying two thirds of the octahedral sites. This is referred to as the corundum structure.

3.4.1 Electrical conductivity

Cr_2O_3 is an electronic conductor. Young et al.[32] found chromia to be a p-type conductor at high p_{O_2} and a n-type conductor at low oxygen partial pressures. However, Young et al. were unable to change from *p*- to *n*-conductivity by reducing the oxygen activity. Holt and Kofstad[33,34] found the conductivity of Cr_2O_3 to be divided in one high temperature region (>1000-1200 °C) and one low temperature region (<1000-1200 °C) of lower activation energy. Conductivity measurements conducted by Holt and Kofstad showed no p_{O_2} dependence at temperatures above 1000 °C, indicating that chromia at high temperatures is dominated by intrinsic electronic equilibrium:

$$n \cdot p = K_i \tag{3.3}$$

Here n and p represent electron concentration and electron hole concentration, and K_i is the equilibrium constant. At temperatures below 1000 °C, Holt and Kofstad found chromia to exhibit p-type conductivity.

3.4.2 Diffusion in chromia

The growth of chromia on alloys is governed by the diffusion of ions through the oxide scale. As ion transport in oxides are enabled by the presence of crystallographic defects, as discussed in section 2.3, understanding the defect structure of Cr_2O_3 is necessary. Defect chemical equations regarding the formation of chromium and oxygen defects in chromia were given in section 2.3.3.

In pure chromia, the diffusing species governing the oxide growth are chromium and oxygen ions. Early studies on the self-diffusion of chromium and oxygen in polycrystalline samples of Cr_2O_3 at high temperatures, from 1100 °C to 1600 °C, have been reviewed by Kofstad.[7] The self-diffusion of chromium was suggested to be about three orders of magnitude faster than that of oxygen. Later studies on single crystals of Cr_2O_3 did however show that the self-diffusion coefficients of Cr go through very low minimum values at certain oxygen activites. A summary of the Cr tracer diffusion coefficients in chromia as a function of temperature and oxygen activity can be seen in figure 3.1, retrieved from Kofstad.[7] The activation energy for Cr diffusion in Cr_2O_3 has been determined to approximately 245 kJ/mol.[35] The diffusion coefficients are believed to represent lattice diffusion of chromium. As measurements on single crystal samples of Cr_2O_3 showed reduced Cr diffusion coefficients, it is suggested that the early studies on polycrystalline samples were significantly influenced by grain boundary diffusion of chromium. Sabioni et al.[36] suggest Cr diffusion coefficients in Cr_2O_3 to be independent of p_{O_2}. Although this is not confirmed by other reports, the measurements in figure 3.1 also indicate large regions where

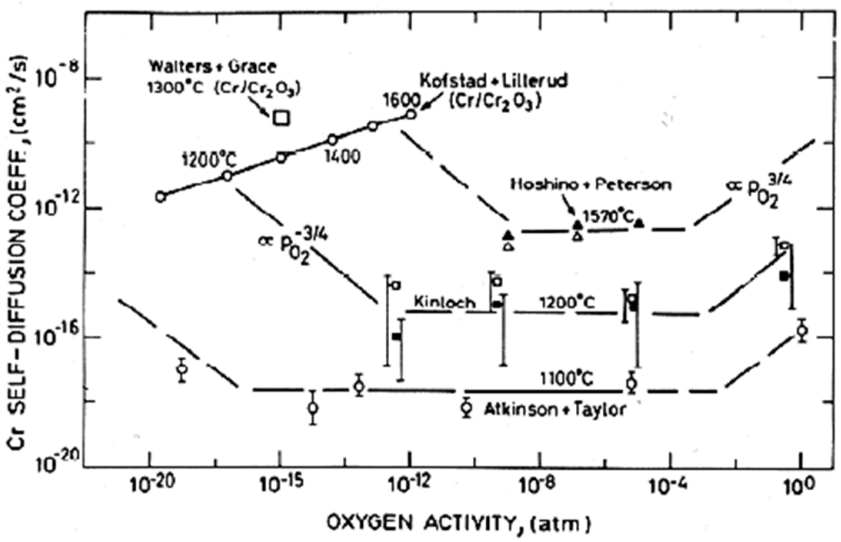

Figure 3.1: Chromium self-diffusion coefficients in Cr_2O_3 as a function of temperature and oxygen activity.[7]

chromium diffusion coefficients are nearly independent of p_{O_2}. The reason for this is unclear, and from the available experimental data no conclusion about the p_{O_2} dependency of chromium diffusion coefficients in Cr_2O_3 can be made.

The diffusion of oxygen in chromia was initially found to be several orders of magnitude slower than that of chromium.[7,12] However, later studies by Sabioni et al.[36] found the oxygen self-diffusion coefficients, both in the lattice and in grain boundaries, to be greater than that of chromium. The activation energy for oxygen diffusion in Cr_2O_3 was reported to 230 kJ/mol, which is slightly lower than that of chromium. Oxygen diffusion should thus become increasingly important with decreasing temperature.

3.4.3 Growth mechanisms

The growth mechanism of Cr_2O_3 scales is a debated topic. The scale growth can proceed by outward diffusion of chromium, inward diffusion of oxygen or a combination of the two. In addition, the inward and outward ion transport can occur through lattice positions or by rapid diffusion paths such as grain boundaries and dislocations. Chromia scales are generally assumed to grow by predominately outward Cr diffusion. Caplan and Sproule[37] concluded that the formation of a monocrystalline Cr_2O_3 oxide scale grows by outward diffusion of Cr ions. However, Atkinson and Taylor[38] suggested that chromia growth rates are too fast for growth by outward Cr diffusion only. Lobnig et al.[12] suggests a significant contribution by inward diffusing oxygen. Kofstad[7] and Tsai et al[39] indicate that Cr_2O_3 scales grow by counter-current diffusion of Cr and O, mainly along grain-boundaries. The oxide scale will grow both normal to and parallel with the metal surface, and the two-way diffusion of anions and cations can lead to compressive stresses, strains and cracking of the scales.[7]

3.4.4 Impurities and dopants

As alloys contain a number of different alloying elements, the diffusion of elements such as Mn, Fe, Ni or Co through chromia is also important to investigate. Ferritic alloys with an addition of elements such as Mn or Co will form a spinel phase on top of the stable Cr_2O_3 scale. This is suggested to be a result of very rapid diffusion of these elemens.[12] Lobnig et al[12] measured diffusion coefficients through Cr_2O_3 grown on Fe-20Cr and Fe-20Cr-12Ni alloys. The general trends in their measurements were that the diffusion coefficients for Fe, Cr and Ni are in the same range, while the Mn diffusivity in the lattice is about two orders higher.[12] Diffusion coefficients of Cr in H_2+H_2O mixtures are reported to be larger than in CO+CO_2 mixtures,[7] suggesting that hydrogen enters as a dopant in chromia and significantly affects the defect structure of the oxide, even at higher temperatures.

3.5 High Temperature Environmental Scanning Electron Microscopy

Much information can be provided by investigating a process as it happens, compared to only examining the inital state and end results. High Temperature Environmental Scanning Electron Microscopy (HT-ESEM) is a technique of great potential, while it is not commonly used in corrosion studies. Usually, samples are heated and oxidized, before later cooled down and examined. In such ex-situ experiments, it is impossible to tell exactly when or how an event occurs. In-situ experimental techniques, such as HT-ESEM, can provide knowledge in initial stages of growth and microstructural

changes that are previously unknown. A variety of in-situ techniques are available and widely used as of today, such as TG, in-situ XRD, conductivity measurements and Transmission Electron Microscopy (TEM). The use of HT-ESEM is on the other hand quite limited.

Schmid et al.[40] investigated the oxidation of pure nickel and chromium in oxygen or water vapour at 700 °C using in-situ ESEM. They found the oxide formation in pure oxygen to be a fine-grained, dense layer, while water vapour atmosphere lead to the formation of chromium whiskers. Whiskers are believed to be favoured when cation lattice diffusion is very slow and an oxidant with the ability to decompose fast on the oxide is available.[40] The growth of whiskers in water vapour atmosphere was also reported by Schmid et al.[41] for the oxidation of pure iron at 700 °C, and by Jonsson et al.[42] for pure iron at 500 °C.

As the maximum pressure obtainable by ESEM is much lower than ambient pressure, it can be questioned if the results achieved during HT-ESEM experiments are comparable to ex-situ experiments under atmospheric conditions.[43] In addition, the effect of a water vapour atmosphere, low vacuum and an electron beam on the oxidation behaviour must be acknowledged. The presence of water vapour is known to alter the oxide scale growth on alloy surfaces by increasing the corrosivity of the environment.[42] The image quality obtained by HT-ESEM has also been reported to decrease as a function of oxide scale thickness, due to the reduction in electrical conductivity.[40]

Chapter 4

Experimental

4.1 Introduction

This chapter will describe the methods and procedures used during the experimental work of this thesis. The main experimental route included sample preparation, oxidation and subsequently characterization of the formed oxide scales. All experiments in this thesis were conducted on samples of a multicomponent Fe-Cr alloy, Sanergy HT from Sandvik. This high-temperature alloy is specifically designed for interconnects in fuel cell applications. The steel samples were either uncoated, or had an applied protective coating of 600 nm Co. The chemical composition of Sanergy HT is presented in table 4.1.

Table 4.1: Nominal Composition of Sandvik Sanergy HT (wt.%)

Cr	Mn	Si	Mo	Nb	Add.	Fe
22	$\leqslant 0.50$	$\leqslant 0.30$	1.0	0.75	Ti	Bal.

4.2 Thermogravimetry

Thermogravimetry (TG) is a method measuring the weight change of a sample as a function of time or temperature, when a sample is exposed to a controlled atmosphere. This is one of the most common methods to investigate oxidation of metals. As a metal oxidizes, the measured weight change will reflect the oxide scale growth. From the resulting data, the overall kinetics may be analysed to determine which processes are dominating the reaction rates.

Both temperature and gas composition could be varied during measurements. To enable the use of different gas compositions, the thermobalance

used in this work was connected to a gas mixer. All TG measurements were conducted under isothermal conditions in the range of 800-1000 °C, in 5 % H_2+Ar, O_2+Ar and pure O_2. The maximum water vapour content was a p_{H_2O} of 0.025 atm. In this work, this is referred to as "wet" conditions.

4.2.1 Instrumentation

The TG measurements were done using a C.I. Electronics MK2 Microbalance with a 0.1 μg sensitivity and a maximum load capacity of 5 grams. The sample was hanging freely on a platinum wire connected to the instrument's balance arm, counterbalanced by weights. The counterweights were located inside a glass tube, while the sample was positioned inside a resistance heated AC furnace. The conditions in the AC furnace were isothermal and isobaric. The temperature was monitored by a thermocouple, and the ambient gas composition was given by the connected gas mixer. The flow rate from the gas mixer to the reaction chamber was controlled by a ball flow meter.

Measurements in reducing atmospheres required some additional steps to minimize the risk of leakages. The sample was suspended inside a long glass tube connected to the instrument, ensuring a gas-tight system. Prior to the experiments, the entire system was flushed with inert gas (Ar) before introducing the hydrogen containing gas mixture. The program *LabWeigh* was used to graphically display data while measuring. Later the data was examined using the graphing and data analysis software *Origin*.

4.2.2 Sample preparation

The samples were made from a 0.2 mm thick foil of Sanergy HT, measured and cut to dimensions of 1.40 x 1.90 cm^2. A hole of 2 mm in diameter was drilled for suspension. Each sample was finally cleaned in ethanol and dried by compressed air before suspended into the furnace at isothermal temperature.

4.3 The gas mixer

It is desirable being able to vary and control the surrounding atmosphere of samples during measurements. In this thesis the gas composition for all thermogravimetric measurements was controlled using a gas mixer. The gas mixer consists of several connected pressure meters, with the possibility to inlet various gases. By mixing oxygen and argon, the oxygen partial pressure in the system can be varied. As the argon gas used in this work is assumed to have an oxygen impurity level of about 10 ppm, the minimum partial pressure of oxygen in a oxygen-argon mixture is $1 \cdot 10^{-5}$ atm.

The water vapour partial pressure can be varied by leading the gas mixture through a wetting or drying stage. The wetting stage consists of one container of pure H_2O and one container of a saturated KBr solution. The p_{H_2O} of the gas mixture after passing through the KBr solution will be 0.025 atm at 25 °C. The drying stage is a container of P_2O_5 salt which will absorb water from the gas mixture. However, due to possible leakages elsewhere in the system, it is assumed that approximately 30 ppm H_2O can be present although the gas mixture is lead through a drying stage. In this work, the gas mixtures used will hereafter be named "wet" or "dry" to specify their water vapour content. Under reducing conditions, a mixture of wet 5 % H_2 and argon was used. The program *GasMix* was used in calculating partial pressures of gases by specifying the gases and types of flow meters present in the system.

4.4 High Temperature Environmental Scanning Electron Microscopy

High Temperature Environmental Scanning Electron Microscopy was used for in situ investigation of the oxide growth on Sanergy HT. As many different parameters influence the image quality and the results obtainable by HT-ESEM, both the instrumentation and the execution of the experiment can be complex. This section will provide an overview of general principles of the technique and the instrumental setup. Instructions and technical specifications given in this section is retrieved from "Options Manual FEI XL 30 SEM" by FEI Company.[44]

4.4.1 Instrumentation setup

Scanning electron microscopes are most commonly used for room temperature experiments, and many of the components are not customized for elevated temperatures. High temperature experiments in a SEM will therefore involve both exchanging temperature sensitive components and installing a complete high temperature system. The high temperature system itself consists of several components:

- Heating Stage Module (HSM)
- High Temperature Stage Controller (HTSC)
- Water Flow Box (WFB)
- Heat Shield Assembly for 1500 °C (HSA)
- Bias Supply Controller (BSC)
- High Temperature Gaseous Secondary Electron Detector (HT-GSED)

A schematic illustration of the components in the HT-ESEM system is given in figure 4.1. The heating stage used was a resistance heated furnace custom

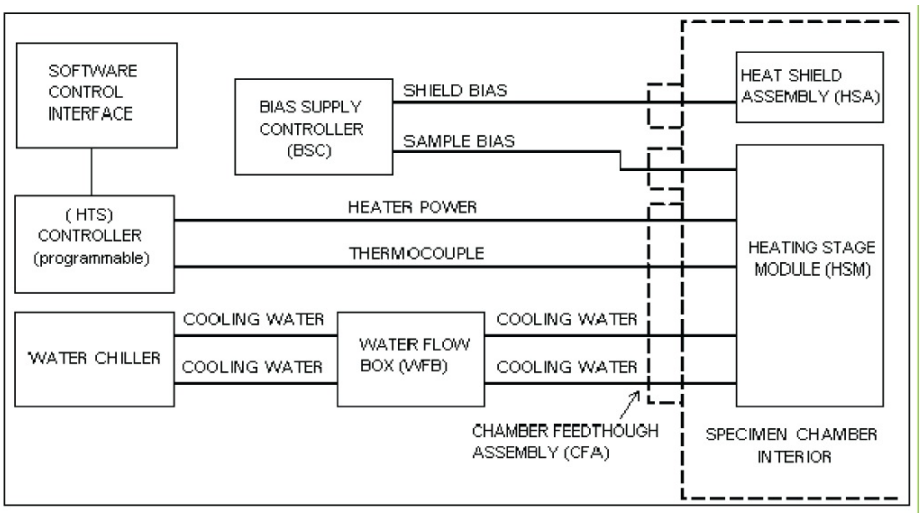

Figure 4.1: Schematic diagram of HT-ESEM instrumentation for FEI Quanta 200F[44]

build for FEI instruments. The heating stage module has a heating rate in the range of 1-50 °C/min and can reach a maximum temperature of either 1000 °C or 1500 °C. To measure the temperature, a thermocouple specific for the furnace was used. The thermocouple for the 1000 °C furnace is B-type, while the 1500 °C furnace uses a K-type thermocouple. In this work, all experiments were done using a 1500 °C HSM. The heating stage was cooled by water flow, monitored by a connected WFB.

Thermally excited electrons severely affect the image quality obtained for heated samples. To reduce the effect of thermal electrons, a bias was applied. Depending on whether the applied bias is positive or negative, electrons will be promoted or suppressed. The high temperature system includes both a heat shield bias and a sample bias. For experiments at temperatures below 400 °C, an applied heat shield bias is not necessary. The complete HT-ESEM setup inside the Scanning Electron Microscope at high temperature can be seen in figure 4.2.

4.4.2 Sample preparation

The steel foil samples were cleaned with ethanol, dried by pressurized air and then cut in circular pieces of $\sim$ 2 mm diameter. The sample was mounted on top of an alumina crucible and glued in place by platinum ink to ensure connection between the sample and the applied bias. The alumina

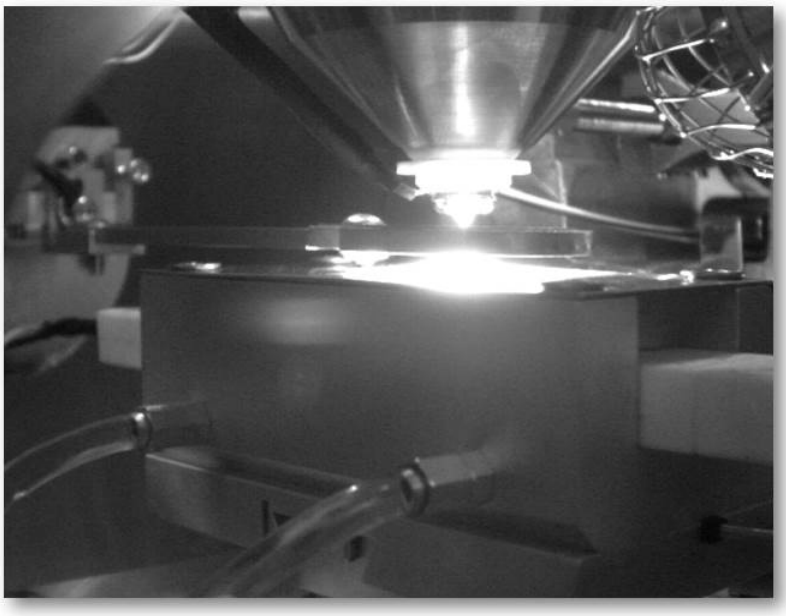

Figure 4.2: HT-ESEM instrumentation viewed from inside the sample chamber of a Scanning Electron Microscope at high temperature.

crucible will shrink over time, and as a result it will not sit tightly. When the temperature increases, this could cause severe vibrations. To reduce the effect of vibrations on the imaging quality, alumina paper was inserted between the crucible and the heater to ensure a tighter fit.

4.4.3 Experimental execution

The samples were oxidized both isothermally and by varying the temperature from 500 °C to 900 °C. The isothermal experiments had a temperature range from 600 °C to 900 °C, where the experiment at each temperature lasted 3 hours. In the experiments where the temperature was varied, the furnace was initially increased to 500 °C during the first 10 minutes. Then the temperature was increased in steps of 50 °C, were each step was held for 20 minutes. This was done until a final temperature of 900 °C was reached. The temperature was held constant at 900 °C for 20 minutes before decreasing to room temperature. The total duration of each oxidation experiment was 3 hours per sample. The water vapour partial pressure in the reaction chamber was 600 Pa for all samples.

4.5 Two-stage oxidation: $^{18,18}O_2$-$^{16,16}O_2$ isotope exchange

Two-stage oxidation by exchange of oxygen isotopes $^{18,18}O_2$ and $^{16,16}O_2$ is often used to investigate the growth mechanisms of oxides on alloys. Characterization methods such as Secondary Ion Mass Spectrometry (SIMS) can subsequently be used to obtain depth profiles showing the distribution of oxygen isotopes in the scale, and by this provide information about the dominating growth mechanisms. It is then possible to elucidate to what extent outward cation diffusion, or inward diffusion of oxygen, is taking place in the scale growth.

4.5.1 Sample preparation and instrumentation

Foil of Sanergy HT (0.2 mm thick) was cut into samples of dimensions 20x10 mm^2, cleaned in ethanol and dried by pressurized air. The samples where placed inside a closed quartz tube, inserted into a tube furnace at isothermal temperature. The total pressure was monitored by a Pfeiffer CMR 261 pressure gauge, and the gas composition by a Pfeiffer Prisma QME 200 Quadropole Mass Spectrometer. The oxygen isotopes $^{18,18}O_2$ and $^{16,16}O_2$ were introduced by a connected gas supply system.

The samples were initially oxidized in $^{18,18}O_2$ up to approximately half the desired scale thickness. Subsequently the gas was exchanged to $^{16,16}O_2$. By using $^{16,16}O_2$ in the final stage of oxidation, any small air leakages in the system over time would not severely affect the experiment. All two-stage oxidation experiments of this work were conducted on cobalt coated samples.

4.6 Characterization methods

The samples in this work were characterized post oxidation by a number of methods to retrieve information about the crystal structure, composition and morphology of the oxide scales. X-ray diffraction, Scanning Electron Microscopy and Secondary Ion Mass Spectrometry can all provide different types of information. This section will present the characterization methods used to investigate the oxidized samples of this work.

4.6.1 X-ray diffraction

The oxide phases present in the scales grown on Sanergy HT were identified by X-ray diffraction (XRD). The instrument used was a Bruker D8 Discover diffractometer with monochromatic Cu-$K_{\alpha 1}$ radiation and Bragg-Brentano geometry. Fluorescence suppression settings were used to avoid noise from

Fe fluorescence due to the copper radiation source. The resulting diffraction patterns were compared to the ICDD [1] database in the program EVA (Bruker AXS Inc., USA).

4.6.2 Scanning Electron Microscopy

Analysis of chemical composition and morphology were conducted by Scanning Electron Microscopy (SEM). The instrument used was a Quanta 200F FEG-SEM (FEI Company, USA). This microscope has two different detectors for collecting secondary electrons. In high vacuum (HV), the microscope uses an Everhart-Thornley detector (ETD), while in low vacuum a Large-Field detector (LFD). Backscattered electrons are collected by a Solid-State detector (SSD). In addition, an Energy-Dispersive detector is used to map chemical composition. Oxide scale thicknesses were measured by the imaging program *XT docu*. To conduct cross sectional analysis of oxidized samples by SEM, the samples were embedded in resin and prepared by wet water grinding on SiC grinding paper. Surface imaging in SEM required no further sample preparation.

4.6.3 Secondary Ion Mass Spectrometry

The distributions of oxygen isotopes $^{18,18}O_2$ and $^{16,16}O_2$ in oxide scales grown during two-step oxidation experiments were investigated by Secondary Ion Mass Spectrometry (SIMS). SIMS is widely used in analysing tracer elements in solid materials. The sample is sputtered by a focused ion beam, and the ejected secondary ions are then collected and analysed. Depth profiles can be constructed by recording secondary ion intensities as a function of sputter time. Converting ion intensities to concentration values involve using a reference sample of known concentration. As no standard is available for the samples analysed in this work, the measured ion intensities, I_i, were converted to normalized, fractional concentrations according to equation 4.1.

$$C_{i_1}(x) = \frac{I_{i_1}(x)}{I_{i_1}(x) + I_{i_2}(x)} \tag{4.1}$$

C_i is the normalized ion concentration of the chemical species $_i$, x is inward depth from the oxide surface and I_i is the measured ion intensity of the chemical species i. The sputter time was converted to depth by measuring the depth of the sputtered crater with a profilometer. The instrument used was a Cameca IMS 7f with a 15 keV Cs^+ ion beam. The depths of the sputtered SIMS craters were measured by a Dekta 8 stylus profilometer. For depth calibration, the erosion rate was assumed to be constant. The SIMS analysis was conducted in collaboration with Lasse Vines at the Department of Physics, University of Oslo.

[1] International Centre for Diffraction data

4.7 Sources of error

Obtaining exact measurements by experimental work is impossible. Scientific results will always be susceptible to error, and the goal of any experimentalist should thus be to minimize these errors and keep track of their sources. This section will provide some known inaccuracies and sources of errors in the experimental methods used in this work.

4.7.1 Sample preparation

The alloy used in this work was provided by Sandvik Materials Technology. Compositional differences between alloy batches can occur, and it is thus preferable that all compared samples originate from the same batch. The initial oxidation of metal surfaces are very affected by defects present at the surface. To avoid grease and foreign impurities on the surfaces, gloves should be worn while handling the samples. Bending the samples introduce defects such as dislocations into the material, which may affect the oxidation mechanisms. It is also important to consider the sample dimensions, as thinner samples are reported to oxidize faster.[16]

4.7.2 Thermogravimetry

The oxidation of metals is very much affected by temperature. Also, the thermobalance is sensitive to thermal vibrations. To ensure comparable conditions and minimal noise, temperature stability is important. The samples were suspended midway down and in the center of the cylindrical furnace, this to minimize the effect of any gradient in temperature. The thermocouple monitoring the temperature was mounted at the same height as the samples. The thermobalance is also sensitive to mechanical vibrations, which can be reduced by placing the instrument on vibration absorbing material.

The gas flow from the gas mixer will also contribute to noise. This noise will vary depending on the weight and size of the present gas molecules. Due to this noise, only the overall trends and oxidation kinetics were considered when analysing the thermogravimetric data.

The flow meters of the gas mixer have high uncertainties ($\sim$ 60 %) at flows below 20 mm. The uncertainty is reduced to $\sim$ 5 % for flow rates above 60 mm. The flow rates in the experimental work of this thesis were thus constrained to higher levels, with an absolute minimum value of 30 mm. The gas mixer consists of copper tubing and numerous connections, which are prone to leakages from the ambient. The entire gas mixer and

the thermobalance were checked for leakages at regular intervals to ensure a gas-tight system.

Uncertainties of rate constants from thermogravimetric measurements

Growth rate constants are widely used in describing kinetics of oxidation reactions on metal or alloy surfaces. In this work, parabolic oxidation behaviour is the most encountered and this section will thus discuss uncertainties of parabolic growth rate constants. Uncertainties include:

- temperature uncertainty of the thermocouple
- temperature gradient inside furnace
- variance in the surrounding atmosphere
- mechanical disturbance and noise
- sample manufacturing and surface preparation
- surface area measurements and calculations
- fitting and analysis of experimental data

Oxidation kinetics are very dependent on temperature. It is therefore of high importance to be in control of the temperature in which the oxidation experiments proceed. As mentioned in section 4.2.1, the temperature inside the furnace is monitored by a thermocouple. There will be a difference between the temperature measured and the true temperature the samples are exposed to. The magnitude of this temperature difference should be examined to verify how this may influence the measurements.

The parabolic weight related growth rate constant $k_{p,w}$ is calculated from thermogravimetric experiments by plotting the weight gain of a sample squared as a function of time. If the growth is parabolic, this will yield a straight line with a slope $k_{p,w}$. The most common unit used for reporting $k_{p,w}$ values is $\frac{g^2}{cm^4 s}$. The calculated $k_{p,w}$ values may vary as a function of experimental duration. When comparing $k_{p,w}$ values of several experiments, it is preferable that all growth rate constants are calculated from a similar number of hours. Mechanical disturbance will also give rise to noise in the measurement data, affecting the linear fit and hence the value of k_p.

Chapter 5

Results

This chapter will present the results from the oxidation experiments conducted on uncoated and cobalt coated samples of Sanergy HT. The chapter is divided in four main parts:

- Composition and morphology
- Thermogravimetry
- Two-stage oxidation ($^{18,18}O_2$ -$^{16,16}O_2$ exchange)
- HT-ESEM

The first section will present the composition and morphology of the formed oxide scales, including results from XRD and SEM. The next sextion presents measured weight gain curves, temperature dependencies and p_{O_2} dependencies of parabolic rate constants for precoated and uncoated samples of Sanergy HT. The third section, presenting the results from the two-stage oxidation experiments, will include characterization of the resulting oxide scales by SIMS. The HT-ESEM section will include series of images from SEM, showing oxide scale development as a function of time. A CD including video clips of the oxide scale growth observed during HT-ESEM will be included as an attachment to this thesis.

5.1 Composition and morphology of oxide scales

5.1.1 Chemical composition

The compositions of the oxide scales formed on uncoated and coated samples were characterized by XRD and EDS. EDS analysis of the oxide scales formed on samples of Sandvik Sanergy HT indicates a duplex oxide scale consisting of a Cr_2O_3 phase near the alloy-oxide interface and a $(A,B)_3O_4$ (A, B = Mn, Cr, Co and/or Fe) spinel phase near the gas-oxide interface. This was confirmed by XRD. The oxide phases identified by XRD for uncoated

samples in wet air is presented in table 5.1. The exact chemical composition of the spinel phase is difficult to determine, due to the small difference in ionic radii for Fe, Mn and Cr cations. The most probable composition is a manganese rich spinel phase, as indicated by EDS. The spinel phase varies in composition depending on temperature, time and surface coating. For cobalt coated samples, the spinel phase was found to be rich in cobalt and deficient in chromium.

Table 5.1: Oxide phases identified by XRD in oxide scale on uncoated Sanergy HT samples, oxidized in wet air at 850 °C and 900 °C for 150 hours.

Oxide phases
Cr_2O_3
$FeMn_2O_4$
$MnFe_2O_4$
$CrMn_{1,5}O_4$
$Cr_{1,3}Fe_{0,7}O_3$
Fe_2O_3

The total thickness of the oxide scale, and the ratio between the spinel phase and chromia, varies as a function of time, temperature and reaction atmosphere. A linescan showing the distribution of O, Cr, Mn, Co and Fe as a function of distance through the oxide scale of a cobalt coated sample oxidized in wet 5 % H_2+Ar at 975 °C for 40 hours, can be seen in figure 5.1. The outer layer of the oxide scale is the (Co, Mn)$_3O_4$ spinel phase and the inner layer is Cr_2O_3.

Surface concentrations of cations: Cr, Mn and Fe

The surface concentrations of Cr, Mn and Fe for uncoated and cobalt coated samples oxidized in wet 5 % H_2+Ar and O_2+Ar mixtures at temperatures from 850 °C to 1000 °C for 150 hours were estimated by EDS-analysis, see table 5.2.

Chromium concentrations on surfaces of uncoated samples are similar under reducing and oxidizing conditions, indicating negligible dependence on p_{O_2}. The variation with increasing temperature is also small. Cobalt coated samples show low concentrations of chromium at temperatures below 925 °C. At temperatures from 925 °C to 1000 °C, large precipitations of chromium rich particle clusters are observed, see figure 5.2. The Cr concentrations in these islands are significantly higher, from 38 at.% to 47 at.%.

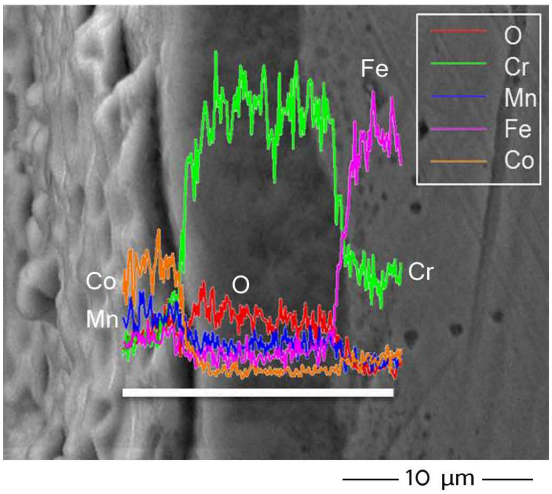

Figure 5.1: Angled view of spinel and chromia oxide scales formed on Co coated sample oxidized in wet 5 % H_2+Ar at 975 °C for 40 hours. EDS linescan results are included to show the distribution of selected elements as a function of distance.

Table 5.2: Surface concentrations of Cr, Mn and Fe under oxidizing and reducing conditions at temperatures from 850 °C to 1000 °C after 150 hours.

Atmosphere	**Sample**	**Cr (at.%)**	**Mn (at.%)**	**Fe (at.%)**
wet 5 % H_2+Ar	Uncoated	40-50	20-23	2-5
wet 5 % H_2+Ar	600 nm Co	3-9	4-16	6-7
O_2+Ar	Uncoated	43-45	11-20	2-5
O_2+Ar	600 nm Co	3-9	10-20	2-5

The concentration of manganese measured on oxide surfaces increases as a function of temperature and time. This is assumed to be a result of larger amounts of manganese reaching the surface after diffusion from the alloy interior. For uncoated samples at 900 °C, large crystalline particles rich in Mn were observed, see figure 5.3. These crystalline particles had a Mn concentration of 65 at.%. The Mn rich particles had very low concentrations of chromium, 3 at.%, which indicates the formation of a relatively pure manganese oxide phase.

Surface concentrations of Fe on uncoated and cobalt coated samples are generally low and constant. However, cobalt coated samples under reducing conditions show slightly increased surface concentrations of iron, as seen in table 5.2.

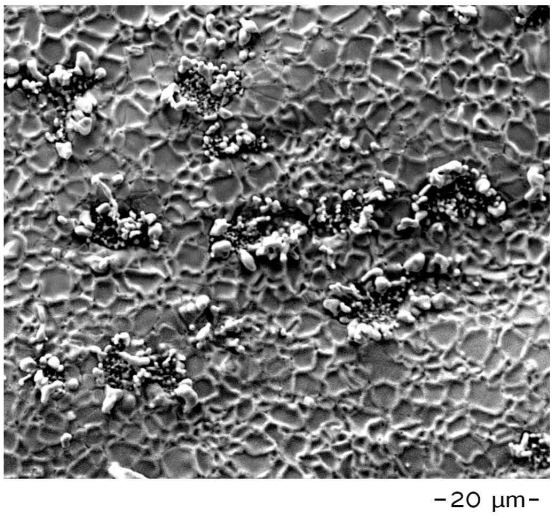

Figure 5.2: Surface of cobalt coated sample oxidized in wet 5 % H_2+Ar for 150 hours at 950 °C. Large precipitations of Cr rich particle clusters and protruding oxide ridges are observed.

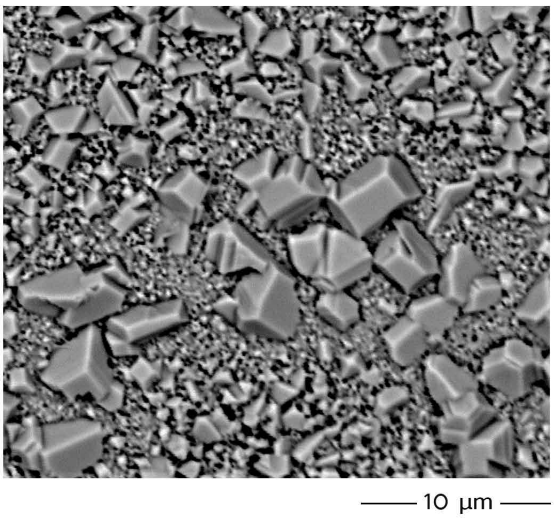

Figure 5.3: Surface image of the formed oxide scale on a uncoated sample oxidized in wet 5 % H_2+Ar at 900 °C for 150 hours. Large, Mn rich (65 at.%) crystalline particles were observed.

Table 5.3: Concentrations of Cr, Mn, Fe and Co in chromia and spinel phases on uncoated and cobalt coated samples oxidized in wet 5 % H_2+Ar at temperatures from 850 °C to 1000 °C after 150 hours. In the spinel phase $(A,B)_3O_4$, A and B represent Cr, Mn, Co and Fe.

Cr_2O_3	**Cr (at.%)**	**Mn (at.%)**	**Fe (at.%)**	**Co (at.%)**
Uncoated	60	< 1	6-8	-
600 nm Co	60	< 1	6	< 1
$(A,B)_3O_4$	**Cr (at.%)**	**Mn (at.%)**	**Fe (at.%)**	**Co (at.%)**
Uncoated	45	40	12	-
600 nm Co	5-8	14	12-16	30-46

Cation concentrations in oxide scale cross sections

Uncoated samples and cobalt coated samples oxidized in wet 5 % H_2+Ar a temperatures between 900 °C and 1000 °C show duplex oxide scales consisting of Cr_2O_3 near the oxide-alloy interface and (Cr, Mn)$_3O_4$ spinel near the gas-oxide interface. The concentrations of Cr, Mn, Fe and Co in chromia and spinel phases on uncoated and cobalt coated samples oxidized under reducing conditions at temperatures from 850 °C to 1000 °C for 150 hours can be seen in table 5.3.

Some interesting features are:

- A selection of cobalt coated samples indicate Fe concentrations of 12-16 at.% in the (Co, Mn)$_3O_4$ spinel phase. The observed Fe concentrations drop in the Cr_2O_3 layer, and is thus not caused by collected signals from the underlying steel.

- EDS linescans indicate increased concentrations of Si (2-4 at.%), Ti (1 at.%) and Nb (1-2.7 at.%) in the spinel-Cr_2O_3 and Cr_2O_3-alloy interfaces. These elements are present in the alloy in small concentrations[1].

5.1.2 Surface morphology

The surface morphologies of grown oxide scales were investigated by SEM imaging. Large variations were observed, confirming the complex relation between nucleation and growth of oxide particles, and external influences such as surface treatment, temperature and gas compositions.

[1]Nominal composition of Sanergy HT can be found in table 4.1 in chapter 4

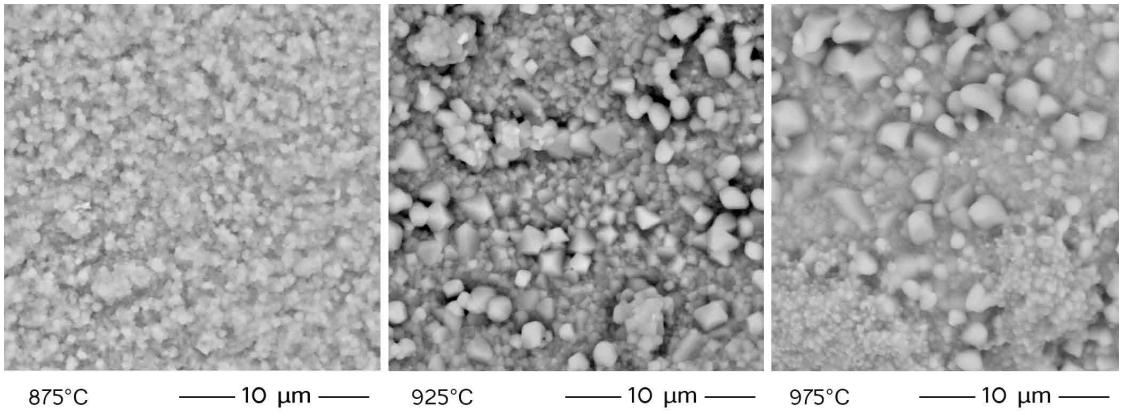

(a) 45 hours at temperatures from 875 °C to 950 °C.

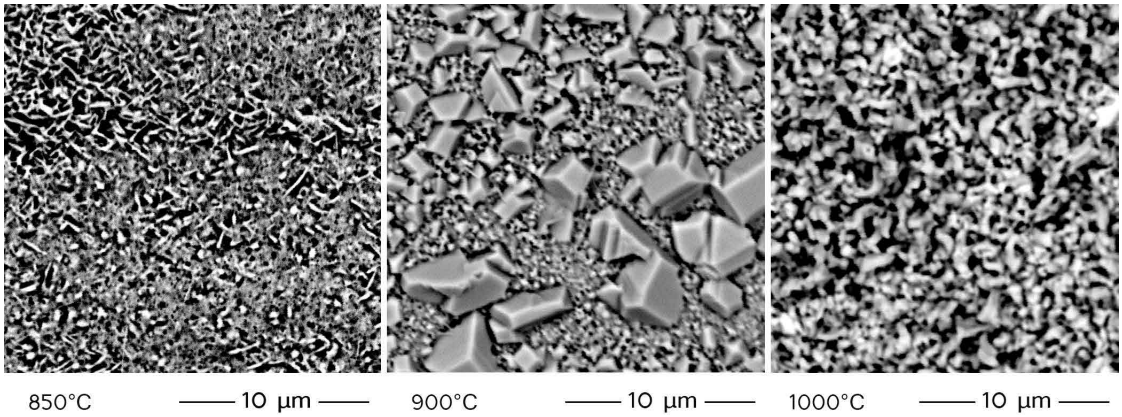

(b) 150 hours at temperatures from 850 °C to 1000 °C.

Figure 5.4: Surfaces of uncoated samples oxidized in wet 5 % H_2+Ar for 45-150 hours at temperatures from 850 °C to 1000 °C.

Uncoated samples oxidized in wet air and wet 5 % H_2+Ar for 150 hours at temperatures from 850 °C to 1000 °C generally show uniform, continuous scales. Figure 5.4 show uncoated samples oxidized under reducing conditions for 45-150 hours at temperatures from 850 °C to 1000 °C. In wet air larger, spherical particles are nucleated in the rolling direction of the steel foil. This is not observed under reducing conditions.

The microstructure of uncoated steel samples prior to and after oxidation in wet air at 900 °C for 150 hours can be seen in figure 5.5. The oxide scales generally consist of homogeneous crystalline particles, with the exception of larger nucleations on surface defects. With increasing temperature, uncoated samples show larger particle sizes and wider size distributions, see table 5.4.

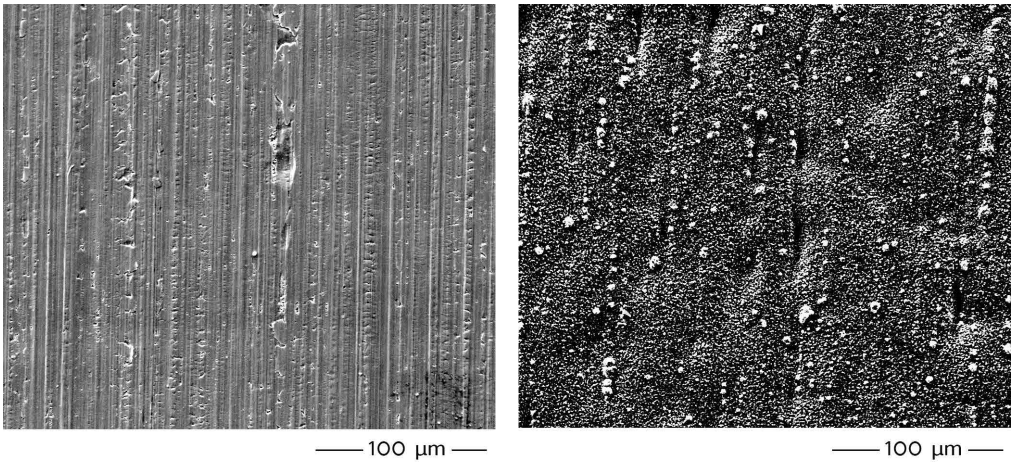

Figure 5.5: Left: Surface of uncoated steel sample prior to oxidation. Right: Uncoated sample oxidized at 900 °C in wet air for 150 hours. Larger particles grow in the rolling direction of the steel foil.

Table 5.4: Particle sizes of oxide scales on uncoated samples oxidized in wet air at temperatures from 850 °C to 1000 °C for 150 hours.

Temperature (°C)	Particle size (μm)
850	0.4
900	0.7
1000	1-5

At lower temperatures, the oxide scales are relatively flat. However, the scales become more buckled with increasing temperature, indicating larger growth stresses in the oxide scales at higher temperatures. Under reducing conditions, the scales at high temperatures are less buckled than under oxidizing conditions. A comparison of the oxide scale surfaces of uncoated samples oxidized at 900 °C for 150 hours under oxidizing and reducing conditions can be seen in figure 5.6.

Uncoated samples oxidized under reducing conditions at 850 °C exhibit surfaces covered by whiskers of varying length and thickness, as seen in figure 5.4b.

For cobalt coated samples oxidized under both oxidizing and reducing conditions, two temperature regions are observed. At temperatures from 850 °C to 900 °C, the oxide scale is uniform and continuous with no second

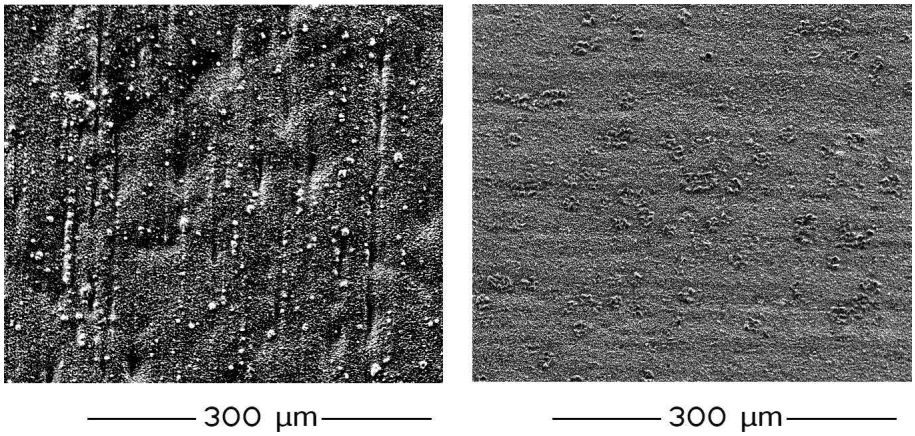

Figure 5.6: Surfaces of uncoated samples oxidized in wet air (left) and wet 5 % H_2+Ar (right). The oxide scale formed under reducing conditions is less buckled.

phase precipitates. At 850 °C, the oxide particles are clearly defined and crystalline. As temperature increases, the grains sinter to soft-edged particles with wide distributions in shape and size.

The second temperature region begins at approximately 925 °C, where the oxide grains sinter further to large, flat grains from 1 μm to 8 μm in diameter. Gaps and pores are present at the grain boundaries, and the grain boundaries appear as ridges on otherwise flat oxide scales. The ridges at the grain boundaries are most protruding at temperatures between 925 °C and 975 °C. At 1000 °C, the grain boundaries appear more flat. For all samples oxidised at temperatures from 925 °C to 1000 °C, large precipitations of spherical particles are observed. These are identified as Cr_2O_3. Figure 5.7 show the surfaces of cobalt coated samples oxidized in wet 5 % H_2+Ar for 150 hours at temperatures from 850 °C to 1000 °C.

5.1.3 Metal-oxide interface properties

Stress induced ballooning of the oxide-alloy interface was observed for uncoated samples oxidized in wet air at 1000 °C for 150 hours. This effect was not observed for samples oxidized under reducing conditions at the same temperature. Samples oxidized under reducing conditions exhibited flat oxide-alloy interfaces, indicating uniform growth without significant growth stresses. A comparison of the oxide-alloy interfaces under oxidizing and reducing conditions can be found in figure 5.8. White precipitations, see figure 5.9 were observed at the oxide-alloy interface after oxidation in wet 5 % H_2+Ar and wet air at temperatures from 900 °C to 1000 °C. A selection

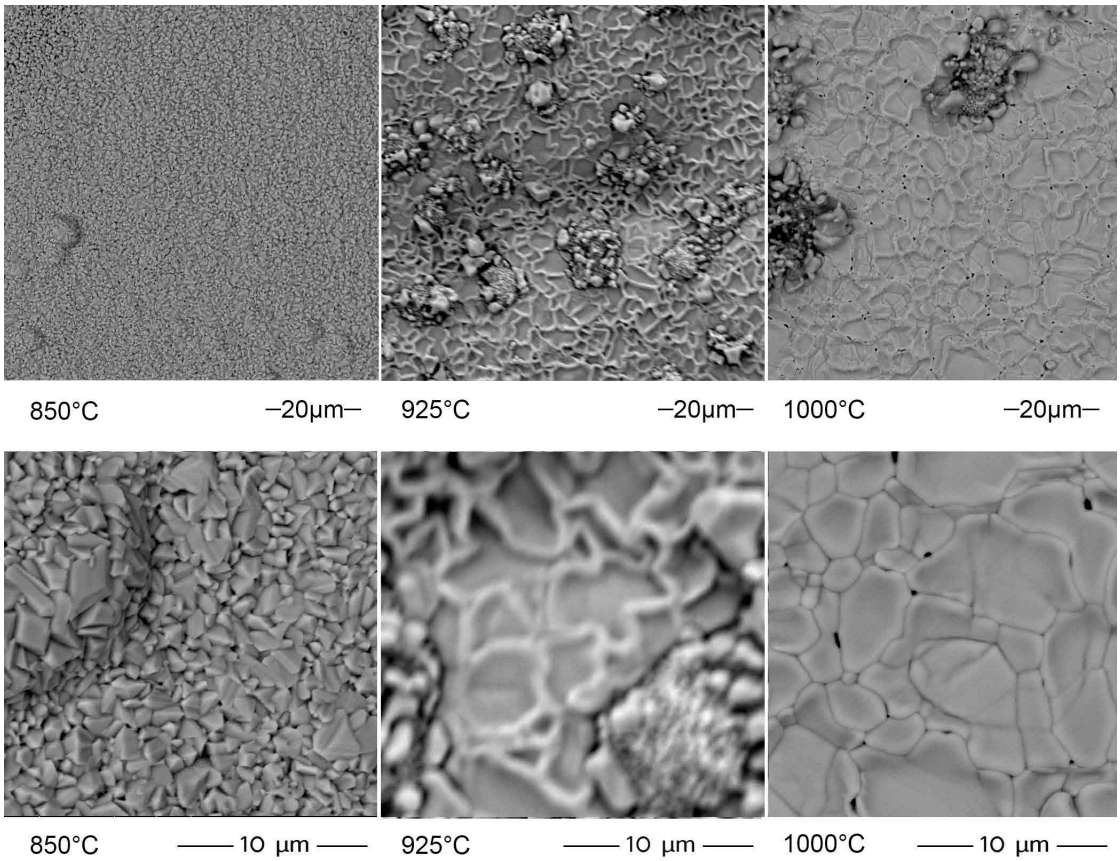

Figure 5.7: Cobalt coated samples oxidized in wet 5 % H_2+Ar for 150 hours at temperatures from 850 ° to 1000 °C

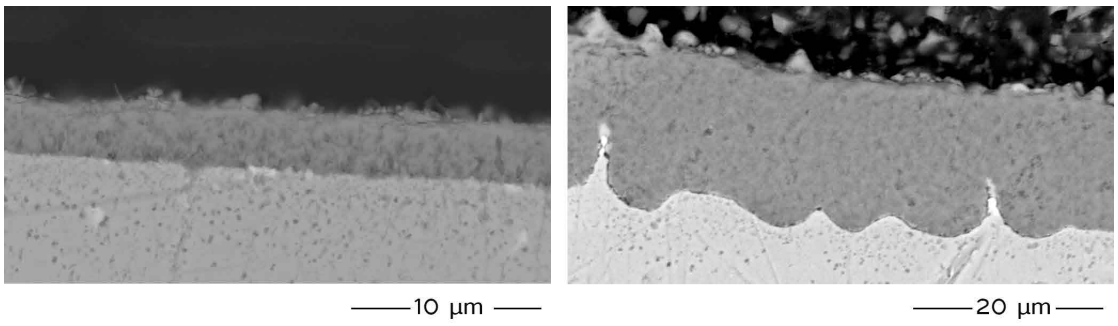

Figure 5.8: Flat oxide-alloy interface for uncoated sample oxidized in wet 5 % H_2+Ar, ballooning of oxide-alloy interface for sample oxidized in wet air. Both samples are uncoated and oxidized at 1000 °C for 150 hours.

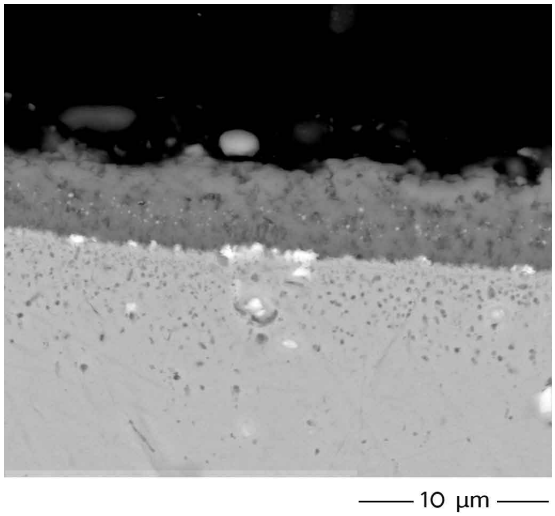

Figure 5.9: White precipitations inside oxide scale and at oxide-alloy interface. 600 nm Co coated sample oxidized in wet 5 % H_2+Ar at 900 °C for 150 hours.

of samples showed increased concentrations of Si, Ti, Mo and Nb in the oxide-alloy interfaces. Due to the small amounts, determination of phase compositions from is difficult. The same samples also exhibited gaps at the oxide-alloy interfaces. EDS linescans showed increased concentrations of Ti, Si in oxide-alloy interfaces.Increased concentration of Si in the spinel-chromia interface and possibly inside the spinel layer, was also observed.

5.2 Thermogravimetry

Thermogravimetric measurements were conducted to measure the weight gain due to oxide growth of cobalt coated and uncoated Sanergy HT as a function of time. In this section the results of these experiments will be presented. The parabolic growth rate constants are all calculated from the first 45 hours of oxidation, unless stated otherwise. Tables of weight related parabolic growth rate constants for thermogravimetric measurements conducted in this work can be found in the Appendix.

5.2.1 Temperature dependency

Figure 5.10 shows the weight gain of 600 nm Co coated Sandvik Sanergy HT samples at temperatures from 850 °C to 1000 °C in wet 5 % H_2+Ar under atmospheric pressure. All samples show parabolic weight gain as a function of time, indicating diffusion-controlled oxide scale growth. The weight gain curve at 1000 °C show a rapid increase in reaction rate after approximately 90 hours.

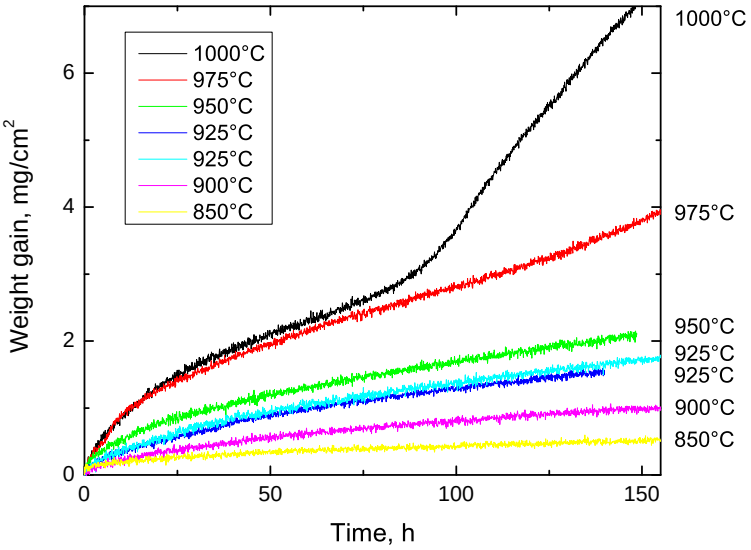

Figure 5.10: Weight gain of 600 nm Co coated Sandvik Sanergy HT at temperatures from 850 °C to 1000 °C in wet 5 % H_2+Ar under atmospheric pressure.

The weight gain curves of uncoated samples at temperatures from 850 °C to 1000 °C in wet 5 % H_2+Ar and in wet air, both under atmospheric pressure, are given in figure 5.11 and figure 5.12. Under reducing conditions,

the oxidation kinetics for uncoated samples are parabolic at all measured temperatures. The weight gain curves in wet air are all initially parabolic, but at 1000 °C the oxidation rate accelerates after approximately 80 hours. This acceleration in reaction rate, often termed "breakaway oxidation", leads to a change from parabolic to essentially linear growth kinetics.

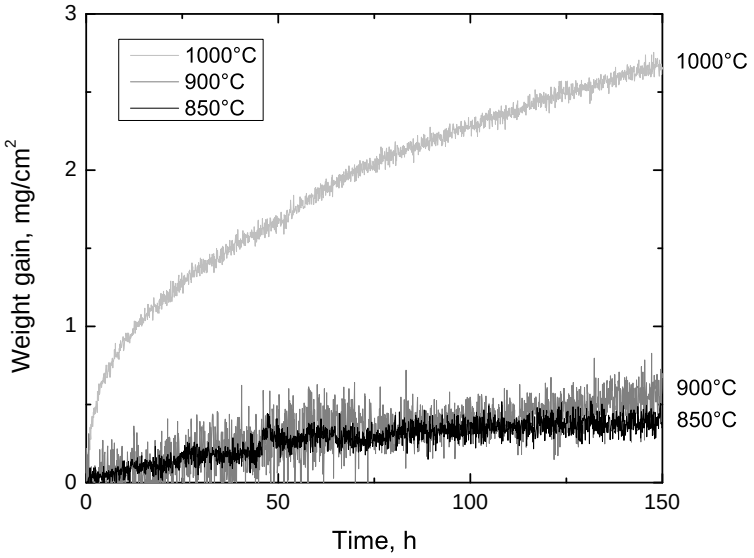

Figure 5.11: Weight gain as a function of time for uncoated Sanergy HT oxidized in wet 5 % H_2+Ar at 1000 °C, 900 °C and 850 °C for 150 hours.

The oxidation behaviour of uncoated samples oxidized in wet air and wet 5 % H_2+Ar at 1000 °C for 150 hours can be seen in figure 5.13. In wet air, breakaway oxidation is observed, while in wet 5 % H_2+Ar the oxidation follows parabolic behaviour.

A comparison of the weight gain curves for cobalt coated and uncoated Sanergy HT oxidized in wet 5 % H_2+Ar at 1000 °C for 150 hours can be seen in figure 5.14. At 1000 °C, the oxidation of the uncoated sample follows parabolic rate kinetics while the cobalt coated exhibits an acceleration in oxidation rate after approximately 80 hours.

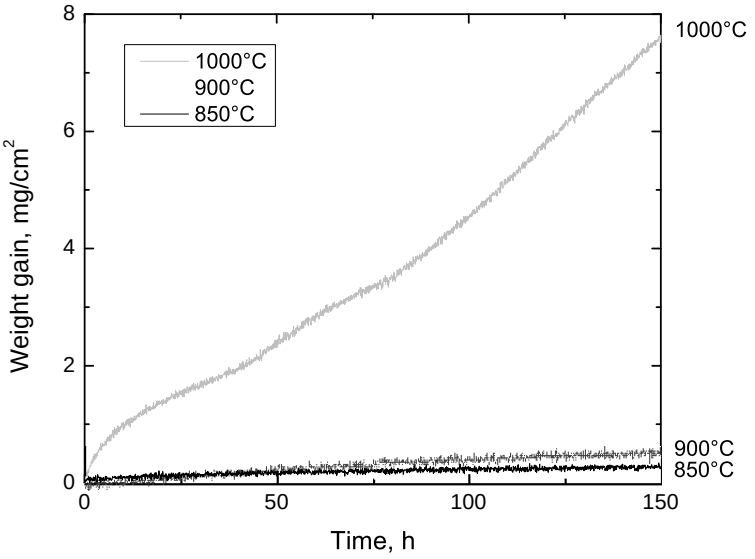

Figure 5.12: Weight gain as a function of time for uncoated Sanergy HT oxidized in wet air at 1000 °C, 900 °C and 850 °C for 150 hours.

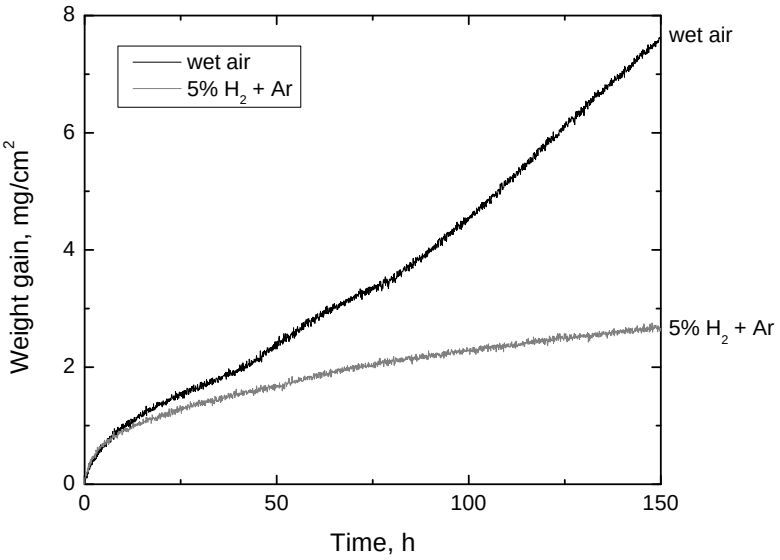

Figure 5.13: Comparison of the weight gain for the oxidation of uncoated Sanergy HT at 1000 °C in wet air and wet 5 % H_2+Ar for 150 hours.

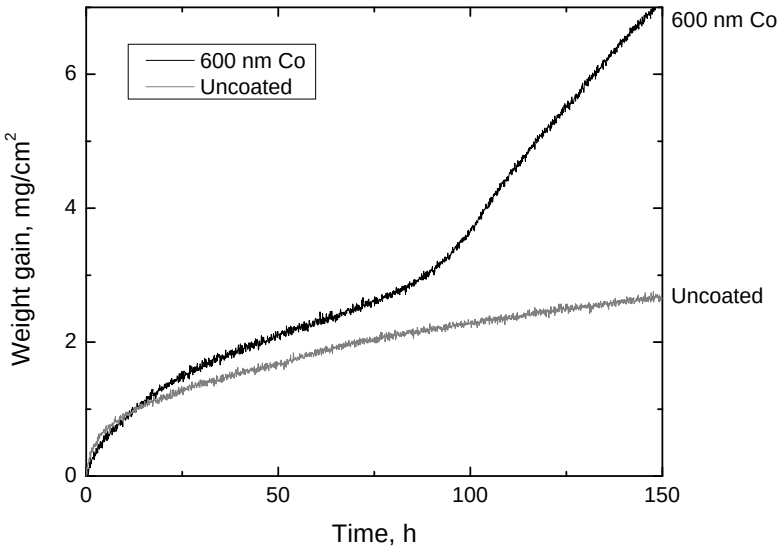

Figure 5.14: Comparison of the weight gain for the oxidation of cobalt coated and uncoated Sanergy HT at 1000 °C in wet 5 % H_2+Ar for 150 hours.

5.2.2 Activation energy

The activation energy for oxidation was calculated from the slope of a linear fitting of weight related parabolic rate constants presented in an Arrhenius plot. All rate constants were calculated from the initial 45 hours of oxidation in both wet 5 % H_2+Ar and wet air under isothermal conditions from 800 °C to 1000 °C.

Cobalt coated Sanergy HT follows approximately linear Arrhenius behaviour in wet 5 % H_2+Ar at temperatures from 850 ° to 1000 °C, see figure 5.15, and the activation energy was calculated to 323 kJ/mol. In wet air, the activation energy was calculated to 317 kJ/mol. The activation energies for Co coated samples under oxidizing and reducing conditions differ by 6 kJ/mol, which is well within the expected uncertainty. The activation energy for oxidized Co coated samples is thus assumed to be equal under oxidizing and reducing conditions.

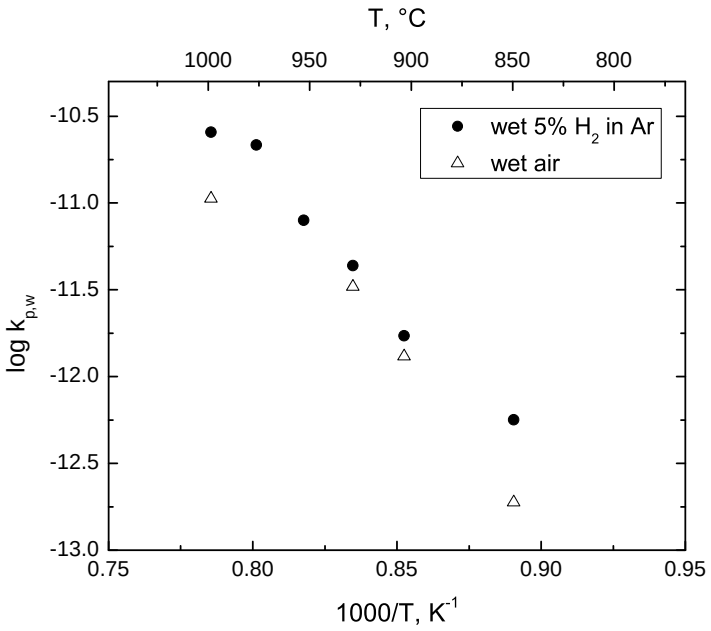

Figure 5.15: Arrhenius plot of $k_{p,w}$, weight related parabolic rate constants measured by thermogravimetry, for the oxidation of 600 nm Co coated in wet 5 % H_2+Ar and wet air from 850 °C to 1000 °C.

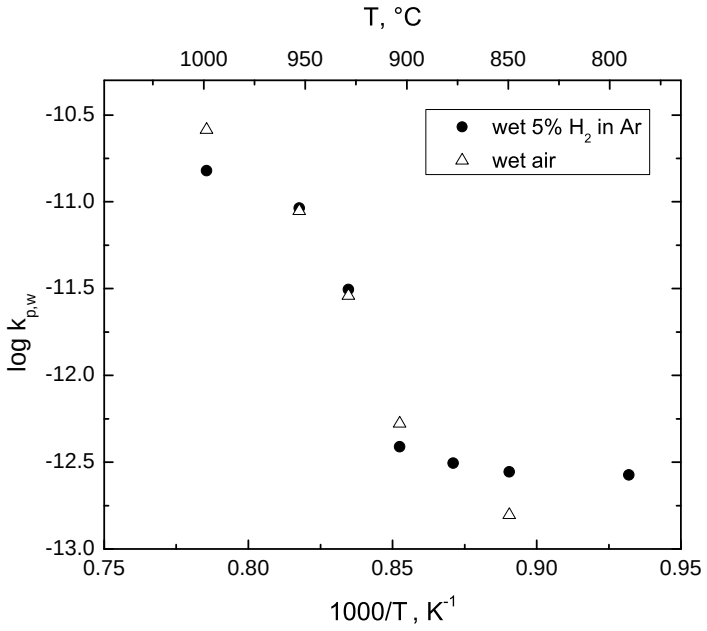

Figure 5.16: Arrhenius plot of $k_{p,w}$, weight related parabolic rate constants measured by thermogravimetry, for the oxidation of uncoated Sanergy HT in wet 5 % H_2+Ar and wet air from 850 °C to 1000 °C.

Uncoated samples in wet 5 % H_2+Ar, see figure 5.16, do not follow linear Arrhenius behaviour and the activation energy can thus not be calculated from the full temperature range. The temperature dependence in wet air follow a more linear Arrhenius-type behaviour and the activation energy was calculated to 431 kJ/mol. A summary of the calculated activation energies of both cobalt coated and uncoated samples can be found in table 5.5.

Table 5.5: Activation energies, E_a calculated for the oxidation of 600 nm Co coated and uncoated samples in wet 5 % H_2+Ar and wet air.

Sample	Atmosphere	E_a (kJ/mol)
600 nm Co	wet 5 % H_2+Ar	323
	wet air	317
Uncoated	wet 5 % H_2+Ar	non-linear Arrhenius behaviour
	wet air	431

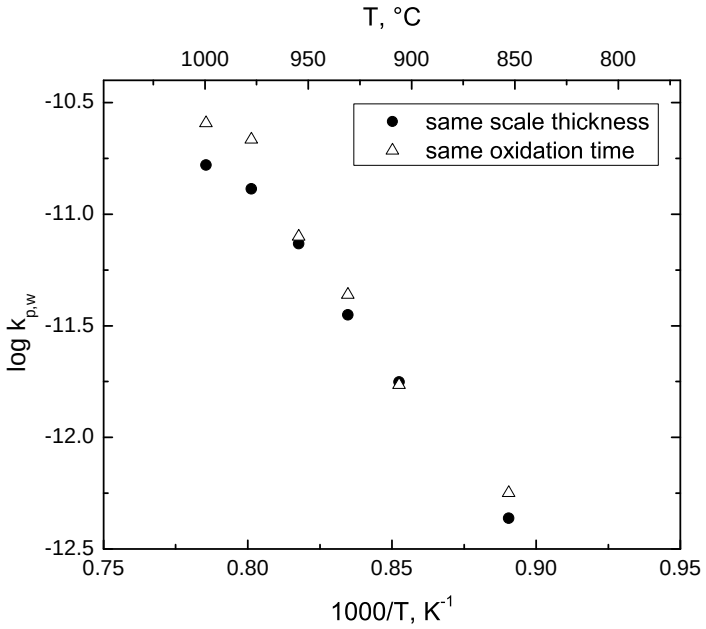

Figure 5.17: Arrhenius plot of $k_{p,w}$, weight related parabolic rate constants for the oxidation of cobalt coated samples oxidized in wet 5 % H_2+Ar. Each rate constant is calculated from the time each sample is expected to have the same oxide scale thickness. The assumed thickness used for calculations was 3.4 μm.

The non-linear temperature dependence for uncoated samples under reducing conditions could result from the parabolic rate constants, each calculated from the initial 45 hours of oxidation, representing different stages of the oxide growth. To investigate the effect of scale thickness on the dependence of temperature, parabolic growth rate constants calculated after 45 hours are compared to rate constants calculated from the time were the samples are expected to have similar oxide scale thickness. Figures 5.17 and 5.18 show cobalt coated and uncoated samples, respectively.

5.2.3 Correlation between expected oxide scale thickness from $k_{p,t}$ and scale thickness measured by SEM

An expected oxide scale thickness after 150 hours at a specific temperature was calculated by converting weight related parabolic growth rate constants ($k_{p,w}$) measured by TG to thickness related rate constants ($k_{p,t}$) using equation 2.20 on page 17. A comparison of the calculated oxide scale thickness and the scale thickness measured by SEM for uncoated and cobalt coated samples oxidized in wet 5 % H_2+Ar for 150 hours at temperatures from 850 °C to 1000 °C can be seen in table 5.6.

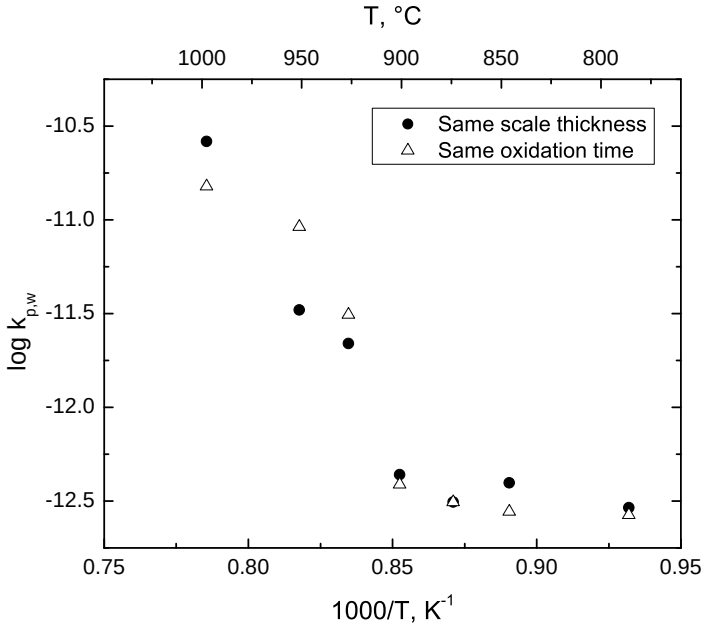

Figure 5.18: Arrhenius plot of $k_{p,w}$, weight related parabolic rate constants for the oxidation of cobalt coated and uncoated samples oxidized in wet 5 % H_2+Ar. Each rate constant is calculated from the time where each sample is expected to have the same oxide scale thickness. The assumed thickness used for calculations was $1{,}4\mu m$.

Table 5.6: Comparison of oxide scale thickness calculated from thickness related parabolic growth rate constants (A) and scale thickness measured by SEM (B) for uncoated and cobalt coated samples oxidized in wet 5 % H_2+Ar at temperatures from 850 °C to 1000 °C for 150 hours.

T, °C	**A: calculated,** μm	**B: measured,** μm	**Ratio: A/B**
Uncoated			
850	2.3	1.2	1.9
900	2.8	3.0	0.9
1000	17	9.0	1.9
600 nm Co			
850	3.3	2.0	1.6
900	5.9	4.5	1.3
925	9.0	9.0	1.0
950	13	8.0	1.6
975	22	10	2.2
1000	23	17	1.4

The oxide scale thickness measured by SEM was similar to or lower than the calculated scale thickness for both uncoated and cobalt coated samples at all temperatures. The reduced scale thickness could be due to sample preparation. Cross sections are prepared by embedding the sample in resin, and the hardening of the resin could cause parts of the oxide scale to detach. If the cross sections are slightly tilted during preparation, this would affect the scale thickness measured by SEM. However, as a tilted cross section would increase the observed oxide scale thickness by SEM, this source of error can be excluded. The reduced scale thickness can also be a result of evaporation of volatile species from the oxide scales. The volatilization of chromium is strongly dependent on p_{O_2},[20] and should not contribute to significant evaporation under reducing conditions.

5.2.4 p_{O_2} dependence of parabolic growth rate constants

Undoped chromia is reported to have pO_2 dependent defect concentrations, which will affect transport through the oxide and hence the oxide growth rate.

The p_{O_2} dependence of parabolic rate constants measured isothermally at 900 °C for uncoated and coated samples of Sanergy HT can be seen in figure 5.19. The growth rate constants show no significant dependence of p_{O_2}, and it is assumed that any small changes are caused by experimental uncertainties.

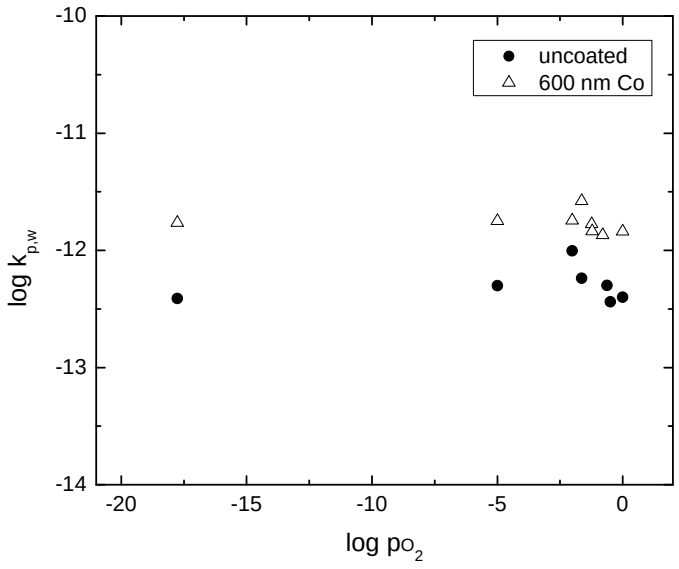

Figure 5.19: The p_{O_2} dependence of parabolic growth rate constants ($k_{p,w}$) measured isothermally at 900 ° by TG for uncoated and coated samples of Sanergy HT .

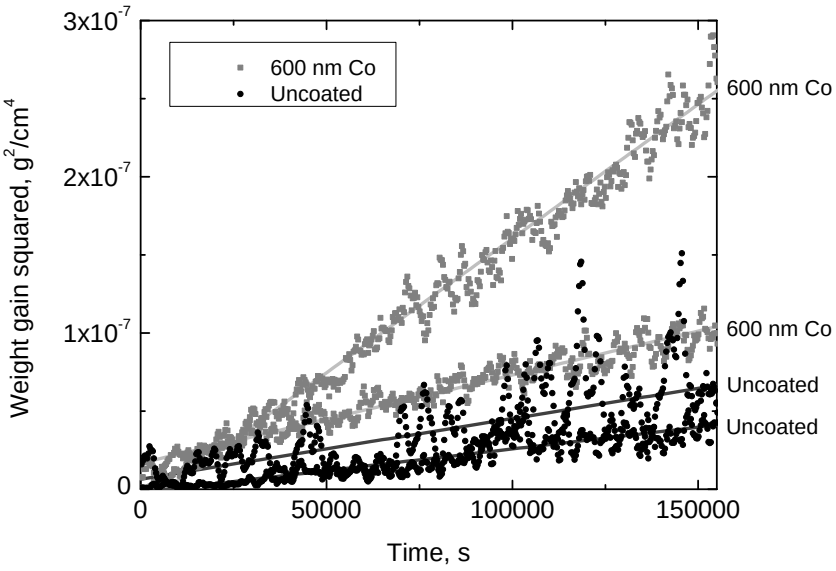

Figure 5.20: Weight gain squared (g^2/cm^4) as a function of time for cobalt coated and uncoated samples oxidized in wet 5 % H_2+Ar at 850 °C and 900 °C. Curves have been smoothed to reduce noise.

5.2.5 Effect of cobalt coating

The effect of cobalt coating on oxidation kinetics and growth rates were investigated. A comparison of the weight gain curves of cobalt coated and uncoated samples oxidized in wet 5 % H_2+Ar at temperatures from 850 °C to 900 °C, and at 1000 °C can be seen in figures 5.20 and 5.21 respectively. The weight gain of 600 nm Co coated samples is higher than that of uncoated samples in wet 5 % H_2+Ar for all measured temperatures. The parabolic growth rate constants for cobalt coated and uncoated samples in wet 5 % H_2+Ar and wet air at temperatures from 850 °C to 1000 °C can be seen in table 5.7.

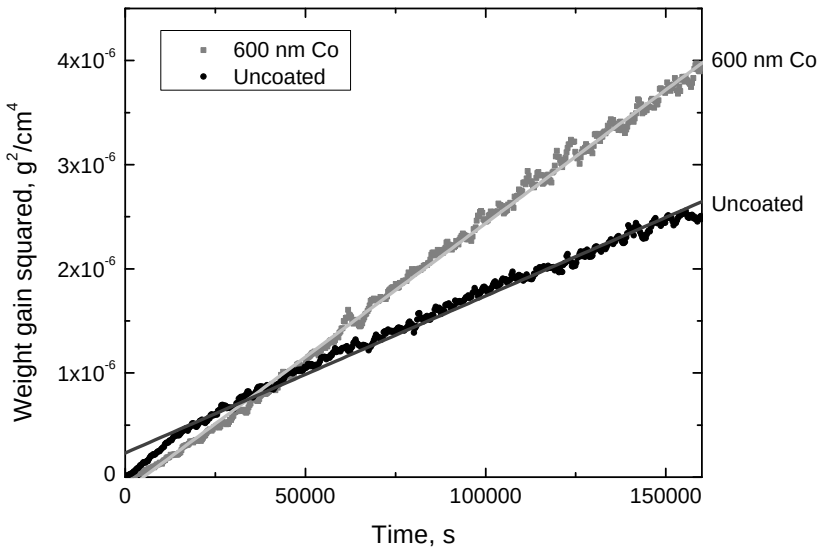

Figure 5.21: Weight gain squared (g^2/cm^4) as a function of time for cobalt coated and uncoated samples oxidized in wet 5 % H_2+Ar at 1000 °C. Curves have been smoothed to reduce noise.

Table 5.7: Parabolic growth rate constants, $k_{p,w}$ ($\cdot 10^{-13} g^2 cm^{-4} s^{-1}$), of cobalt coated (A) and uncoated (B) samples oxidized in wet 5 % H_2+Ar and wet air.

Temperature, °C	**A: 600 nm Co**	**B: Uncoated**	**Ratio: A/B**
wet 5 % H_2+Ar			
850 °C	5.6	2.8	2.0
900 °C	17	3.9	4.4
1000 °C	260	150	1.7
wet air			
850 °C	1.9	1.6	1.2
900 °C	13	5.3	2.4
1000 °C	106	260	0.4

5.2.6 Uncertainty of measured weight gain curves

To estimate the uncertainty of weight gain curves obtained by thermogravimetry, 3 samples oxidized under identical conditions were compared. The weight gain curves are given in figure 5.22 and the parabolic growth rate constants, calculated from the initial 45 hours of oxidation, are given in table 5.8. The estimated standard deviation of the series was $4.0{\cdot}10^{-13}$ $g^2/cm^4\ s^{-1}$, or approximately 29 % of the measured average value.

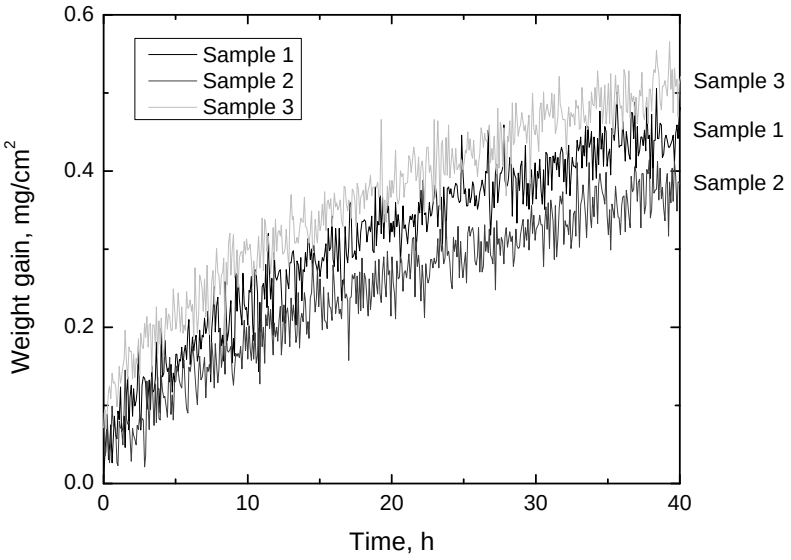

Figure 5.22: Uncertainty in weight gain curves for 3 samples oxidized under identical conditions.

Table 5.8: Comparison $k_{p,w}$ for 3 samples oxidized under identical conditions.

Sample	$k_{p,w}$, $g^2/cm^4\ s^{-1}$
1	$1.4{\cdot}10^{-12}$
2	$1.0{\cdot}10^{-12}$
3	$1.8{\cdot}10^{-12}$

When comparing different rate constants calculated from thermogravimetric data, rate constants should be corrected to a similar number of hours, or the same oxide scale thickness, if different measurements are to be compared. These to ensure that the rate constants represent the same stage in

the oxide growth, and to avoid the effect of noise or experimental artifacts on calculated $k_{p,w}$ values over time.

5.3 Two-stage oxidation

Two-stage oxidation experiments were conducted at temperatures from 850 °C to 1000 °C to investigate the distribution of oxygen isotopes and cations in the formed scales of cobalt coated samples. Normalized SIMS depth profiles were constructed, showing the measured concentrations as a function of depth in the oxide scales. When converting ion intensities measured by SIMS to fractional concentration distributions, the following assumptions were made:

- The secondary ion intensities of ^{16}O and ^{18}O are similar and thus comparable.
- Cobalt and chromium are assumed to occupy the same crystallographic sites in the oxide structure, and thus have dependent concentration distributions.
- The differences in secondary ion intensities of Co and Cr are assumed to be small enough to compare general behaviour and trends in cation distributions across the formed oxide scales.

Mn and Fe are also assumed to occupy the same crystallographic sites as Co and Cr, but very low secondary ion intensities increase the uncertainty of the measured intensities significantly. The secondary ion intensities for Mn in these measurements were too low to detect the distribution of manganese in the formed oxide scales. However, the distribution of Mn is of great interest and should be investigated further. To accurately detect the secondary ion intensities of ^{18}O and ^{16}O, the ion sputtering in this work was conducted by a Cs ion beam. However, as positive ionization can be enhanced by electronegative ions, sputtering with oxygen could possibly give better results for Mn and similar elements.

The normalized SIMS depth profiles of the oxygen isotope distribution in oxide scales formed on cobalt coated samples during two-stage oxidation at temperatures from 850 °C to 1000 °C can be seen in figure 5.23. The oxide scales generally show two distinct regions of well separated oxygen distributions. The inner part of the scale, close to the metal-oxide interface, consists mainly of ^{18}O, while the outer region is dominated by ^{16}O. The clear separation of the two regions indicates oxide scale growth primarily from the gas-oxide interface by outward diffusion of cations.

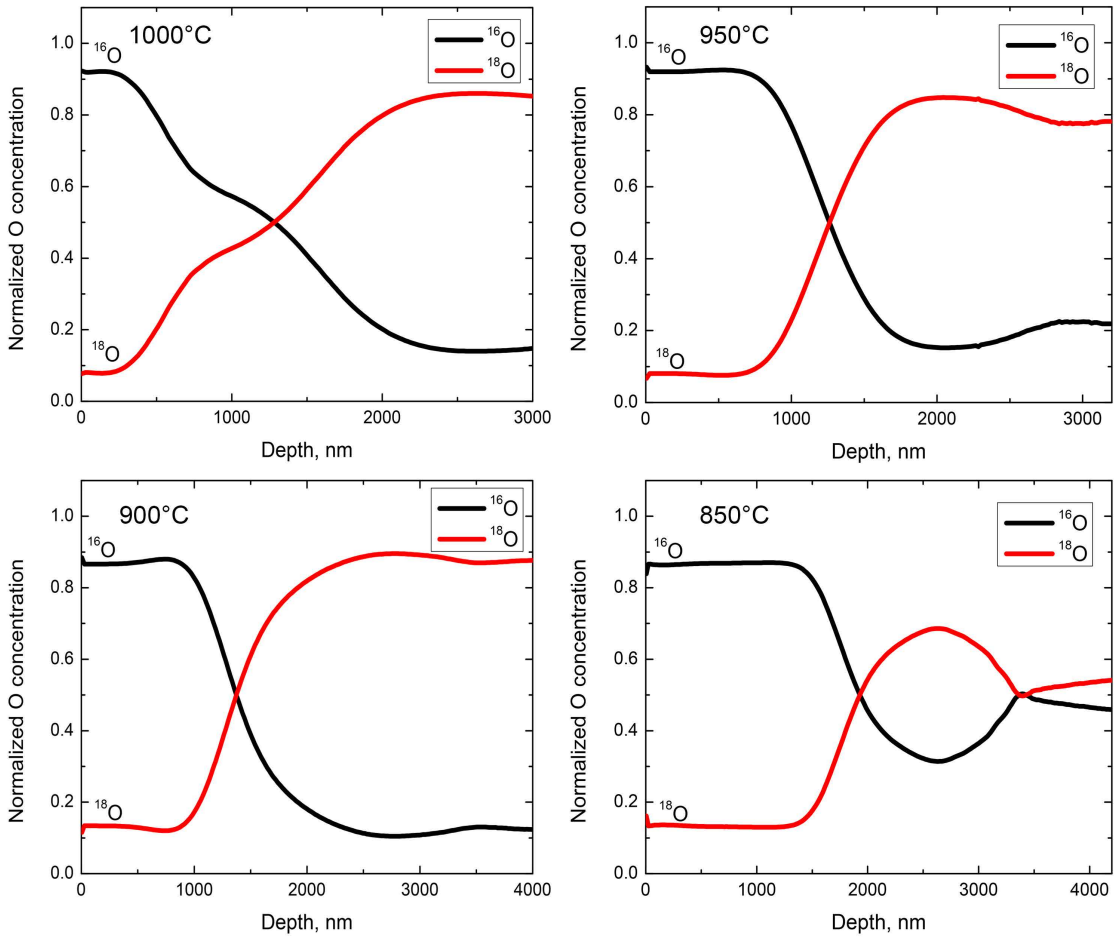

Figure 5.23: Distribution of oxygen isotopes in oxide scale formed during two-stage oxidation at temperatures from 1000 ° to 850 °C for 80 min to 97 hours.

At the lower temperatures, the innermost part of the oxide exhibits more narrow oxygen distributions. Increased ^{16}O in this region could indicate inward transport of oxygen, or the presence of an oxide phase formed on the alloy surface prior to oxidation in $^{18,18}O_2$. At 1000 °C, the outer part of the scale show increased concentration of ^{18}O, indicating significant oxygen diffusion in this region.

The depth profiles at lower temperatures show rounded distribution curves in the inner part of the oxide, indicating a contribution to isotope variation apart from scale growth. This contribution could be isotope exchange with the surrounding gas. Some general trends appear:

- Increased temperature broaden the ^{16}O-^{18}O switch area, indicating more rapid interdiffusion of oxygen ions.
- Features from possible isotope exchange with surrounding gas, to form $^{16,18}O_2$, in oxide scales formed prior to introduction of ^{18}O appear more steep as a function of temperature, indicating that the amount of oxygen exchanged is increasing with increasing temperature

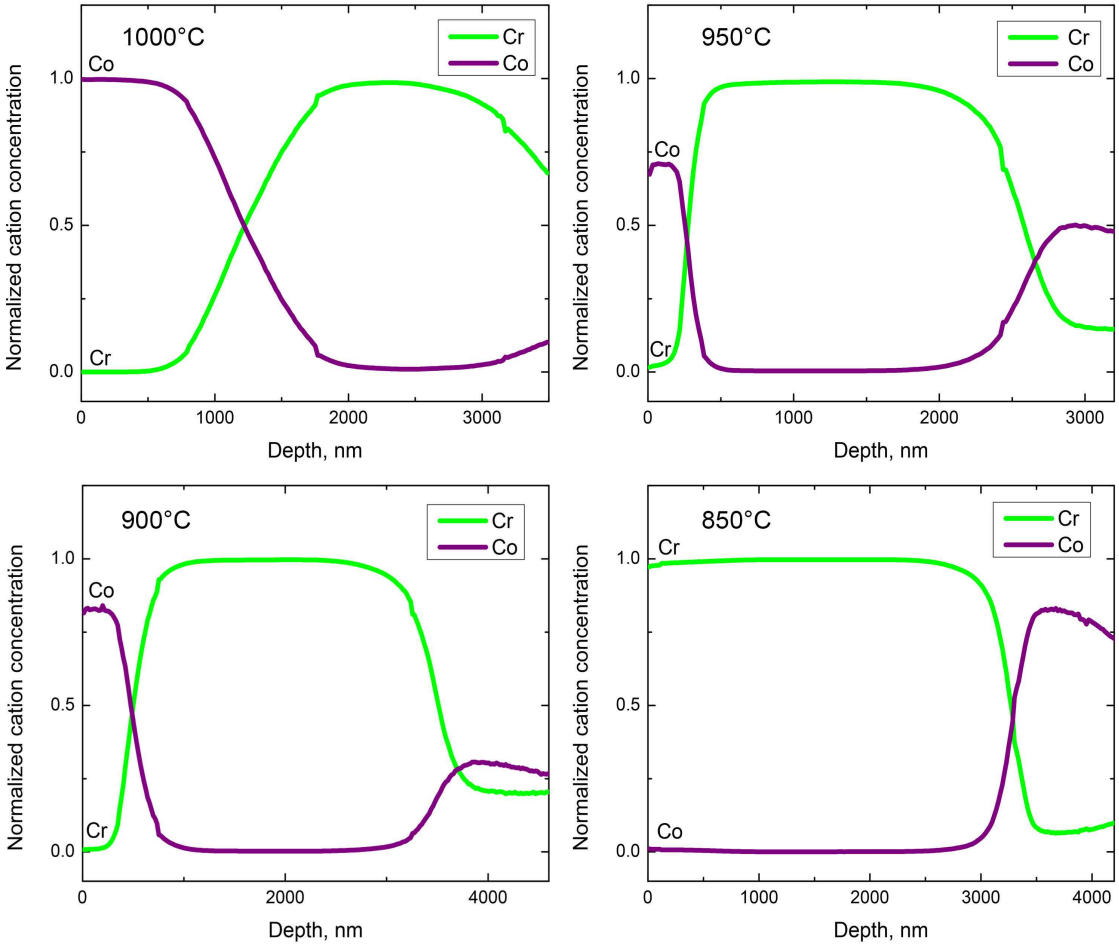

Figure 5.24: Distribution of Cr and Co in oxide scale formed at temperatures from 1000 ° to 850 °C for 80 min to 97 hours.

5.3.1 Cation distribution

SIMS depth profiles showing Cr and Co distributions in the formed oxide scales can be seen in figure 5.24. The distributions show two regions, where one is rich in Co and the other is rich in Cr. In the outer part of the oxide scale, cobalt is dominating the oxide scale distribution. This indicates a cobalt rich oxide phase in the outer region, probably a spinel phase Co_3O_4 or $(Co, Mn)_3O_4$. The region where chromium is dominating is assumed to consist of Cr_2O_3. Increased concentrations of cobalt are observed in the inner part of the oxide scale, indicating that a cobalt oxide phase is formed prior to the oxidation in $^{18,18}O_2$, as was suggested from oxygen isotope depth profiles. At the lower temperatures, the distributions of Co and Cr are well separated indicating a defined changeover from cobalt spinel to chromia. At 1000

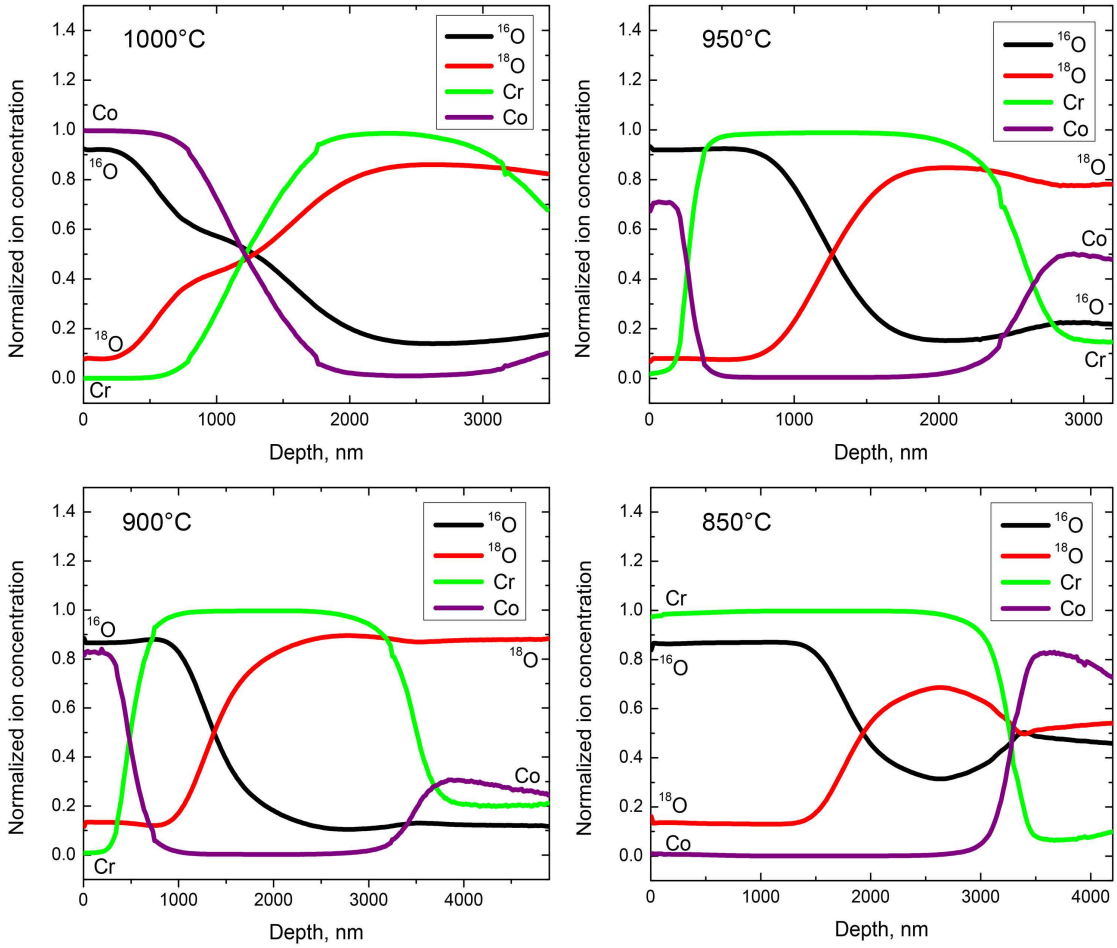

Figure 5.25: Distribution of oxygen isotopes, Cr and Co in oxide scale formed at temperatures from 1000 ° to 850 °C for 80 min to 97 hours.

°C, the transition region between the spinel phase and Cr_2O_3 is broadened, indicating more rapid interdiffusion of cations at this temperature.

Figure 5.25 show distributions of both oxygen isotopes and cations in the formed oxide scales. At 1000 °C, the reduced separation of ^{18}O and ^{16}O in the outer region of the oxide scale, in the cobalt rich region, could indicate inward diffusion of oxygen occurring in the spinel phase. The formation of oxide can thus occur within the oxide scale, and not only at the gas-oxide interface. The distribution profiles at lower temperatures have sharp transition regions and are well separated, indicating oxide scale growth governed by outward diffusion of cations. At 850 °C, the outer scale appear to consist of Cr_2O_3 and not the cobalt rich spinel phase. This could be due to rapid formation of a Co_3O_4 phase prior to introducing $^{18,18}O_2$, but no conclusions can be

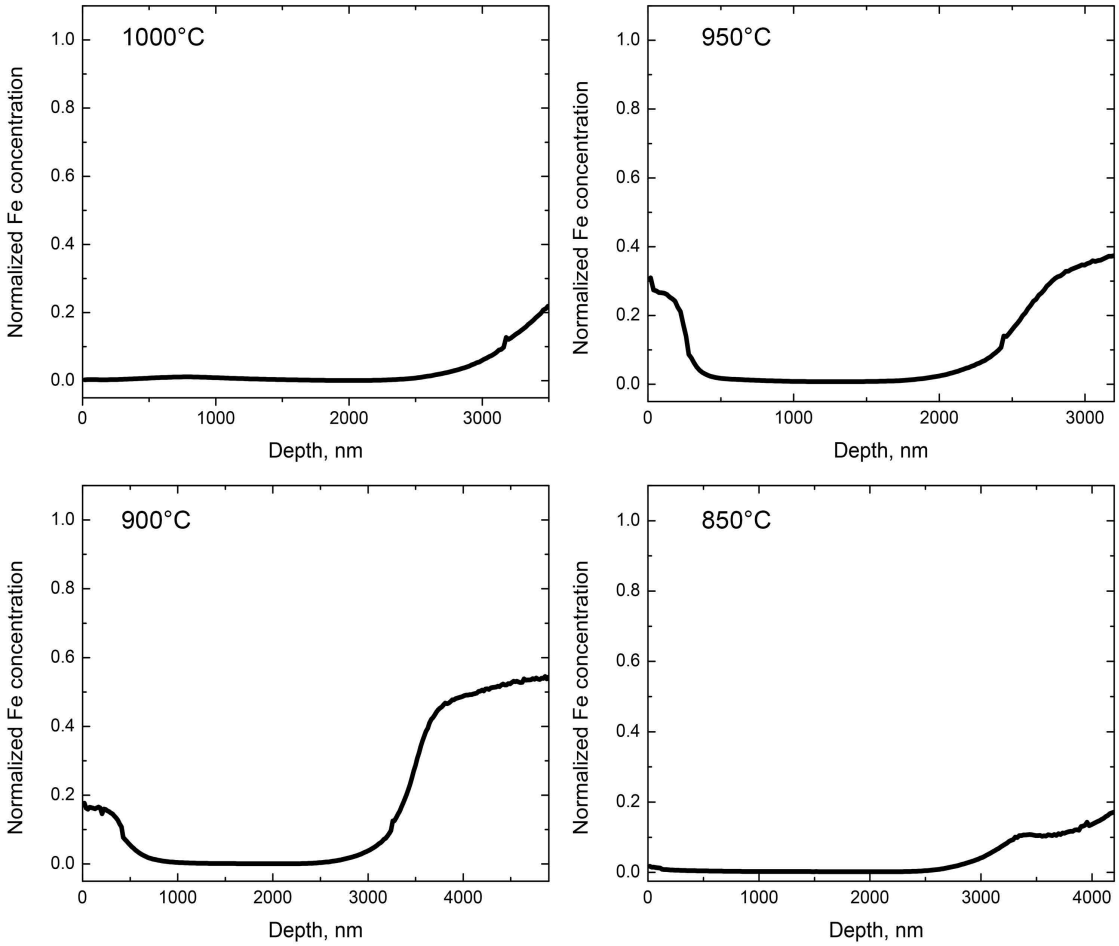

Figure 5.26: Distribution of Fe in oxide scale formed at temperatures from 1000 ° to 850 °C for 80 min to 97 hours.

drawn without further investigations.

The distributions of Fe and Mn in the formed oxide scales are harder to detect due to lower secondary ion intensities. Iron distributions at temperatures from 850 °C to 1000 °C can be seen in figure 5.26. At temperatures from 900 °C to 950 °C, significant amounts of Fe are present in the outer part of the oxide scales. This is probable to occur in the cobalt rich spinel phase, indicating a iron containing $(Co,Fe)_3O_4$ spinel. No dissolved iron appear to be present in the chromia phase. The distribution of Mn in the oxide scale formed at 950 °C can be seen in figure 5.27. Due to the very low intensity, the uncertainty is too high and the distribution of Mn in the formed oxide scales is thus hard to determine. Sputtering by negative oxygen ions could increase the signal count from Mn, but this will remove the

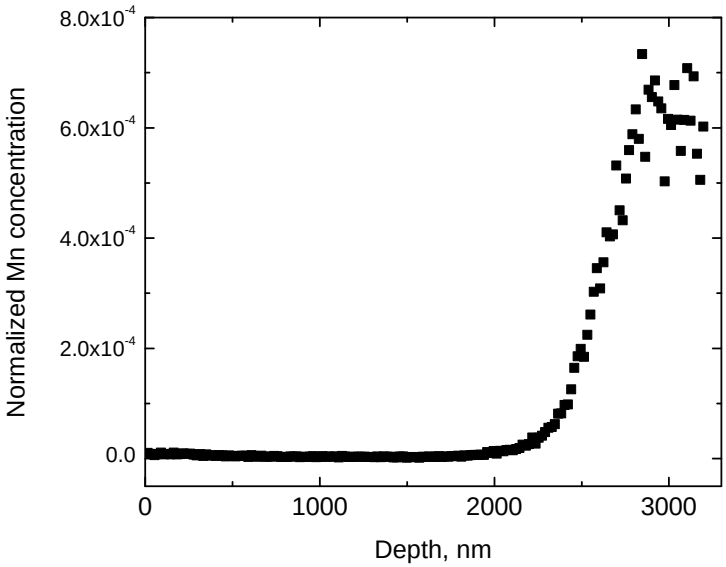

Figure 5.27: Distribution of Mn in oxide scale formed at 950 °C for 150 min.

possibility of simultaneously investigating the distribution of oxygen ions.

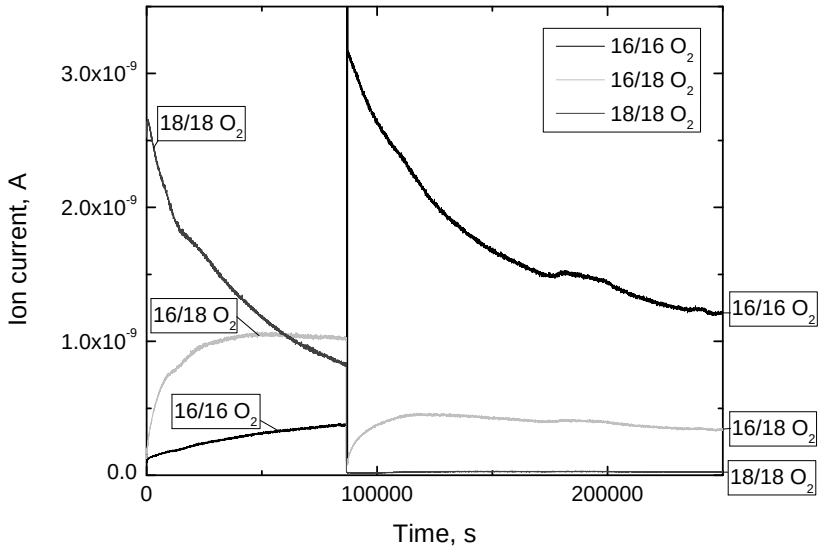

Figure 5.28: Ion current measured by mass spectrometry for $^{16,16}O_2$, $^{16,18}O_2$, and $^{18,18}O_2$ as a function of time at 850 °C.

5.3.2 Gas exchange in oxide scales during oxidation

Gas exchange between the grown oxide scales and the surrounding atmosphere could occur during oxidation and influence the ion distributions detected by SIMS. A mass spectrometer was thus connected during the oxidation experiments to record the atmosphere development as a function of time. Figure 5.28 show the detected ion currents at 850 °C as a function of time. At both temperatures, small amounts of $^{16,18}O_2$ is detected during the first stage of the oxidation. This indicates the presence of an ^{16}O oxide scale prior to introducing $^{18,18}O_2$, and that ^{16}O to some extent is exchanged by ^{18}O in the grown oxide. Due to the small amounts, gas exchange is not assumed to significantly affect the ion distributions.

5.4 HT-ESEM

HT-ESEM was used to observe the oxide growth on uncoated and cobalt coated samples in-situ. All samples were oxidized in 0.006 atm pure H_2O in low vacuum at temperatures from 500 °C to 950 °C. The observed growth was highly affected by surface defects and the microstructure of the alloy. The oxide scale development of an uncoated sample oxidized from 500 °C to 900 °C can be seen in figure 5.29. The first visible oxide growth was observed at 650 °C, initially developing at surface defects, such as cracks and in the rolling direction of the steel foil. Due to the nature of HT-ESEM experiments, it is difficult to determine the exact starting point for oxidation.

The morphology is observed as non-unform blade shaped grains. During the first 90 minutes of oxidation, the grains undergo horizontal expansion and the edges of the grains are sharpened. Locations with negligible surface defects were dominated by the formation of thin protrusions often referred to as "whiskers". Whiskers formed during oxidation of an uncoated sample can be seen in figure 5.31. The whiskers had relatively uniform length of about $0.5\mu m$, with the exception of a small number of longer and thicker whiskers of approximately $3\mu m$.

The oxide growth on a cobalt coated sample under similar conditions can be seen in figure 5.30. The first visible oxide growth was observed already at 550 °C, and the overall growth appeared highly uniform.Unlike uncoated samples, the oxide growth on cobalt coated samples was not affected by surface defects. The oxide scale morphology was generally blade formed grains with sharp edges, seemingly growing in all observable directions.Thin whiskers were also observed for cobalt coated samples after 80 minutes of oxidation. After 100 minutes of oxidation, the observed whiskers expanded horizontally and developed into blade like formations, identical to the rest of the scale.

Oxide scales formed on cobalt coated samples exhibited less charge accumulation from the incident electron beam, indicating oxides with higher electrical conductivity than the oxides formed on uncoated samples. Surface analysis of samples oxidized during HT-ESEM indicated high concentrations of iron (50 at.%). This could be a result of signals collected from the underlying steel, or possibly due to formation of iron oxides caused by a water vapour atmosphere. Cross sections analysed by EDS line scans indicated Cr_2O_3 and an iron rich spinel phase. Both oxides were low in manganese.

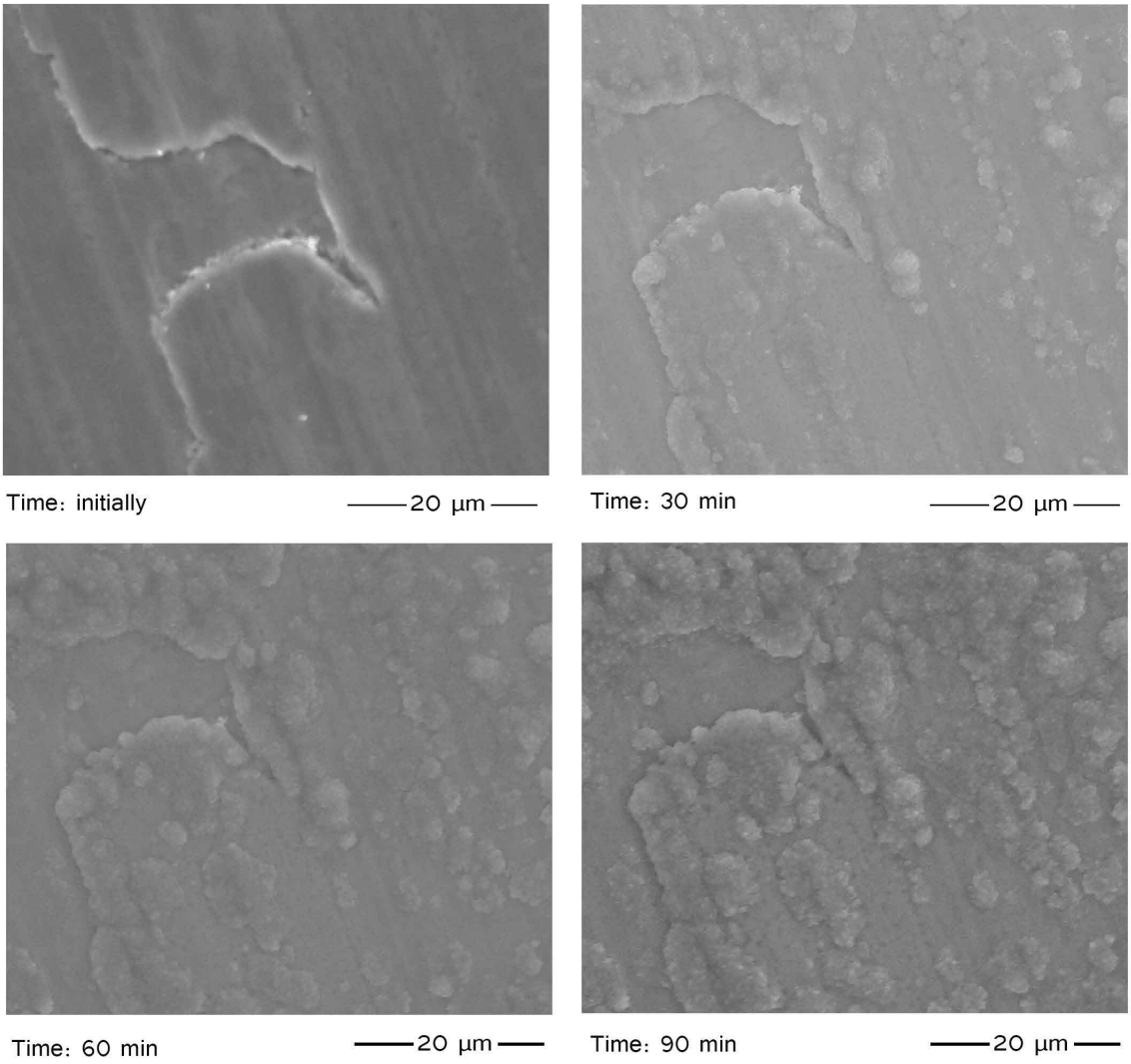

Figure 5.29: Uncoated sample oxidized using HT-ESEM in 600 Pa H_2O in the temperature range of 500 °C to 900 °C.

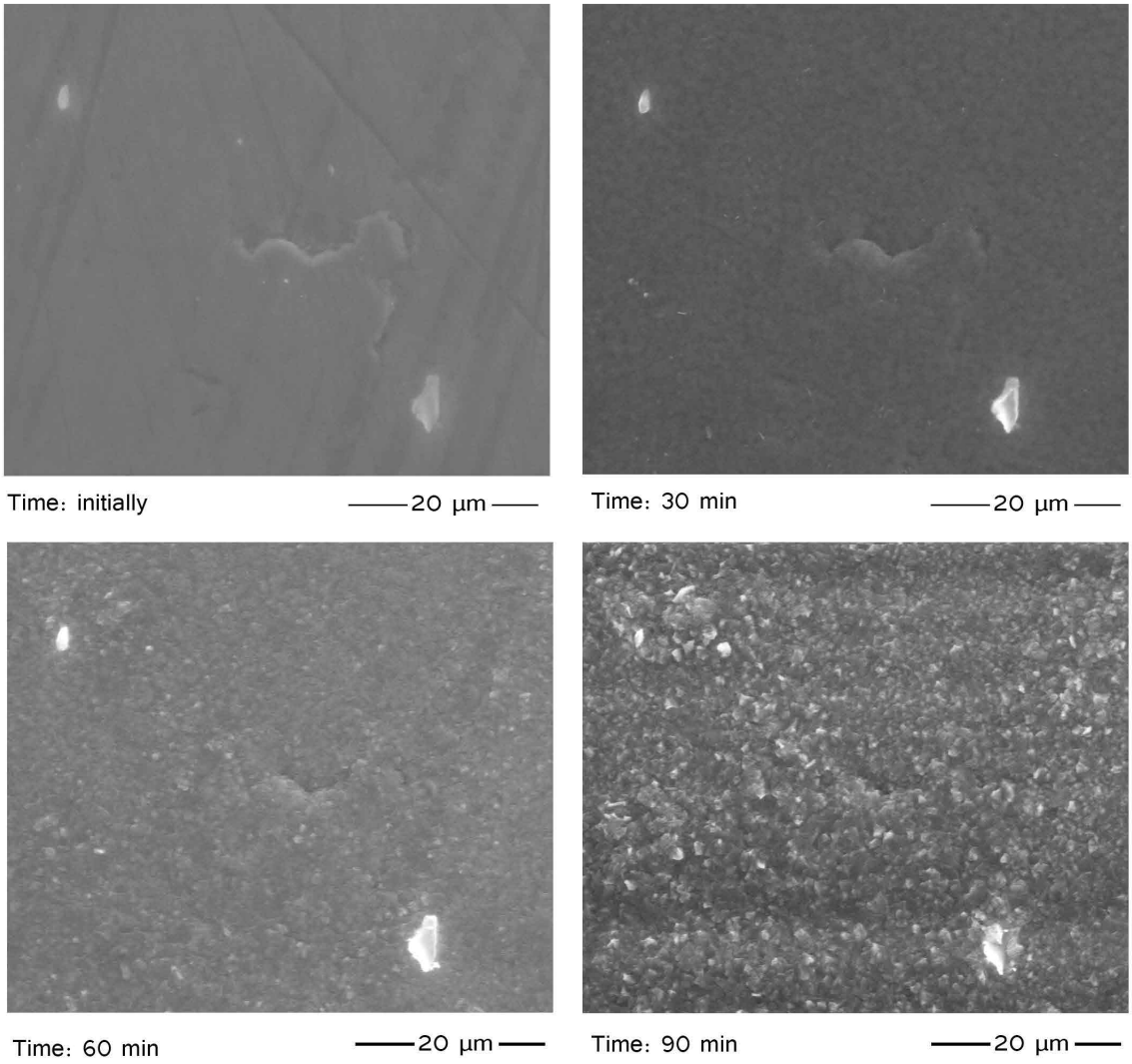

Figure 5.30: 600 nm Co coated sample oxidized using HT-ESEM in 600 Pa H_2O in the temperature range of 500 °C to 900 °C.

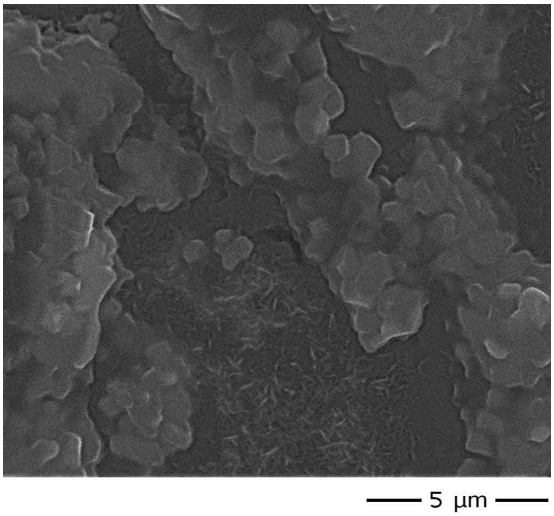

Figure 5.31: Whiskers and blade structures observed during oxidation of uncoated samples during HT-ESEM.

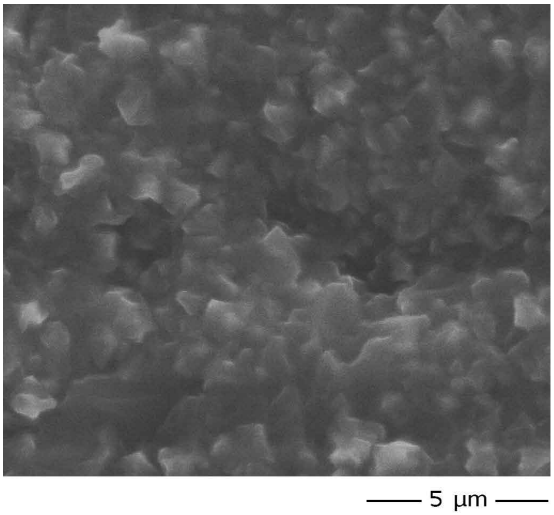

Figure 5.32: Blade structures observed during oxidation of 600 nm Co coated samples during HT-ESEM.

5.4.1 Comparison TG

To evaluate HT-ESEM as an experimental method in high temperature oxidation, samples oxidized during HT-ESEM should be compared to samples oxidized by more conventional methods, for instance thermogravimetry.

Samples oxidized in HT-ESEM are exposed to low vacuum, and the gaseous environment used for all samples in this study was 0.006 atm pure H_2O. These conditions are difficult to replicate by the thermogravimetric equipment used in this work. The surface of cobalt coated samples oxidized using the TG setup, for 5 to 120 minutes in wet air at 900 °C, can be seen in figure 5.33. Wet conditions in the TG setup correspond to a p_{H_2O} of 0.025 atm, as explained in chapter 4. This p_{H_2O} is approximately 4 times higher than what samples oxidized using HT-ESEM are exposed to. In addition, the TG experiments were conducted at atmospheric pressure. The samples oxidized using HT-ESEM are mounted flat, while those oxidized by TG are hanging freely and exposed to a gas flow. This could possibly affect the oxide scale morphology. The effect of temperature must also be taken into consideration, as samples oxidized using HT-ESEM is gradually heated from room temperature, and samples oxidized by TG is lowered directly from room temperature into the high temperature furnace. As two different furnaces are used in the HT-ESEM and TG setups, a deviation in temperature could also be present.

As mentioned, the samples oxidized by TG were exposed to wet air. There will thus also be a difference in p_{O_2} for samples oxidized during HT-ESEM compared to those oxidized in wet air. The weight related parabolic growth rate constants for cobalt coated and uncoated samples, see figure 5.19, were found to be independent of p_{O_2}. The carrier gas used to transport water vapour was therefore assumed not to significantly affect the oxidation kinetics for the samples oxidized by TG. However, the carrier gas, air, could still affect the morphology of the formed oxide scales.

The samples oxidized by TG for 5 minutes and 30 minutes show continuous and uniform oxide scales of flat, smooth-edged grains. The scales are in addition porous with intragranular voids. The samples oxidized using HT-ESEM did not form similar grains or appear porous for the same oxidation times. The samples oxidized by TG for 60 minutes and 120 minutes formed continuous scales of flat, blade-like formations, similar to the morphologies observed for samples oxidized using HT-ESEM. A comparison of cobalt coated samples oxidized during HT-ESEM and TG for 2 hours at 900 °C can be seen in figure 5.34.

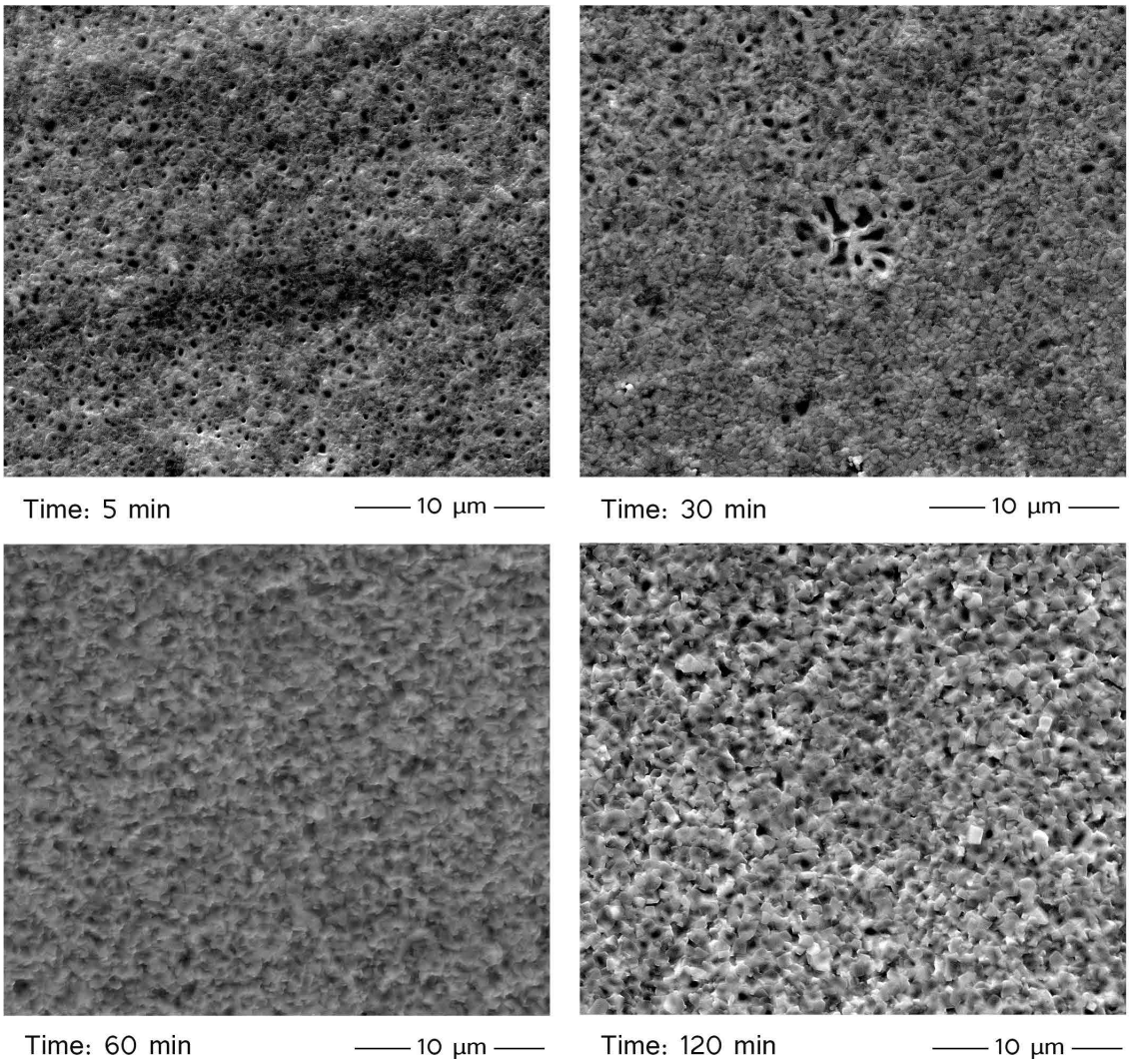

Figure 5.33: 600 nm Co coated samples oxidized by TG at 900 °C for 5 min, 30 min, 60 min and 120 min.

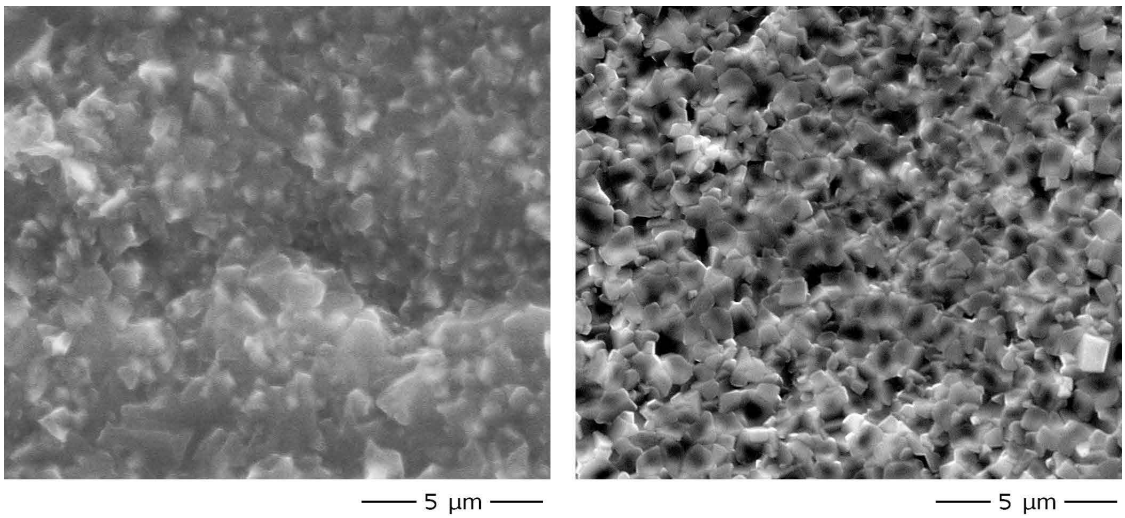

Figure 5.34: Comparison of oxide scales on cobalt coated samples oxidized for 2 hours at 900 °C using HT-ESEM and TG. Left: HT-ESEM, Right: TG

Chapter 6

Discussion

The discussion part of this work will be divided into the following sections:

- Microstructure, morphology and interface properties
- Oxidation behaviour of Sanergy HT
- Evaluation of HT-ESEM as experimental method

6.1 Microstructure, morphology and interface properties

The microstructure and morphology of oxides scales are very sensitive to external influences such as temperature, surrounding atmosphere, time and surface preparation. During oxidation of multicomponent alloys, multiple growth processes occur simultaneously, resulting in an infinite number of morphological variations. Due to this high complexity, a complete analysis and understanding of the nucleation and growth of surface features is regarded as nearly impossible. However, the morphology may provide important information about the mechanisms governing the oxide scale growth. This section will thus attempt to elucidate the general trends and some of the important features occurring during high temperature oxidation of a multicomponent alloy. The following will be discussed:

- the effect of temperature and gas composition on scale microstructure
- formation of oxide ridges, whiskers and blades
- morphology of the oxide-alloy interface

The emphasis will be on the formation and development of these features, and how this can be related to dominating transport processes in the oxide.

6.1.1 Effect of temperature and gas composition

The microstructure and morphology of the oxide scales grown on Sanergy HT have shown to be dependent on both temperature and reaction atmosphere. The initial formation of oxide particles appears to grow epitaxially the metal surface, and the resulting oxide scales are relatively dense and adherent.

Cobalt coated samples oxidized under reducing conditions show uniform growth of equiaxed, crystalline particles. The homogeneous, single phase scale is due to the preferential oxidation of Co at the surface. The submicron, equiaxed grains sinter with increasing temperature, leading to larger flat grains with protruding oxide ridges and pores at the grain boundaries. Large islands of spherical precipitations, identified as Cr_2O_3, appear for temperatures above 925 °C. Is is not known whether these large chromia precipitations occur only as a result of an increased diffusion coefficient of chromium as a function of temperature, or due to reduced availability of Co. Most likely, the cause is a combination of the two. The Cr_2O_3 precipitations appear to initially form as individual protruding features, growing both within grains and at grain boundaries of the cobalt oxide surface. This indicates outward diffusion of Cr both through the oxide lattice and the grain boundaries.

Uncoated samples show larger variations in morphology as a result of the direct interaction between oxygen and the number of different elements present in the alloy. For short oxidation times, around 45 hours, the oxide scales seem apparently one-phase, consisting of crystalline particles with increasing size distribution as a function of temperature. After 150 hours, large differences are visible at the various temperatures. This indicates that the initially formed oxides are those of the main compositional elements, namely iron and chromium. Oxygen active elements present in smaller amounts, for instance Mn, are limited by diffusion from the alloy interior and will reach the surface at a later stage. Early formation of these oxides near the oxide-alloy interface by inward diffusion of oxygen is not excluded, but is difficult to determine by surface analysis only. After longer oxidation times, the surface after oxidation under reducing conditions at 850 °C is covered by whiskers. The formation of whiskers will be discussed further in section 6.1.2. At 900 °C, large crystalline grains rich in Mn are observed, indicating rapid diffusion of Mn in Cr_2O_3, compared to that of Cr, at this temperature. With increasing temperature the size distribution of grains reduces, and the growth of large Mn rich grains is no longer favoured. The ratio between the diffusion coefficient of Mn and the diffusion coefficient of Cr in Cr_2O_3 appear to reach a maximum at around 900 °C. This can indicate that Mn is also transported through grain boundaries of Cr_2O_3, as is also suggested by other studies.[36,45]

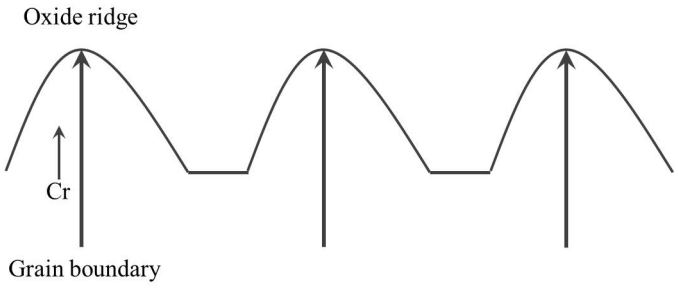

Figure 6.1: Suggested growth mechanism of oxide ridges through grain boundary transport, modified from Polman et al.[49]

Oxide scales formed under oxidizing conditions are significantly more buckled and deformed than under reducing conditions. There are several sources for stresses and strains in oxides. Stresses will occur in a growing oxide scale as a result of crystallographic mismatch between the alloy surface and the oxide scale. Large growth stresses will also be introduced when counter-current diffusion of cations and anions dominates the scale growth, as the oxide will form not only at the gas-oxide interface, but also at the oxide-alloy interface and within the oxide scale. Under reducing conditions, uniform growth with a more flat, stress free oxide scale indicates that the oxide growth occur mainly from the gas-oxide interface by outward cation diffusion.

6.1.2 Oxide ridges, whiskers and blades

Oxide ridges are observed on the surface of cobalt coated samples oxidized at temperatures above 925 °C for 150 hours under reducing conditions, see figure 5.2. Although the specific morphology is not expected to extend far below the gas-oxide interface, morphological indications of certain growth processes can be used to support observations from other measurements. The oxide ridges appear to be located on top of grain boundaries, which is also reported by Hsu et al.[46] This localized scale thickening is suggested to result from transport of chromium, oxygen, or both along grain boundaries in Cr_2O_3.[37,47] Raynaud and Rapp[48] also report that shallow, dish-shaped oxide grains with slight ridges at their grain boundaries are probable to result from growth by grain-boundary diffusion. It is assumed that the grain boundaries extend through the ridge, enabling oxide formation and growth of the ridge as ions migrate through the center, see figure 6.1. The grain-boundary ridges appear to become more protruding with decreasing temperature. This could indicate that diffusion along grain boundaries is significant at lower temperatures, but less important at higher temperatures when the lattice diffusion of chromium is faster. A difference in image contrast is observed by

the ETD detector used in SEM, indicating a change in phase composition between the bulk and the grain-boundary ridges. Due to the limited resolution of EDS analysis in SEM, determining the phase composition at the grain-boundary ridges is difficult. Preferential transport of oxygen along grain boundaries is also suggested to cause detachment of oxide scales from the alloy surface and scale cracking at high temperatures.[37,47,50]

Thin protrusions, often referred to as *whiskers*, are observed for uncoated samples oxidized under reducing conditions at 850 °C. The whiskers were identified to consist of Cr_2O_3. Whisker formation is also observed by HT-ESEM for all samples in the initial stages of oxidation. The thin geometry of the whiskers indicates that the growth occurs either at the tip or from the base of the whisker. If the whiskers grow from the tip, chromium must be transported outwards from the alloy. This transport of chromium can occur either within the whisker, by surface diffusion or both. At the temperatures measured in this work, the formation and growth of chromia whiskers during the first hour of oxidation appear too fast to be a result of lattice diffusion. Generally, whiskers are found to grow around screw dislocations[51,52] and thus have a hollow core. It is assumed that the chromia whiskers formed in this study also resemble this hollow structure. Takagi[52] found that whiskers and blade-like platelets grow from the tip by surface diffusion from the base. This growth mechanism is supported by the development and growth of whiskers observed by HT-ESEM in this work. If surface diffusion from the base occurs, lateral growth of the whiskers would be expected. This is confirmed by in-situ HT-ESEM, where whiskers after some time expand to blade-like platelets.

Whiskers are mostly observed at the lower temperatures, around 850 °C. This could be due to the smaller activation energy for surface diffusion than lattice diffusion at these temperatures. Lattice diffusion will become more favourable as the temperature is increased, and eventually eliminate whisker formation. Another possibility is that the chromia whiskers evaporate easily from the surface at high temperatures due to their large surface areas. The appearance of whiskers at the surface of uncoated samples after 150 hours of oxidation at 850 °C under reducing conditions could indicate that the scale formation happens predominately within the oxide scale, or at the oxide-alloy interface, due to inward diffusing oxygen and not at the gas-oxide interface as a result of cation diffusion. It is also possible that evaporation of whiskers do not occur under these conditions due to a combination of low temperature and low p_{O_2}.

6.1.3 Morphology of the oxide-alloy interface

Uncoated samples oxidized at elevated temperatures under oxidizing conditions show deformed oxide-alloy interfaces, see figure 6.2, while under

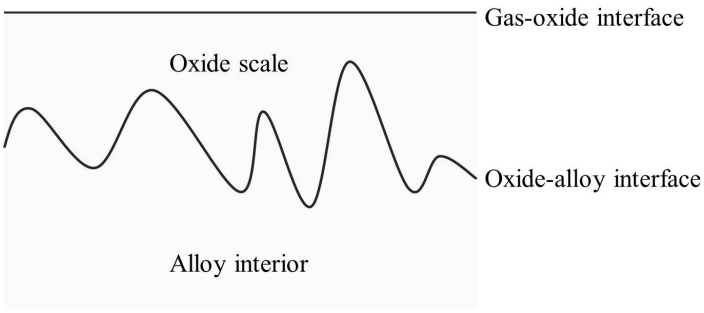

Figure 6.2: Schematic illustration of deformed oxide-alloy interface, as seen for uncoated samples oxidized under oxidizing conditions at 1000 °C.

reducing conditions the oxide-alloy interface is flat. In their theoretical approach, Asaro and Tiller[53] treated the interface between a material under stress and its surroundings as a phase front. The phase front can either be smooth and regular, which is observed for uniform oxide growth, or buckled, which often lead to cracking. They also assume the phase front to change position and shape through both surface and volume diffusion. Large introduced growth stresses and ballooning of oxide-alloy interfaces can indicate that the oxide growth is dominated by counter-diffusion of both anions and cations. This is also suggested by Kofstad.[54] Oxide-alloy interfaces of samples oxidized under reducing conditions are flat, indicating scale growth predominately by outward cation diffusion.

Alloying elements can segregate to grain-boundaries and interfaces in the metal-oxide system, affecting defect concentrations and mechanical properties in these regions. High concentrations of Mn at grain boundaries have been reported for oxide scales grown on Fe-Cr alloys.[55] The two interface regions discussed in this section is the oxide-alloy interface and the oxide-oxide interface between the spinel phase and Cr_2O_3 in the duplex oxide layer.

The oxides scales formed under reducing conditions at high temperatures did show indications of poor adherence and gaps at the alloy-oxide interface. Voids at the alloy-oxide interface are frequently encountered for oxide scales growing predominately by outward diffusion metal ions. The outward diffusion of metal ions will lead to accumulations of metal vacancies near the alloy-oxide interface. The oxide scale will in addition grow from the gas-oxide interface, causing essentially no new oxide phase to form and fill voids within the scale. Oxide phases from alloying elements such as Si, Ti, Mn, Nb and Mo to be present in the alloy-oxide and oxide-oxide interfaces of samples oxidized in this work.The presence of such oxides at interfaces can influence

mechanical properties of the oxide scale, and also the transport of ionic species across these regions. Oxide scales formed under oxidizing conditions revealed no visible gap at the alloy-oxide interface. This could be due to inward diffusing oxygen, or other alloying elements, forming oxides near the alloy-oxide interface. It is thus probable that the interfacial gap observed at low p_{O_2} is caused by less precipitated oxide phases in the interface region under reducing conditions due to variations in solubility of these oxides in Cr_2O_3.

6.2 Oxidation behaviour of Sanergy HT

The oxidation of Sanergy HT at temperatures between 850 °C and 1000 °C under oxidizing and reducing conditions show parabolic oxidation kinetics as a function of time. Parabolic rate kinetics indicate that the oxide growth is limited by diffusion of ions through the oxide scale. Diffusion-controlled rate kinetics are commonly observed for chromia forming alloys.[7,56]

A duplex oxide scale is formed during oxidation of uncoated samples consisting of a continuous inner layer of Cr_2O_3 near the oxide-alloy interface and a (Cr, Mn)$_3O_4$ spinel phase near the gas-oxide interface. Cobalt coated samples for similar duplex scales, but with a (Co, Mn)$_3O_4$ spinel phase. The formation of a cobalt rich spinel phase in the outer part of the scale indicates that the oxidation of Co is favoured and more rapid than the oxidation of outward diffusing chromium. Increased concentration of Fe has been found in (Co, Mn)$_3O_4$ compared to (Cr, Mn)$_3O_4$, indicating higher solubility of iron in the cobalt spinel.

Pores are observed in the outer region of the alloy, and the pore density increases as the alloy-oxide interface is approached. These pores are expected to be formed by accumulated metal vacancies by outward metal diffusion from the alloy. As the metal depletion is largest close to the alloy-oxide interface, increased alloy porosity in this region would be expected. Pore formation in the outer part of Sanergy HT samples is also reported by other sources.[45,57]

6.2.1 Oxide scale growth mechanisms

From HT-ESEM it is observed that oxide particles initially nucleate at the alloy surface and rapidly increase in number and size until a continuous oxide film is completely covering the surface. Further growth then proceeds by outward diffusion of Fe, Mn and Cr ions and inward diffusion of oxygen.

The nucleation and growth on cobalt coated samples is observed to be uniform and seemingly unaffected by surface defects. Uncoated samples exhibit less uniform growth, where the formation of oxide particles is favoured at large surface defects. This difference could be explained by the initially formed oxides on uncoated and cobalt coated samples. For uncoated samples, both Cr_2O_3 and (Cr, Mn)$_3O_4$ are assumed to be formed in the early stages of oxidation, probably in addition to iron oxides such as Fe_2O_3 and Fe_3O_4. Surface defects are favourable nucleation centres due to high concentrations of dislocations, which could explain the increased nucleation and growth in these locations. When uncoated samples are exposed to oxidizing atmospheres, oxygen molecules will adsorb and react with the alloy directly. As the alloy consists of several elements with varying oxygen affinity, rapid surface reactions could lead to a number of different oxide phases. For cobalt coated samples, the initial oxidation will occur between oxygen and metallic cobalt. The oxide would thus essentially be one phase, and more uniform growth is expected.

In uncoated samples, the formation of a (Cr, Mn)$_3O_4$ spinel phase is favoured due to the oxygen affinity of Mn. The spinel phase is located on top of the Cr_2O_3 layer, presumably growing at the gas-oxide interface by outward diffusing cations. The high concentration of Mn in the outer spinel indicates rapid diffusion of Mn in chromia , compared to that of Cr, in the measured temperature range. High lattice diffusivity of Mn in chromia is also reported by other studies.[12,45,58,59] In addition, Mn can be transported through rapid diffusion paths such as grain boundaries and interfaces, as suggested by other studies.[45,60] Due to the large amounts of available Cr, it is assumed that the growth of (Cr, Mn)$_3O_4$ is limited by the diffusion rate of Mn from the alloy and in Cr_2O_3. The growth of the (Co,Mn)$_3O_4$ spinel layer formed on coated samples is more rapid at lower temperatures than the growth of (Cr, Mn)$_3O_4$, indicating that the growth rate is less dependent on Mn diffusion rates. This is assumed to be caused by the access to a finite source of cobalt at the surface. The concentration of chromium in the cobalt spinel layer is small (3-9 at.%), indicating slow diffusion of Cr in (Co, Mn)$_3O_4$.

The Cr_2O_3 scale can either grow at the oxide-alloy interface by inward diffusion of oxygen or at the spinel-chromia interface by outward diffusion of Cr and inward transport of oxygen through the spinel layer. From SIMS depth profiles obtained in this work, significant contributions of inward diffusing oxygen through the chromia layer are not observed. However, there are indications of inward oxygen transport in the outer spinel oxide. The Cr_2O_3 scale is thus assumed to initially form at the scale-alloy interface when the spinel scale is very thin, and later grow at the spinel-chromia interface

predominately by outward diffusing Cr ions and inward transport of oxygen through the spinel layer.

In all oxidized samples, the Cr_2O_3 part of the oxide layer is observed to be the thicker than the spinel phase. This is probably due to the high amount of chromium available for oxidation in the alloy. The ratio between chromia and spinel in the oxide scale increases as a function of temperature, which could indicate that the growth rate of Cr_2O_3 is more temperature dependent than that of the spinel phase. The increased growth rate of Cr_2O_3 as a function of temperature could result from a higher activation energy for chromium diffusion than for Mn diffusion. Variations in defect concentrations as a function of temperature can also occur, affecting the transport of reacting species in the scale.

6.2.2 Oxide growth rates

It is found that cobalt coated samples show larger weight gains as function of time than uncoated samples at all measured temperatures, under both oxidizing and reducing conditions. This is assumed to be a result of rapid oxidation of metallic cobalt, compared to that of Cr_2O_3 and $(Cr, Mn)_3O_4$ on uncoated samples. The volatilization of chromium on uncoated samples will also affect the weight gain under oxidizing conditions.

Accelerated growth kinetics are observed for cobalt coated samples after 90 hours of oxidation at 1000 °C under reducing conditions. Uncoated samples do not exhibit non-parabolic kinetics under reducing conditions, but under oxidizing conditions breakaway oxidation is observed after 80 hours.

Breakaway oxidation can occur when the protective properties of the formed oxide scales are reduced. If the growing oxide has a larger volume than the underlying alloy, compressive stresses will accumulate in the scale. Assuming the oxide scale grows by outward diffusing metal ions, the volume of the alloy will reduce. As the oxide scale is adhered to the alloy surface, a reduction in the volume of the alloy will cause stresses both normal and parallel to the surface. For scales growing at the gas-oxide interface purely by outward diffusion cations, or at the oxide-alloy interface purely by inward diffusion oxygen, the formation of new oxide will lead to small stresses. However, if the oxide scale grows by counter-diffusion of both cations and anions, large growth stresses will develop and affect the mechanical properties of the scale. To relieve the build-up of growth stresses in oxide scales, the scales may either deform, for instance by forming cracks, or detach from the alloy surface.

Cracks function as convenient diffusion paths for molecular oxygen in the surrounding atmosphere, causing the growth rate to increase rapidly. The breakaway oxidation observed for uncoated samples under oxidizing conditions could thus be caused by significant cracking of the scale and subsequently inward transport of oxygen along these cracks. Under reducing conditions, the amount of available oxygen is significantly less, which could explain why breakaway oxidation do not occur. It is also possible that the starting point for breakaway oxidation of uncoated samples under reducing conditions is prolonged to after 150 hours, which was the maximum hours measured. Morphological observations support the suggestion of less available oxygen for transport along cracks under reducing conditions. Oxide scales formed under reducing conditions are less buckled than oxide scales formed under oxidizing conditions, see figure 5.6, which indicates that reduced amounts of compressive growth stresses accumulate in the scales during oxide growth. Less introduced growth stresses could indicate that oxide growth under reducing conditions occur predominately by outward diffusion of cations, while counter-current diffusion of both anions and cations contribute under oxidizing conditions. Contributions from inward diffusing oxygen were confirmed by SIMS depth profiles of cobalt coated samples at high temperatures, see figure 5.23.

A complicating factor for deformation mechanisms in oxide scales at high temperatures is the presence of a chemical potential gradient. The gradient in chemical potential will lead to varying defect concentrations across the oxide scale. Due to these variations, the rates and degree of deformation will also vary. Under reducing conditions, the gradient in p_{O_2} from the gas-oxide interface to the oxide-alloy interface is small. As nonstoichiometry in oxides can vary significantly as a function of p_{O_2}, one could thus assume that the largest variations in defect concentrations across the oxide scale are present under oxidizing conditions. As deformation processes often involve diffusion of both anions and cations, regions with increased concentrations of defects contributing to anion transport, such as interstitial oxygen or oxygen vacancies, could be more prone to deformation than regions governed by cation defects only. Generally, oxygen defects are assumed to be minority defects in chromia.[7]

In addition, the oxide scale formed on Sanergy HT consists of more than one oxide phase. If the growth of one oxide phase is favoured under certain conditions, this could dominate the overall oxidation kinetics. Also, the amount of compressive stresses may vary for the different phases. The crystallographic mismatch between the alloy surface and Cr_2O_3, and between Cr_2O_3 and the spinel phase could thus be considered.

p_{O_2} and temperature dependence of parabolic rate constants

Commercial high temperature alloys, such as Sanergy HT, contain numerous alloying components to achieve desirable mechanical properties. In addition to Fe and Cr, Sanergy HT consists of Mn, Si, Ti, Mo and Nb, all affecting the oxidation of the alloy. Due to the highly complex oxidation behaviour of multicomponent alloys, a complete and detailed analysis of all reaction products and diffusion processes in the alloy and the formed oxide phases is difficult. However, this section will attempt to elucidate general trends and dominating processes affecting the oxide scale growth in this particular alloy.

The p_{O_2} and temperature dependence of oxide growth rates on Sanergy HT were investigated. The parabolic rate constants measured for uncoated and cobalt coated samples were found to be essentially independent of p_{O_2}. The measurements were conducted under isothermal conditions at 900 °C, and parabolic rate kinetics were observed for all samples, indicating that the oxide growth is limited by diffusion of reacting species through the scale. Reaction rate constants at ambient oxygen pressures are generally observed to obey linear, Arrhenius-type behaviour. However, the temperature dependence of multicomponent alloys can contain large variations and irregularities due to the high number of components, oxide phases and processes occurring simultaneously.

Wagner's oxidation theory relates the parabolic growth rate constant, k_p, to the self diffusion coefficient of the reacting species participating in the oxide formation. If the defect concentrations enabling diffusion in the oxide are dependent of oxygen activity, it is thus expected that the parabolic growth rate constants will vary as a function of p_{O_2}. Both oxides formed on uncoated Sanergy HT, Cr_2O_3 and $(Cr, Mn)_3O_4$, are expected to exhibit p_{O_2} dependent defect concentrations. The majority of the oxide scale grown on Sanergy HT consists of Cr_2O_3. It will be assumed, as a simplification, that the growth of chromia has the largest impact on the measured parabolic growth rate constants. The oxide growth of chromia is observed to be governed by predominately outward diffusion of chromium.

The amount of oxygen needed in the surrounding atmosphere to sustain oxide formation is small, and is thus not a limiting factor in the scale growth. What limits the oxide growth, is the transport of chromium ions through the scale. Any p_{O_2} dependence found for parabolic growth rate constants is thus expected to reflect changes in the ability to transport chromium, that is changes in defect concentrations enabling Cr diffusion. In addition, for oxides grown on metal surfaces, a gradient in oxygen activity will be present across the scale, from a maximum at the gas-oxide interface to a minimum near the oxide-alloy interface. This is due to the migration of metal ions and

oxygen ions in opposite directions through the scale. It is thus expected that p_{O_2} dependent defect concentrations vary throughout the oxide layer.

As previously mentioned, the oxide scale on Sanergy HT consists mainly of a Cr_2O_3 layer near the oxide-alloy interface and a spinel layer near the gas-oxide interface. Assuming that the growth of chromia dominates the measured parabolic rate constants, the lack of p_{O_2} dependence could result directly from the defect situation in Cr_2O_3. Cation point defects, v'''_{Cr} and $Cr_i^{\bullet\bullet\bullet}$ are assumed to be the majority defects in chromia, while $v_O^{\bullet\bullet}$ and O_i'' are present as minority defects. The total electroneutrality of Cr_2O_3 can be seen in equation 2.10 on page 11. In a constructed Brouwer diagram for pure Cr_2O_3, see figure 2.4, a region independent of p_{O_2} is expected when chromium interstitials ($Cr_i^{\bullet\bullet\bullet}$) and chromium vacancies (v'''_{Cr}) are the dominating species. This would require chromium ions to diffuse outwards through an interstitial mechanism or through lattice vacancies. Diffusion through interstitial positions is most energetically favourable for chemical species of small ionic radii, as larger ions could require expansion of the lattice. However, structural gaps such as grain boundaries, interfaces and stress induced cracks can provide rapid diffusion paths for ions in oxides.

The effect of Fe, Mn, Si, Ti, Mo and Nb

Defect concentrations in Cr_2O_3 scales grown on Fe-Cr alloys can be affected by foreign elements entering as dopants, significantly altering the defect structure of the oxide. Elements such as Fe, Mn, Si, Ti, Mo, and Nb are all present in Sanergy HT.

Increased concentrations of Ti, Si, Mo and Nb have been observed in the spinel-chromia and chromia-alloy interfaces, while Mn is also a reacting species in formation of the $(Cr, Mn)_3O_4$ spinel phase. The presence of these alloying elements in oxide-oxide and oxide-alloy interfaces of Sanergy HT has been reported by Canovic et al.[45] Iron oxides are also likely to be formed prior to the formation of a continuous Cr_2O_3 film on the alloy surface. To elucidate the effect foreign cations have on defect concentrations in chromia, and subsequently the p_{O_2} dependence of parabolic growth rate constants, constant dopant concentrations are assumed as a first approximation.

The Cr_2O_3 layer has been observed to grow predominately by outward diffusing chromium. If cation point defects are assumed to dominate the defect structure of chromia, the nonstoichiometry of Cr_2O_3 could be described as either $Cr_{2-y}O_3$ or $Cr_{2+y}O_3$. At high p_{O_2}, chromia is now assumed to be metal deficient and the dominating defects are chromium vacancies (v'''_{Cr}) and electron holes ($h^{\bullet}$). At low p_{O_2}, Cr_2O_3 is assumed to

exhibit metal excess with dominating defects being interstitial chromium ($Cr_i^{\bullet\bullet\bullet}$) and electrons ($e'$).

If Mn is introduced as a lower valent dopant in chromia near the spinel-chromia interface, this would reduce the concentration of chromium vacancies and increase the concentration of electron holes. Near the oxide-alloy interface, Mn'_{Cr} would increase the concentration of interstitial chromium and reduce the concentration of electrons. As the concentration of Mn would be highest in the outer part of the oxide scale, the effect of Mn as a dopant would be most significant in this region. Negative Mn'_{Cr} defects would be compensated by positive electron holes, and the concentration of v'''_{Cr} is reduced. Reduced concentration of chromium vacancies could reduce outward chromium transport in the outer part of the scale, which could lead to reduced growth rates.

Si, Ti, Nb and Mo will enter as higher valent dopants in Cr_2O_3. Positive $Ti^{\bullet}_{Cr}$, $Si^{\bullet}_{Cr}$, $Mo^{\bullet}_{Cr}$ and $Nb^{\bullet\bullet}_{Cr}$ defects will be compensated by negative defects, while the concentration of positive defects present will be reduced. In the outer part of the scale, Si, Ti and Nb substituted on chromium lattice sites will reduce the concentration of electron holes and increase the concentration of v'''_{Cr}. In the inner part of the scale, the concentration of chromium interstitials will decrease and the concentration of electrons increase. Increased concentrations of chromium vacancies could increase oxide growth rates, and the effect would be most significant in the outer part of the oxide scale due to the higher p_{O_2}. Ti, Si and Nb would, as higher valent dopants, counteract the effect of lower valent Mn. Common for these dopant reactions, is that charge compensation by chromium vacancies and chromium interstitials would give no contribution to p_{O_2} dependency. Equation 6.1 show Si as an example of a higher valent dopant in Cr_2O_3.

$$3SiO_2(s) = 3Si^{\bullet}_{Cr} + v'''_{Cr} + 6O^x_O \tag{6.1}$$

It is expected that the alloying elements are present in the system as precipitated oxides. Precipitations are observed at the oxide-alloy interface both in oxidizing and reducing conditions at temperatures between 900 °C and 1000 °C. Precipitated second phases indicate that the total amount of solute has exceeded the solubility limit. When a second phase of solute has precipitated, the concentration of solute is not constant, but will vary by exchange between the bulk and the second phase. The solubility of dopants can be dependent of both p_{O_2} and temperature. It is thus possible that the solubility will vary across the oxide scale due to the gradient in p_{O_2}. The solubility will in this case vary with p_{O_2} until the oxide phase is completely dissolved. The behaviour will then resemble that of a constant dopant concentration.

The lack of p_{O_2} dependence of parabolic rate constants found for Sanergy HT is assumed to be caused by rapid outward chromium diffusion enabled by aliovalent defects present in the oxide. The effect of cation impurities in chromia is also suggested by Kofstad.[7] Still, the parabolic rate constants determined for the Fe-Cr alloy in this work are approximately two orders of magnitude smaller than the rate constants reported for oxidation of pure Cr.[29]

The parabolic rate constants determined for cobalt coated samples showed approximately linear temperature dependence, and the activation energy was calculated to 323 kJ/mol. The activation energy corresponds well with that reported for the same alloy,[61] but is higher than values typically reported for similar chromia forming alloys ($\sim$ 250 kJ/mol).[62,63]The activation energy for chromium tracer diffusion in chromia has been reported in the range of 245-280 kJ/mol.[7,36] Due to the large uncertainties in measuring parabolic growth rate constants, the activation energy determined in this work is assumed to correspond to that of Cr diffusion in chromia. The slightly higher activation energy could be related to the growth of (Co, Mn)$_3$O$_4$.

The non-linear Arrhenius behaviour observed for uncoated samples oxidized under reducing conditions in the same temperature range could indicate two temperature regions where different processes are dominating the oxide growth. The first region is from 1000 °C to 925 °C, and the second from approximately 900 °C to 800 °C. To extract activation energies from each temperature region is possible, but could be misleading as the changeover between dominating processes occurs gradually. As the non-linear temperature dependence is more significant for uncoated samples, one could suspect an effect from the evaporation of chromium containing species. However, chromium volatilization is strongly dependent of p_{O_2} and no chromium evaporation is expected under reducing conditions.[20]

The rate constants in the Arrhenius plot in figure 5.16 were all calculated from 45 hours of oxidation. At this time, the oxide scale thicknesses will vary significantly for samples oxidized at different temperatures and the measured rate constants can thus represent different stages in the oxidation sequence. To explore the effect of scale thickness on the general behaviour, the rate constants were corrected to the same expected scale thickness for every sample, see figure 5.18. It can be seen that the $k_{p,w}$ values at temperatures from 1000 °C to 950 °C show a more linear trend when corrected to the same oxide scale thickness. The effect of correcting to equal oxide scale thickness is smaller for samples at the lower temperatures, between 925 °C and 850 °C. As the oxide scales grow more rapidly at higher temperatures, it is expected that the effect of correcting to similar scale thickness increases.

It can be concluded that correcting the calculated rate constants to the same scale thickness do not yield a linear temperature dependence across the full temperature range. This finding supports the presence of two temperature regions of different growth processes.

The two regions can be a result of one region where the growth of Cr_2O_3 is favoured, and one where the growth of (Cr, Mn)$_3O_4$ is governing the rate kinetics. In the high temperature region, it is probable that the oxide scale growth has several contributions and that the temperature dependence thus reflect a combination or coupling of mechanisms. Evidence of oxide scale growth by counter-diffusion of both cation and anions, such as deformation of the oxide-alloy interface, have been found at 1000 °C, but appear to be most significant under highly oxidizing conditions. The formation of oxide ridges on top of grain-boundaries is also observed, indicating contributions from ion transport in grain boundaries. It is observed that the ratio between Cr_2O_3 and (Cr, Mn)$_3O_4$ is significantly larger with increasing temperature, indicating that chromia is the fastest growing oxide at higher temperatures. It is thus likely that the rate constants observed in the high temperature region is governed by the growth of Cr_2O_3, which seem probable considering that the determined activation energy is in the range of that reported for Cr diffusion in chromia. In the low temperature region, the rate constants can be more influenced by the growth of (Cr, Mn)$_3O_4$ and not dominated by chromia growth. If the spinel layers of uncoated and cobalt coated samples at lower temperatures are compared, the (Co, Mn)$_3O_4$ layers of cobalt coated samples are significantly thicker. The Cr_2O_3 parts of the oxide scales are however comparable. Assuming that the rate constants measured in the low temperature region are dominated by the growth rate of (Cr, Mn)$_3O_4$, the difference in temperature dependence of the high and low temperature regions could result from different temperature dependencies of chromium and manganese diffusion rates.

The temperature dependence is most likely also affected by the presence of large concentrations of aliovalent dopants, as discussed previously. So far, only individual point defects have been discussed. However, for large defect concentrations defects may interact to form associated defects. In chromia scales growing on multicomponent alloys, the concentration of dopants is most likely high enough for associated defects to become energetically favourable. Higher valent dopants such as $Ti_{Cr}^{\bullet}$, $Si_{Cr}^{\bullet}$, $Nb_{Cr}^{\bullet\bullet}$ and $Mo_{Cr}^{\bullet\bullet\bullet}$ may associate with negative defects, for instance chromium vacancies, $v_{Cr}^{\prime\prime\prime}$. Lower valent Mn may associate with positively charged native defects such as chromium interstitials. Equations 6.22 show an example of formed associated defect clusters between Si and chromium vacancies.

$$2v_{Cr}^{\prime\prime\prime} + Si_{Cr}^{\bullet} = (2v_{Cr}Si_{Cr})^{5\prime} \tag{6.2}$$

The high concentration of positively charged dopants could lead to significant amounts of associated defects between these dopants and chromium vacancies. This would severely reduce the mobility of the chromium vacancies trapped in these defect complexes and possibly effect oxide growth rates, especially at lower temperatures.

The formation of complex defects may increase the activation energy for transport along grain boundaries. If negative chromium vacancies are associated with effectively positive reactive elements substituting a Cr site, this can reduce the outward chromium transport. In the same way may positive oxygen vacancies associate with a lower valent dopant and reduce the inward diffusion of oxygen.

6.2.3 Protonic defects in oxides at high temperatures

The non-linear temperature dependence of uncoated samples is most significant under reducing conditions. Hydrogen may dissolve as protonic defects in chromia, significantly affecting the defect structure and subsequently oxide growth rates. This is also suggested by Norby.[64]

Protons, $OH_O^{\bullet}$, are positively charged and is compensated by negative defects in the oxide. In Cr_2O_3, these negative defects could be chromium vacancies, v_{Cr}'''. Higher concentrations of chromium vacancies can increase the migration rate of outward diffusing chromium, favouring oxide growth by outward diffusing cations at or near the gas-oxide interface. This can contribute to more uniform and stress free scale growth, as is observed under reducing conditions in this work. Holt and Kofstad[33] reported the solubility of hydrogen in chromia to increase with decreasing temperature at constant p_{H_2}. The effect of hydrogen doping in chromia is thus assumed to be largest at lower temperatures.

As the charge of protons is smaller than the charge of oxygen ions, the ionic radius will also be smaller. The reduction in size from O^{2-} to hydroxide ions could increase the mobility of oxygen in the oxide scale. However, this effect is assumed to be small and will not affect measured oxide growth rates significantly, as scales under reducing conditions appear to grow predominately by outward Cr diffusion.

6.2.4 Sanergy HT as interconnect material in fuel cell systems

To evaluate the Fe-Cr alloy Sanergy HT as a potential interconnect material, a high number of material properties must be investigated. Section 3.3.1 provides the list of standard requirements a fuel cell interconnect must fulfill.

However, this study is limited to the oxidation behaviour of the alloy and the evaluation can thus be made from oxidation kinetics and scale properties only.

Ferritic alloys as metallic interconnects are favoured due to slow oxidation kinetics, high electrical conductivity and low price. Due to the strict requirements in mechanical properties, only minor changes in elemental composition can be made to improve the oxidation behaviour of the alloy further. Consequently,surface coatings appear as the most convenient method to achieve desired oxidation kinetics and scale properties. The evaporation of chromium containing species from uncoated Sanergy HT make coatings a necessity if this alloy is to be used in fuel cell systems. Parts of the experimental work in this study were conducted on cobalt coated samples, and a brief evaluation of the effect will be given in section 6.2.5. The precipitation of Si and Ti oxide phases, and oxides of other alloying elements, in the alloy-oxide and spinel-chromia interfaces may significantly affect the electrical conductivity through the scale. Further work should therefore be conducted to investigate the electrical properties of oxide scales grown on Sanergy HT.

6.2.5 Chromium evaporation and the effect of cobalt coating

If iron-chromium alloys are to be used as interconnects in fuel cell systems, the evaporation of chromium containing species, such as $CrO_2(OH)_2$,[65,66] must be prevented. Evaporated chromium will poison the electrodes, especially on the cathode side, leading to cell degradation. The addition of Mn in the alloy results in an outer oxide layer of (Cr, Mn)$_3$O$_4$. Although this spinel oxide reduces the volatilization of chromium by about 50 %,[23,67] further improvements are needed to reduce the evaporation of Cr sufficiently.

One cost effective method investigated is precoating the alloy surface with metallic cobalt. Submicrometer cobalt coatings are reported to reduce chromium evaporation by one order of magnitude[68] due to the formation of an outer oxide layer of (Co,Mn)$_3$O$_4$. The samples used in this work had a surface coating of 600 nm Co, applied by a physical vapour deposition process developed by the alloy manufacturers Sandvik Materials Technology. To ensure high efficiency of the fuel cell, the electrical resistance through the stack must also be kept at a minimum. The corrosion protective oxide scale growing on Fe-Cr alloys will cause the electrical resistance through the interconnect to increase. It is thus desired to form oxide scales of high electrical conductivity. The evaporation of chromium is not investigated in this work, but as the chromium content in the outer part of the oxide scale of coated samples is significantly reduced, the cobalt coating appear to be successful. At the lower temperatures, the (Co, Mn)$_3$O$_4$ phase appears to

cover the surface completely. However, as the temperature is increased above 925 °C, large clusters of chromium rich particles are observed under reducing conditions. Chromium evaporation from these precipitations is assumed to be significant, indicating that the cobalt coating only reduce Cr migration sufficiently below this temperature.

By HT-ESEM it is also observed that the oxide scales formed on cobalt coated samples have higher electrical conductivities than the scales on uncoated samples. This is due to increased electrical conductivity of (Co, Mn)$_3$O$_4$ spinels phase compared to (Cr, Mn)$_3$O$_4$ spinels. Electrical conductivities of selected Co-Mn spinels at 800 °C are given in table 3.1 on page 26.

6.3 Evaluation of in-situ HT-ESEM as an experimental method in high temperature oxidation

The formation and development of surface features on alloys during high temperature oxidation can give insight to the competing processes present during oxide scale growth. Ex-situ investigation methods are by far the most common, but to get a more profound understanding of processes in multicomponent alloys oxidized in complex environments, methodological errors and weaknesses must be eliminated. Samples observed with ex-situ methods undergo cooling, which may severely alter the microstructure of the oxide scale and also the oxidation products. In-situ methods have the potential of eliminating known sources of error by enabling continuous observation as features occur and develop. High Temperature Environmental Scanning Electron Microscopy is a potentially flexible experimental method, enabling the use of various gas mixtures in a wide temperature range. Samples can be observed during heating, at isothermal temperature and during cooling, which provides information about every step of the oxidation process. To learn the full potential of HT-ESEM and increase its credibility as an experimental method in high temperature oxidation, more work has to be done. The comparability of results from HT-ESEM and ex-situ methods must be determined. There are also experimental challenges to overcome if HT-ESEM is to rise in the scientific community as an equally accepted method to traditional ex-situ investigation methods.

Similar to ex-situ methods, samples investigated by HT-ESEM is oxidized in a controlled atmosphere, where temperature, gas composition and pressure can be adjusted and monitored throughout the experiment. However, the experiment takes place inside an electron microscope variations are limited. For instance is atmospheric pressure not possible, as the electron column in

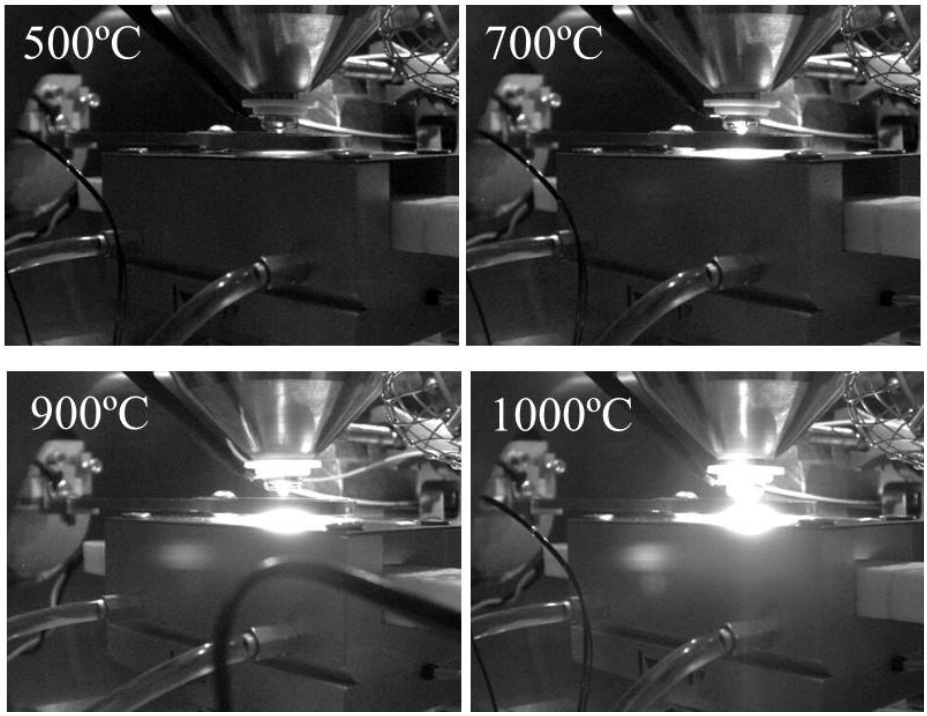

Figure 6.3: Image of HT-ESEM setup showing the development of thermal electrons as a function of temperature from 500 °C to 1000 °C.

the microscope must be protected. The samples are thus exposed to low vacuum conditions, which may affect the oxidation behaviour.

Although various gas compositions can be used, the experimental difficulty limits the options which successfully can be used. The electronic conductivity of the growing oxide scale is observed to be a limiting factor for image quality. Higher acceleration voltages can provide improved focus at higher magnifications, but sufficient conductivity is required to prevent charge accumulation on the sample surface. Charge accumulation is detrimental to the image quality. At high temperatures, signals from thermally excited electrons must be reduced. The most crucial factor in obtaining high image quality is good electrical connection between sample and sample holder. Both the sample bias and the heat shield bias used in this work are necessary to guard the detectors from excess electrons at higher temperatures, see figure 6.3. However, the effect is varying and inconsistent.

Chapter 7

Conclusions

The objective of this work was to investigate the high temperature oxidation behaviour of the multicomponent Fe-Cr alloy Sanergy HT under reducing and oxidizing conditions. More insight in elucidating the dominating growth mechanisms of Cr_2O_3 and $(Cr, Mn)_3O_4$ has been achieved, although the complexity of high temperature oxidation of multicomponent alloys impedes a detailed analysis of the system.

The oxidation of Sanergy HT generally follows parabolic growth kinetics, indicating diffusion controlled oxide scale growth. The formed scale is a duplex oxide layer of Cr_2O_3 near the alloy-oxide interface with a $(Cr, Mn)_3O_4$ spinel phase on top. Based on SIMS depth profiles, the oxide scale is assumed to grow predominately from the gas-spinel and spinel-chromia interfaces by outward diffusion of Cr and Mn. The ratio between Cr_2O_3 and $(Cr, Mn)_3O_4$ increases as a function of temperature, indicating significantly more rapid growth of chromia at higher temperatures compared to that of $(Cr, Mn)_3O_4$.

The measured parabolic growth rate constants are independent of p_{O_2} and show non-linear dependence of temperature. This supports that the defect structure and transport properties of chromia are significantly influenced by aliovalent dopants. Elements present in small amounts in the alloy, such as Mn, Ti, Si, Nb and Mo, significantly alter the oxidation behaviour compared to that of pure metals and binary alloys.

It can be concluded that an applied coating of cobalt significantly reduces the concentration of chromium in the outer part of the oxide scale. This is an important step in reducing chromium evaporation from the alloy, which must be avoided during fuel cell operation.

As a method, in-situ HT-ESEM has great potential in investigating oxide growth processes at high temperatures. However, the experimental difficul-

ties and instability of the high temperature setup limit the possibilities. To reach the level of stability and certainty needed, HT-ESEM as a method must be developed further.

7.1 Further work

The oxidation experiments conducted in this work were relatively short, and prolonged experiments should be made to improve the understanding of dominating growth mechanisms after longer oxidation times. This will reduce the uncertainty of the thermogravimetric measurements, and as the oxide layers are thicker, sample preparation and analysis of cross-sections will be less difficult.

To achieve more knowledge regarding the diffusivity of Mn, SIMS analysis by oxygen sputtering should be attempted. This could increase the secondary ion intensities from Mn, leading to improved results. SIMS depth profiles of ion distributions in scales under reducing conditions would also be interesting, as growth mechanisms may vary. The limits and possibilities of HT-ESEM as an experimental method should be investigated further. In-situ observations during high temperature oxidation can eliminate uncertainties often linked to ex-situ analysis, such as cooling, and also provide valuable information of competing processes and development of surface features.

To better understand the effect of temperature, p_{O_2} and aliovalent dopants on growth rates of Cr_2O_3 and $(Cr, Mn)_3O_4$, more investigations should be conducted in clarifying the defect concentrations in these oxides. The effect of alloying elements on oxidation behaviour of multicomponent alloys is not yet fully understood. To reduce the degree of complexity, alloys of less components could be investigated. However, it is important to continue fundamental research on commercially available multicomponent alloys as these are the widely used alloys in high temperature technology.

Bibliography

[1] W. Z. Zhu and S. C. Deevi. Development of interconnect materials for solid oxide fuel cells. *Materials Science and Engineering*, 2003.

[2] K. Huang, P. Y. Hou, and J. B. Goodenough. Characterization of iron-based alloy interconnects for reduced temperature solid oxide fuel cells. *Solid State Ionics*, 29, 2000.

[3] World Energy Council. 2013 World Energy Issues Monitor, February 2013.

[4] S. P. S. Badwal and K. Foger. Solid oxide electrolyte fuel cell review. *Ceramics international*, 22, 1996.

[5] A. B. Stambouli and E. Traversa. Solid oxide fuel cells (SOFCs): a review of an environmentally clean and efficient source of energy. *Renewable and Sustainable Energy Reviews*, 6, 2002.

[6] R. M. Ormerod. Solid oxide fuel cells. *Chemical Society Reviews*, 32, 2003.

[7] P. Kofstad. *High Temperature Corrosion*. Elsevier Applied Science, 1988.

[8] H. J. T. Ellingham. Reducibility of oxides and sulphides in metallurgical processes. *Journal of the Society of Chemical Industry*, 63, 1944.

[9] P. A. Tempest and R. K. Wild. Thickness Measurements of Spinel and Chromia Layers in Stainless Steel Oxide Scales by X-Ray Diffractometry. *Oxidation of Metals*, 17, 1982.

[10] P. Kofstad and T. Norby. *Defects and Transport in Crystalline Solids*. Department of Chemistry, Faculty of Mathematics and Natural Sciences, University of Oslo, 2012.

[11] F. A. Kroger and H. J. Vink. *Relations between the concentrations of imperfections in crystalline solids*, volume 3, pages 273–301. Academic Press, New York, 1956.

[12] R .E. Löbnig, H. P. Schmidt, K. Hennesen, and H. J. Grabke. Diffusion of cations in chromia layers grown on iron-base alloys. *Oxidation of Metals*, 32, 1992.

[13] J. D. Verhoeven. *Fundamentals of Physical Metallurgy.* John Wiley and Sons, 1975.

[14] World Steel Association. "about steel", January 2013.

[15] J. P. Davis. *Heat Resistant Materials.* ASM International, 1997.

[16] K.P. Lillerud and P. Kofstad. On high temperature oxidation of chromium. *Journal of the Electrochemical Society*, 127, 1980.

[17] O. Yamamoto. Solid oxide fuel cells: fundamental aspects and prospects. *Electrochimica Acta*, 45, 2000.

[18] F. W. Jeffrey. Metallic interconnects for solid oxide fuel cells. *Materials Science and Engineering: A*, 397, 2005.

[19] N. Q. Minh. Ceramic fuel cells. *Journal of the American Ceramic Society*, 76, 1993.

[20] P. Kofstad and R. Bredesen. High temperature corrosion in SOFC environments. *Solid State Ionics*, 52, 1992.

[21] H. Yokokawa. *Overview of Intermediate-Temperature Solid Oxide Fuel Cells*, pages 17–43. Springer US, 2009.

[22] J. E. Hammer, S. J. Laney, R. W. Jackson, K. Coyne, F. S. Pettit, and G. H. Meier. The oxidation of ferritic stainless steels in simulated solid-oxide fuel-cell atmospheres. *Oxidation of Metals*, 67, 2007.

[23] Z. Yang, G. Xia, and J. W. Stevenson. Evaluation of NiCr-base alloys for SOFC interconnect applications. *Journal of Power Sources*, 160, 2006.

[24] ThyssenKrupp VDM. Crofer 22 h preliminary material data sheet no. 4050, June 2008.

[25] S. Fontana, R. Amendolab, S. Chevalier, P. Piccardo, G. Caboche, M. Viviani, R. Molins, and M. Sennour. Metallic interconnects for SOFC: Characterisation of corrosion resistance and conductivity evaluation at operating temperature of differently coated alloys. *Journal of Power Sources*, 171, 2007.

[26] P. Huczkowski, V. Shemet, J. Piron-Abellan, L. Singheiser, W. J. Quadakkers, and N. Christiansen. Oxidation limited life times of chromia forming ferritic steels. *Materials and Corrosion*, 55(11), 2004.

[27] F. H. Stott, G. C. Wood, and J. Stringer. The influence of alloying elements on the development and maintenance of protective scales. *Oxidation of Metals*, 44, 1995.

[28] J. Klöwer. Factors affecting the oxidation behaviour of thin Fe-Cr-Al foils part ii: The effect of alloying elements: Overdoping. *Materials and Corrosion*, 51, 2000.

[29] E. A. Polman, Fransen T., and Gellings P. J. The reactive element effect: ionic processes of grain-boundary segregation and diffusion in chromium oxide scales. *Journal of Physics: Condensed Matter*, 1, 1989.

[30] N. Shaigan, W. Qu, D. G. Ivey, and W. Chen. A review of recent progress in coatings, surface modifications and alloy developments for solid oxide fuel cell ferritic stainless steel interconnects. *Journal of Power Sources*, 195, 2010.

[31] M. Schuisky. PreCoated Sandvik Sanergy TM HT: A New Advanced Interconnector Material in SOFCs, 2007.

[32] E. W. A. Young, J. H. Gerretsen, and J. H. Wit. The oxygen partial pressure dependence of the defect structure of chromium(iii)oxide. *Journal of Electrochemical Society*, 134, 1987.

[33] A. Holt and P. Kofstad. Electrical conductivity and defect structure of Cr_2O_3, reduced temperatures. *Solid State Ionics*, 69, 1994.

[34] A. Holt and P. Kofstad. Electrical conductivity and defect structure of Cr_2O_3, high temperatures. *Solid State Ionics*, 69, 1994.

[35] P. Kofstad and K. P. Lillerud. Chromium transport through Cr_2O_3 scales. i. on lattice diffusion of chromium. *Oxidation of Metals*, 17, 1982.

[36] A. C. S. Sabioni, B. Lesage, A. M. Huntz, J. C. Pivin, and C. Monty. Self-diffusion in Cr_2O_3 i. chromium diffusion in single crystals. *Philosophical Magazine A-Physics of Condensed Matter Structure Defects and Mechanical Properties*, 66, 1992.

[37] D. Caplan and G. I. Sproule. Effect of oxide grain structure on the high-temperature oxidation of Cr. *Oxidation of Metals*, 9, 1975.

[38] A. Atkinson and R. I. Taylor. Diffusion of 51cr tracer in Cr_2O_3 and the growth of Cr_2O_3 films. *NATO ASI Series*, 129, 1985.

[39] S. C. Tsai, A. M. Huntz, and C. Dolin. Diffusion of 180 in massive Cr_2O_3 and in Cr_2O_3 scales at 900 °C and its relation to the oxidation kinetics of chromia forming alloys. *Oxidation of Metals*, 43, 1995.

[40] B. Schmid, N. Aas, Grong Ø., and R. Ødegård. High-temperature oxidation of nickel and chromium studied with an in-situ environmental scanning electron microscope. *Scanning*, 23, 2001.

[41] B. Schmid, N. Aas, Grong Ø., and R. Ødegård. High-temperature oxidation of iron and the decay of Wüstite studied with in situ ESEM. *Oxidation of Metals*, 57, 2002.

[42] T. Jonsson, B. Pujilaksono, S. Hallström, J. Ågren, J.-E. Svensson, L.-G. Johansson, and M. Halvarsson. An ESEM in situ investigation of the influence of H_2O on iron oxidation at 500°C. *Corrosion Science*, 51, 2009.

[43] A. Reichmann, P. Poelt, Ch. Brandl, B. Chernev, and P. Wilhelm. High-temperature corrosion of steel in an ESEM with subsequent scale characterization by Raman microscopy. *Oxidation of Metals*, 70, 2008.

[44] FEI Company. The Quanta FEG 200, 400, 600 user's operation manual 1st edition, 2003.

[45] S. Canovic, J. Froitzheim, R. Sachitanand, M. Nikumaa, M. Halvarsson, L.-G. Johansson, and J.-E. Svensson. Oxidation of Co- and Ce-nanocoated FeCr steels: A microstructural investigation. *Surface & Coatings Technology*, 215, 2013.

[46] H.S. Hsu and G.J. Yurek. Kinetics and mechanisms of the oxidation of cobalt at 600-800°C. *Oxidation of Metals*, 17, 1982.

[47] H. Hindam and D. P. Whittle. Microstructure, adhesion and growth kinetics of protective scales on metals and alloys. *Oxidation of Metals*, 18, 1982.

[48] G. M. Raynaud and R. A. Rapp. In situ observations of whiskers, pyramids and pits during the high temperature oxidation of metals. *Oxidation of Metals*, 21, 1984.

[49] E. A. Polman, T. Fransen, and P. J. Gellings. Oxidation kinetics of chromium and morphological phenomena. *Oxidation of Metals*, 32, 1989.

[50] K. P. Lillerud and Kofstad P. Chromium transport through Cr_2O_3 scales. ii. changes in scale morphology during high vacuum treatment of oxidized chromium specimens. *Oxidation of Metals*, 17, 1982.

[51] R. L. Tallman and E. A. Gulbransen. Crystal morphology and mechanisms of growth of alpha-Fe_2O_3 whiskers on iron. *Journal of The Electrochemical Society*, 114, 1967.

[52] R. Takagi. Growth of oxide whiskers on metals at high temperatures. *Journal of the Physical Society of Japan*, 12, 1957.

[53] R.J. Asaro and W.A. Tiller. Interface morphology development during stress corrosion cracking: Part i. via surface diffusion. *Metallurgical transactions*, 3, 1972.

[54] P. Kofstad. On the formation of porosity and microchannels in growing scales. *Oxidation of Metals*, 24, 1985.

[55] T. Horita, Y. Xiong, K. Yamaji, H. Kishimoto, N. Sakai, M. E. Brito, and H. Yokokawa. Imaging of mass transports around the oxide scale/Fe-Cr alloy interfaces. *Solid State Ionics*, 174, 2004.

[56] David Young. *High Temperature Oxidation and Corrosion of Metals*. Elsevier Corrosion Series, 2008.

[57] A. W. B. Skilbred and R. Haugsrud. Sandvik Sanergy HT - a potential interconnect material for LaNbO4-based proton ceramic fuel cells. *Journal of Power Sources*, 206, 2012.

[58] M. G. C. Cox, B. Mcenaney, and V. D. Scott. A chemical diffusion model for partitioning of transition elements in oxide scales on alloys. *Philosophical Magazine*, 26, 1972.

[59] R. K. Wild. High temperature oxidation of austenitic stainless steel in low oxygen pressure. *Corrosion Science*, 17, 1977.

[60] T. Horita, H. Kishimoto, K. Yamaji, Y. Xiong, N. Sakai, M. Brito, and H. Yokokawa. Effect of grain boundaries on the formation of oxide scale in FeCr alloy for SOFCs. *Solid State Ionics*, 179, 2008.

[61] A. W. B Skilbred. *Metallic Interconnects for Proton Ceramic Fuel Cells, Oxidation behaviour and transport properties under simulated fuel cell conditions*. PhD thesis, Department of Chemistry, Faculty of Mathematics and Natural Sciences, University of Oslo, 2012.

[62] T. Brylewski, T. Maruyama, M. Nanko, and K. Przybylski. TG measurements of the oxidation kinetics of Fe-Cr alloy with regard to it application as a separator in SOFC. *Journal of Thermal Analysis and Calorimetry*, 55, 1999.

[63] A. C. S. Sabioni, A.-M. Huntz, E. C. Luz, M. Mantel, and C. Haut. Comparative study of high temperature oxidation behaviour in AISI 304 and AISI 439 stainless steels. *Materials Research*, 6, 2003.

[64] T. Norby. Protonic defects in oxides and their possible role in high temperature oxidation. *Journal de Physique IV*, 3, 1993.

[65] H. Asteman, J.-E. Svensson, and L.-G. Johansson. Effect of water-vapor-induced Cr vaporization on the oxidation of austenitic stainless

steels at 700 and 900 °C. *Journal of The Electrochemical Society*, 151, 2004.

[66] H. Asteman, J.-E. Svensson, L.-G. Johansson, and M. Norell. Indication of chromium oxide hydroxide evaporation during oxidation of 304L at 873 K in the presence of 10% water vapor. *Oxidation of Metals*, 52, 1999.

[67] M. Stanislowski, J. Froitzheim, L. Niewolak, W.J. Quadakkers, K. Hilpert, T. Markus, and L. Singheiser. Reduction of chromium vaporization from SOFC interconnectors by highly effective coatings. *Journal of Power Sources*, 164, 2007.

[68] J. Froitzheim, H. Ravash, E. Larsson, L. G. Johansson, and J. E. Svensson. Investigation of chromium volatilization from FeCr interconnects by a Denuder technique. *Journal of The Electrochemical Society*, 157, 2010.

Appendix

A summary of parabolic rate constants measured for uncoated and cobalt coated samples oxidized under reducing and oxidizing conditions at temperatures from 800° to 1000°C is given in tables 7.1 and 7.2.

Table 7.1: Summary of parabolic rate constants measured for uncoated samples oxidized under reducing and oxidizing conditions at temperatures from 800° to 1000°C.

Atmosphere	**Temperature, °C**	$\mathbf{k_{p,w}}$**, g^2/cm^{4}s**
Uncoated		
Wet air	850	$6.3{\cdot}10^{-14}$
Wet air	850	$1.6{\cdot}10^{-14}$
Wet air	900	$5.3{\cdot}10^{-14}$
Wet air	925	$2.9{\cdot}10^{-12}$
Wet air	950	$8.9{\cdot}10^{-12}$
Wet air	1000	$2.6{\cdot}10^{-11}$
Wet 5% H_2 in Ar	800	$2.7{\cdot}10^{-13}$
Wet 5% H_2 in Ar	850	$2.8{\cdot}10^{-13}$
Wet 5% H_2 in Ar	875	$3.1{\cdot}10^{-13}$
Wet 5% H_2 in Ar	900	$3.9{\cdot}10^{-13}$
Wet 5% H_2 in Ar	925	$3.1{\cdot}10^{-12}$
Wet 5% H_2 in Ar	950	$9.2{\cdot}10^{-12}$
Wet 5% H_2 in Ar	1000	$1.5{\cdot}10^{-11}$
O_2+Ar (p_{O_2}: $1.0{\cdot}10^{-5}$ atm)	900	$5.0{\cdot}10^{-13}$
O_2+Ar (p_{O_2}: $9.6{\cdot}10^{-3}$ atm)	900	$9.9{\cdot}10^{-13}$
O_2+Ar (p_{O_2}: $2.3{\cdot}10^{-2}$ atm)	900	$5.8{\cdot}10^{-13}$
O_2+Ar (p_{O_2}: $2.4\ {\cdot}10^{-1}$ atm)	900	$5.0{\cdot}10^{-13}$
O_2+Ar (p_{O_2}: $3.2\ {\cdot}10^{-1}$ atm)	900	$3.6{\cdot}10^{-13}$
O_2+Ar (p_{O_2}: 1.0 atm)	900	$4.0{\cdot}10^{-13}$

Table 7.2: Summary of parabolic rate constants measured for 600 nm Co coated samples oxidized under reducing and oxidizing conditions at temperatures from 850° to 1000°C.

Atmosphere	**Temperature, °C**	$\mathbf{k_{p,w}}$**, g^2/cm^{4}s**
600 nm Co		
Wet air	850	$1.9{\cdot}10^{-13}$
Wet air	900	$1.3{\cdot}10^{-12}$
Wet air	1000	$1.0{\cdot}10^{-11}$
O_2	900	$1.4{\cdot}10^{-12}$
O_2	900	$1.0{\cdot}10^{-12}$
O_2	900	$1.8{\cdot}10^{-12}$
O_2+Ar (p_{O_2}: $1.6{\cdot}10^{-1}$ atm)	900	$1.3{\cdot}10^{-12}$
O_2+Ar (p_{O_2}: $5.8{\cdot}10^{-2}$ atm)	900	$1.7{\cdot}10^{-12}$
Ar (p_{O_2}: $1.0{\cdot}10^{-5}$ atm)	900	$1.8{\cdot}10^{-12}$
O_2+Ar (p_{O_2}: $6.1{\cdot}10^{-2}$ atm)	900	$1.5{\cdot}10^{-12}$
O_2+Ar (p_{O_2}: $2.3{\cdot}10^{-2}$ atm)	900	$2.6{\cdot}10^{-12}$
O_2+Ar (p_{O_2}: $9.6{\cdot}10^{-3}$ atm)	900	$1.8{\cdot}10^{-12}$
Wet 5% H_2 in Ar	800	$2.7{\cdot}10^{-13}$
Wet 5% H_2 in Ar	850	$2.8{\cdot}10^{-13}$
Wet 5% H_2 in Ar	850	$5.6{\cdot}10^{-13}$
Wet 5% H_2 in Ar	875	$3.1{\cdot}10^{-13}$
Wet 5% H_2 in Ar	900	$3.9{\cdot}10^{-13}$
Wet 5% H_2 in Ar	925	$3.1{\cdot}10^{-12}$
Wet 5% H_2 in Ar	925	$4.4{\cdot}10^{-12}$
Wet 5% H_2 in Ar	925	$5.2{\cdot}10^{-12}$
Wet 5% H_2 in Ar	950	$7.9{\cdot}10^{-12}$
Wet 5% H_2 in Ar	950	$9.2{\cdot}10^{-12}$
Wet 5% H_2 in Ar	975	$2.2{\cdot}10^{-11}$
Wet 5% H_2 in Ar	900	$1.7{\cdot}10^{-12}$
Wet 5% H_2 in Ar	1000	$1.5{\cdot}10^{-11}$
Wet 5% H_2 in Ar	1000	$2.6{\cdot}10^{-11}$